Characterization of manufactured MEMS Vaporizing Liquid Micro-resistojet

MSc Thesis in Aerospace Engineering

Saru Shrestha

TUDelft

Characterization of manufactured MEMS Vaporizing Liquid Micro-resistojet

MSc Thesis in Aerospace Engineering

by

Saru Shrestha

to obtain the degree of Master of Science
at the Delft University of Technology,
to be defended publicly on Thursday December 19, 2024 at 14:45.

Student number:	4570847
Supervisor:	Dr. Angelo Cervone
Faculty:	Faculty of Aerospace Engineering, Delft

Cover: The frontpage image consists of a background (courtesy of ISS Expedition 27 crew) and Delfi-n3Xt (courtesy of Delft University of Technology)

TUDelft

Preface

I would like to thank my supervisor, Dr. Angelo Cervone, for the opportunity to work on this research topic with his undoubted support, academic freedom to explore the research, and valuable feedback.
I want to appreciate my parents, who never had the same opportunities in life to achieve such educational milestones but provided me with the best starting point in life and inspired me to embark on challenges as big as space. Thank you!

<div align="right">

Saru Shrestha
Delft, December 2024

</div>

Summary

Micropropulsion systems like vaporizing liquid micro-resistojet (VLM) are essential in small satellites to realize applications like maneuverability and attitude control. Such VLMs are etched onto silicon wafers with fabricating technologies of micro electro mechanical systems called MEMS. As such, a new generation of MEMS VLM is manufactured at TU Delft that needs to be characterized for its performance. In this study, the objective is to evaluate the performance of next-generation MEMS VLMs by creating a numerical simulation model for the heater microchannel and micronozzle of the VLM and validating the model using existing experimental data.

A multiphase computational fluid dynamics (CFD) Volume of Fluid (VOF) method was used to visualize the flow regimes and characterize the heat transfer performance of the VLM microchannel. Similarly, a micronozzle CFD model with partial slip conditions at the wall was used to analyze the microthruster's thrust and specific impulse performance. The VLM microchannel model used a 2D rectangular mesh, while the micronozzle model featured a 3D linear convergent-divergent geometry. Both the numerical models were validated against the experimental data to ensure accuracy.

The VLM microchannel simulation results demonstrated the flow patterns observed during the flow boiling process in the microchannel. Bubble nucleation, growth, and confinement to an elongated bubble were revealed for the VLM microchannel flow. Similarly, the heat transfer characteristics including time-averaged wall temperature along the microchannel and heat transfer coefficient of the microchannel heater surface were presented. Although the VLM microchannel results were compared against the experimental data of Yin and Jia [116], the accuracy of the model could not be quantified. Despite this, the heat transfer performance trend for the case (sim 82) using the relaxation parameter value of $\lambda_e = \lambda_c$ = 1 s^{-1} in the evaporation condensation model, with a peak performance of 106.57 kW/m^2 at medium thermodynamic quality, x_e of 0.25 aligned with Yin's microchannel experiment. Sim 82 is thus considered the most representative of the real VLM microchannel flow boiling. The average heat transfer rate per single microchannel is calculated as 0.607 W and approximately 3.036 W for the five microchannels considered in this study, excluding the heater's inefficiency and surrounding losses. Numerical instability during the annular flow transition phase and dry-out phase was identified, demanding improved modeling.

Likewise, the VLM micronozzle CFD model results were presented assessing the thrust, mass flow rate, and specific impulse values compared to Cen and Xu's experimental data on performance using water as the propellant. The comparison showed differences of 8.7% in mass flow rate, 5.5% in thrust, and 1.2% in specific impulse, validating the model within a 10% margin of inaccuracy. Additionally, the performances of the new generation micronozzle compared to the third generation micronozzle from [36] using cold nitrogen gas at similar throat Reynolds were presented. The VLM micronozzle demonstrated the improved performance of the new generation VLM with a reduced subsonic layer (Mach<1) in the divergent section close to walls. It is attributed to higher divergence angles. However, thrust efficiency showed minor improvement due to geometric losses from non-axial velocities as a result of the high divergence angles. Thus, a balance between viscous losses and geometric losses needs to be taken into account to optimize the VLM performance. Similarly, a lower convergence angle is suggested, predicting lower flow reversal and pressure losses near the entrance, for the efficient operation of real VLM.

Lastly, the study assessed individual CFD simulations of the VLM microchannel and micronozzle, but it could not couple the two numerical models as was intended at the beginning of the research. Coupling could not be achieved due to uncertainties in the evaporation-condensation model and a lack of empirical data to estimate the relaxation parameters. It was also realized toward the end of the research that the idea to couple the two numerical models based on mass flow rate was impractical

given the sensitivity of multiphase microchannel flow simulation to boundary conditions, longer simulation times exceeding weeks even with the high-performance computing power of a supercomputer, complexity surrounding microchannel flow boiling CFD models and the time available for this thesis research. Despite the situation, valuable results have been presented in this work, and recommendations are provided for further research in this field including micronozzle design improvement, additional research on serpentine microchannel curvature effects on heat transfer performance, research on other heat transfer models, etc.

Contents

Nomenclature

Abbreviations

Abbreviation	Definition
Atm	Atmospheric
CFL	Courant-Friedrichs-Lewy
DSMC	Direct Simulation Monte Carlo
FVM	Finite Volume Method
MEMS	Micro Electro Mechanical Systems
RGP	Real Gas Property
SIMPLE	Semi Implicit Method for Pressure Linked Equations
TAC	Thermal Accommodation Coefficient
TMAC	Tangential Momentum Accommodation Coefficient
VLM	Vaporizing Liquid Micro-resistojet
VOF	Volume Of Fluid

Symbols

Symbol	Definition	Unit
A_e	Nozzle exit area	[m^2]
$\frac{A_e}{A_t}$	Area ratio	[-]
Bo	Bond number	[-]
Co	Confinement number	[-]
C_d	Discharge coefficient	[-]
c_p	Specific heat capacity	[J/ kg K]
d_h	Hydraulic diameter	[m]
F	Thrust	[N]
g	Gravitational acceleration	[m/s^2]
Ga	Convective confinement number	[-]
G	Mass flux	[kg/m^{2}s]
h_{fg}	Latent heat	[J/kg]
$h_{l,sat}$	Saturated liquid enthalpy	[J/kg]
I_{sp}	Specific impulse	[-]
k	Thermal conductivity	[W/m K]
Kn	Knudsen number	[-]
M	Mach	[-]
M_w	Molecular weight	[g/mol]
$\dot{m}$	Mass flow rate	[kg/s]
p_a	Ambient pressure	[Pa]
p_e	Exit pressure	[Pa]
q_w	Heat flux	[W/m^2]
R	Universal gas constant	[J/mol K]
Re	Reynolds number	[-]
T_{sat}	Saturation temperature	[K]
$T_{sub,in}$	Inlet subcooling	[K]
T_f	Bulk fluid temperature	[K]
V_e	Nozzle exit velocity	[m/s]

Symbol	Definition	Unit
V_{eq}	Equivalent velocity	[m/s]
x_e	Thermodynamic quality	[-]
α_q	Volume fraction for phase q	[-]
η_F	Thrust efficiency	[-]
$\eta_{I_{sp}}$	Specific impulse efficiency	[-]
γ	Specific heat ratio	[-]
Γ	Vandenkerckhove parameter	[-]
λ_c	Condensation constant	[s^{-1}]
λ_e	Evaporation constant	[s^{-1}]
μ	Dynamic viscosity	[Pa s]
ρ	Density	[kg/m^3]
σ	Surface tension coefficient	[-]
θ	Contact angle	[°]

List of Figures

List of Tables

1

Introduction

The standardization of CubeSat by initiation of Puig-Suari at California Polytechnic State University and Twiggs at Stanford University, began the ever-increasing trend in development of small satellites. The aim of the project was to make space more accessible for students and educational institutions for purpose of experimentation, by reducing mission costs and development time [18]. However, for this very reason, CubeSats have also gained massive popularity in commercial and governmental agencies around the world. CubeSats are a class of nano-satellites (1-10 kg) with mass of about 1.33 kg. Structures of CubeSats are formed of a 10 cm unit cube (1U) and are defined as CubeSat of form factor 1U, 2U, 3U,etc. A similar concept of standardization called PocketQube has been developed recently, which is even smaller than CubeSat with a form factor of 5 cm x 5 cm x 5 cm.

With advances in miniaturization of payloads, capabilities of scientific instrument and manufacturing technology, these small satellites have gained a wide range of applications that were previously limited to larger satellites. Moreover, preferences for small satellites are seen for high performance missions, like formation flying, observation, and interplanetary missions. In order to realize these applications of small satellites, particularly for maneuverability and attitude control capability during formation flying, orbit transfer, and space debris removal [94] a necessity of miniaturization of propulsion subsystem was predicted by [79]. Following this trend of satellite miniaturization, Delft University of Technology has developed and flown its own PocketQube called Delfi-PQ. In future, Delfi-PQ is to accommodate one or more advanced payloads for technology demonstration. One of these is a micropropulsion technology demonstration payload [80]. Micropropulsion is a propulsion system that produces thrusts in the range of micro- to milli- Newton range, whose mass, size, and power consumption are restricted by the requirements of nano and pico satellites (0.1-1 kg).

The micropropulsion system focused on in this study is MEMS (Micro Electro Mechanical systems) vaporizing liquid micro-resistojet (VLM), where the liquid propellant is heated through resistive heaters in microchannels and vaporized to be accelerated through a micronozzle downstream. Flow behavior in microchannel and micronozzle is far from conventional. Extensive research on flow boiling in microchannels highlights the complexities associated with small-scale phenomena, which are typically absent in larger channels. Surface tension effects are much more prevalent in flow-boiling two-phase microchannels, whereas low-pressure rarefaction effects and viscous losses become important in micronozzles. Flow characteristics of the VLM flow are thus not intuitively measurable through empirical or semi-empirical methods. In the literature, different methods including analytical, experimental, and numerical approaches are applied to investigate the flow characteristics and performances of the microchannel and micronozzle. However, a coupled numerical analysis of the microchannel and micro nozzle is not frequently found, if any. Microchannel research mostly covers heat dissipation devices, which are concerned with high heat removal from heated surfaces. In two-phase flow boiling heat dissipation research, a liquid layer present between the heated wall and vapor core is always preferred rather than a complete dry-out of liquid, since liquid removes higher heat through evaporation than vapor. Whereas in VLM microchannels, the aim is to completely vaporize the liquid, which demands

higher heat flux and lower mass flow rate compared to heat sink microchannels. Such differences, although not big, mean results from heat dissipation microchannels can not be completely adopted to characterize the VLM microchannel heat transfer process. Furthermore, less or no readily available data on VLM microchannel models exist, whether that be experimental or numerical. Thus, in this study, a numerical method more detailed compared to an analytical method and needs fewer resources than the experimental method is to be applied in the coupling of the microchannel and micronozzle models. As such, the study aims to use the numerical approach to characterize the flow and performances of the complete VLM.

The next generation of MEMS VLM has been manufactured at TU Delft. The objective of this research is to evaluate the performance of next-generation MEMS VLMs by creating a numerical simulation model for the heater microchannel and micronozzle of the VLM and validating the model using existing experimental data. The research question is as follows:

How accurately can the heater microchannel and micronozzle of next-generation MEMS VLMs be numerically simulated to predict flow characteristics and assess VLM performance?

The sub-questions for the main research question are:

1. What are the flow characteristics and performance parameters that can be determined through numerical simulation of VLM heater microchannel and micronozzle?

2. Can a better accuracy on performance prediction be achieved by coupling the individual simulation of VLM heater microchannel and micronozzle?

This report presents the research results as follows. In chapter 2 fundamental theory related to microchannel and micronozzle flow is introduced. The numerical approach, modeling setup used and results in the microchannel simulation are explained in chapter 3. Additionally, the numerical coupling problem of microchannel and micronozzle components is discussed in the chapter. Likewise, in chapter 4, micronozzle modeling method and results are discussed and chapter 5 provides the conclusion and recommendation for further research.

2

Fundamentals

Research in the field of VLM microchannels is limited, however, microchannels in heat sink technologies are widely utilized and researched by many. As more power-dense devices are developed, the demand for advanced heat dissipation technologies utilizing phase change microfluidic with superior heat transfer performance compared to single-phase flows has grown significantly. Yet, the study of two-phase flow in microchannels continues to be a complex phenomenon. Despite these challenges, this research aims to characterize the VLM microchannel by applying insights from cooling device technology.

2.1. Microchannel

In the following section, different aspects of flow boiling in microchannels are explained.

2.1.1. Definition of microchannel

Certain thermal and fluid phenomena, like gravity and surface tension effects, are present at varying levels of importance in macro-scale and micro-scale channels. For instance, in two-phase (liquid and vapor) microchannel flow, as the channel size decreases, gravity effects become less important to non-existing.[97] An example of gravity effects is evident in Figure 2.1, where a thick liquid layer at the bottom and a thin liquid layer at the top of the elongated bubble is visible for a diameter of 2 mm channel. The gravity effect is no longer visible as the channel size is decreased to 0.509 mm with a constant thickness of liquid layer present around the bubble. Because, in microchannel confined flow, the surface tension forces dominate, suppressing the gravity-driven buoyancy force effects responsible for the rise of bubble as seen in conventional sized channels.

Indeed, differentiating microchannel from conventional macrochannel is fundamental in studying its flow characteristics. No universally acknowledged criteria exist, along with inconsistent naming conventions for small/mini/microchannels, but various researchers have provided definitions for microchannels across the literature. A size category frequently used to identify microchannel is that of Kandlikar and Grande [48], the scale is based on hydraulic diameter, d_h, defined as follows:
Conventional Channels: d_h > 3 mm
Minichannels: 3 mm ≥ d_h > 200 μm
Microchannels: 200 μm ≥ d_h > 10 μm

According to Thome [98], a size-based criterion does not account for the impact of channel size on physical mechanisms. Thome had cautioned, that such a macro-scale to micro-scale transition could depend on the bubble departure diameter, described as the size of the bubble when it leaves the nucleation site and flows downstream of the channel. As the bubble grows, and compares to the size of the channel diameter before departure, the bubble growth is confined by the channel, which entails an increase in bubble length but confinement in the diameter direction. In this condition, only a single
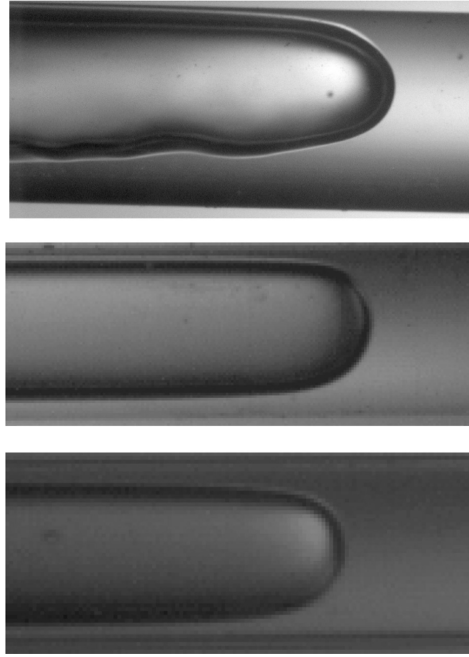
Figure 2.1: An elongated bubble flow in circular channels of different diameters: 2 mm (top), 0.790 mm (middle), and 0.509 mm (bottom) [97]

bubble can exist in the channel. This point at which the bubble is confined is considered a microscale threshold.

Other researchers have distinguished between macro and microchannel depending on several dimensionless numbers. Confinement number, Co, proposed by Kew and Cornwell [51] expresses the ratio of surface tension forces to gravity in Equation 2.1, where σ = surface tension coefficient, g = gravitational acceleration, ρ_L = density of liquid, ρ_V = density of vapor and d_h = hydraulic diameter. The microscale flow threshold was set at Co = 0.5 with the microchannel exceeding Co > 0.5.

$$Co = \sqrt{\frac{\sigma}{g(\rho_L - \rho_V)d_h^2}} \tag{2.1}$$

Cheng and Wu [27] applied the Bond number (Bo) to categorize microchannels, specifying those with Bo < 0.05. The Bond number is defined as the ratio of gravity to surface tension forces, Equation 2.2. A lower value of bond number for two-phase flows indicates that surface tension forces are dominant, as explained previously.

$$Bo = \frac{g(\rho_L - \rho_V)d_h^2}{\sigma} \tag{2.2}$$

Lastly, convective confinement number had been introduced by Harirchian and Garimella [41] and represented as Ga, based on the empirical relation given in Equation 2.3, where, $Bo^{0.5} \times Re_L$ = convective confinement number, Re = Reynolds number = $\frac{GD}{\mu}$, μ_L = liquid dynamic viscosity, G = mass flux (ratio of mass flow rate to cross-sectional area) and D^2 = cross-sectional area of a microchannel. This criterion was established based on the understanding that bubble confinement is affected by both channel size and mass flux. A value of Ga < 160 indicates a microchannel where confinement of vapor bubbles is present. A macro-to-micro transition based on flow behavior is shown in Figure 2.2.

$$Bo^{0.5} \times Re_L = \frac{1}{\mu_L}\left(\frac{g(\rho_L - \rho_V)}{\sigma}\right)^{0.5}GD^2 = 160 \tag{2.3}$$
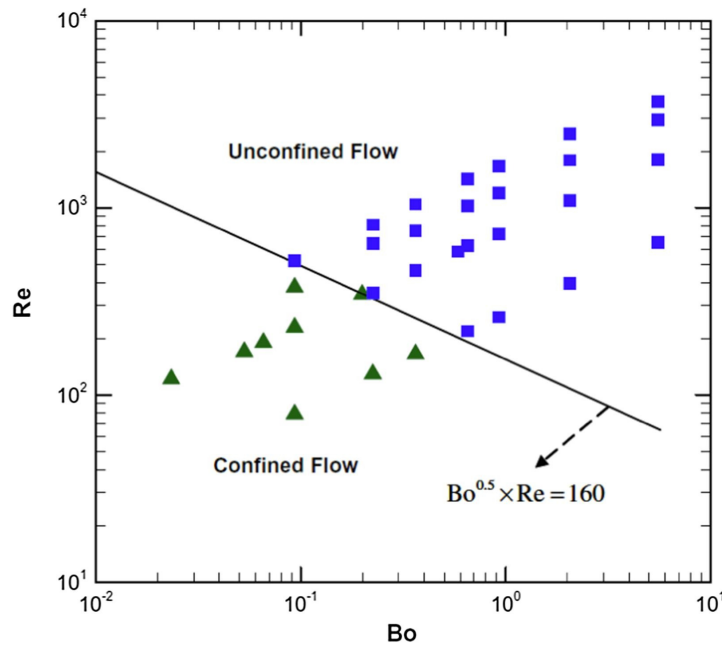
Figure 2.2: Flow transition from unconfined to confined based on experimental observation by Harirchian and Garimella [41]

2.1.2. Flow regimes

Many experimental observations have identified several flow patterns in flow boiling microchannels in recent years.[42] [19] [100] [2] Flow patterns and their transitions in microchannels are influenced by multiple factors, including channel size, bubble growth dynamics, flow rates, heat fluxes, fluid properties, operating conditions, etc. making the process complex. Regardless of slight differences in the form of flow regimes caused by such factors, there are five common flow regimes observed in two-phase flow boiling in microchannels as shown in Figure 2.3 and described below:

- **Bubbly flow**: discrete vapor phase or bubbles smaller than the cross-section of the microchannel are present in the liquid flow.
- **Slug flow**: elongated confined vapor bubbles separated from the wall by a thin liquid layer fill the entire microchannel cross-section. Liquid slugs containing small bubbles are present between the elongated bubbles.
- **Churn flow**: distinguished from slug flow by the deformed vapor bubbles smaller than microchannel diameter, due to the breakdown of elongated vapor bubbles caused by increased gas velocity.
- **Wispy-annular flow**: a thick liquid film separates a large vapor core from the microchannel wall and contains irregularly shaped liquid droplets.
- **Annular flow**: a vapor core is divided from the wall by a thinner liquid film, compared to a wispy-annular, with potentially a wavy liquid-vapor interface. Moreover, the vapor core contains small spherical liquid droplets dispersed within it, and the liquid film shows no visible vapor bubbles.

Among multiple flow regime transition maps found in literature, Figure 2.4 presents a comprehensive map for the flow regimes. Four different flow regimes are identified based on around 390 experimental data points using coolant Fluorinert FC-77, for various channel dimensions, mass fluxes and a range of heat flux 25–380 kW/m^2. Here, $Bl \times Re = 0.017$ $(Bo^{0.5} \times Re)^{0.7}$ in the y-axis denotes a non-dimensional heat flux term resulting in $Bl = 0.017(Bo^{0.4} \times Re^{-0.3})$. The x-axis is the convective confinement number, Ga, explained above. As observed, confined slug and churn/confined annular flow regimes exist in microchannel for Ga < 160 shown by the vertical limit line. Similarly, the transition line $Bl < 0.017(Bo^{0.4} \times Re^{-0.3})$ shows that confined slug and bubbly flow are found in microchannels with lower heat fluxes whereas at $Bl > 0.017(Bo^{0.4} \times Re^{-0.3})$, churn/annular and churn/wispy-annular flow regime is mostly observed.
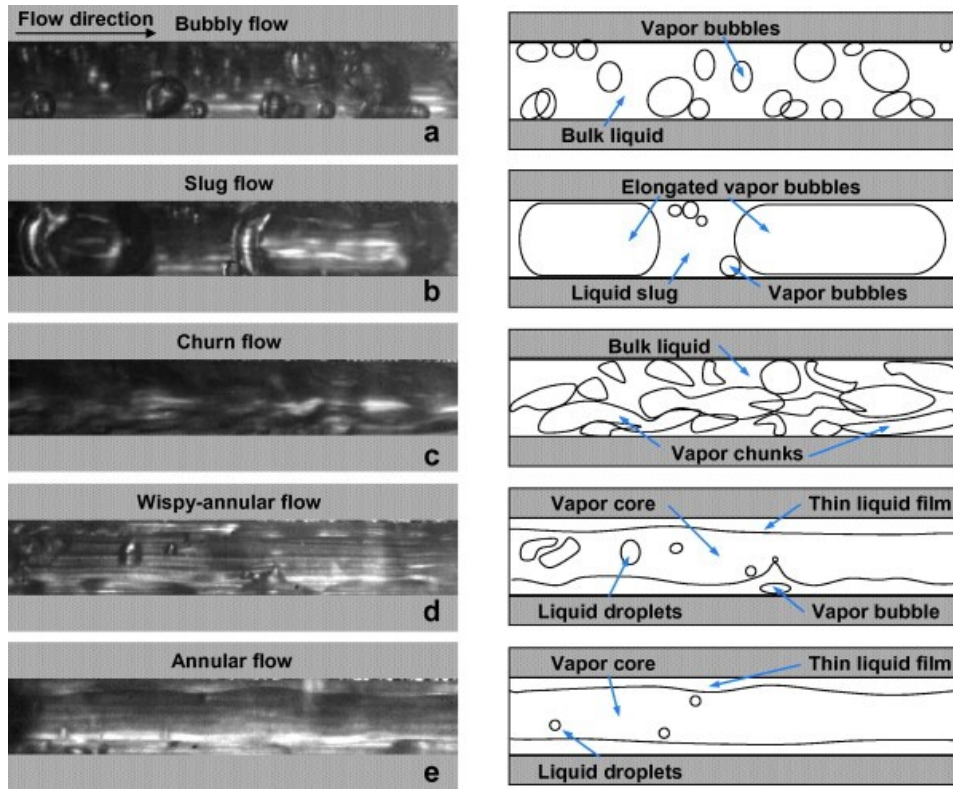
Figure 2.3: Flow boiling regimes identified in microchannel [42]
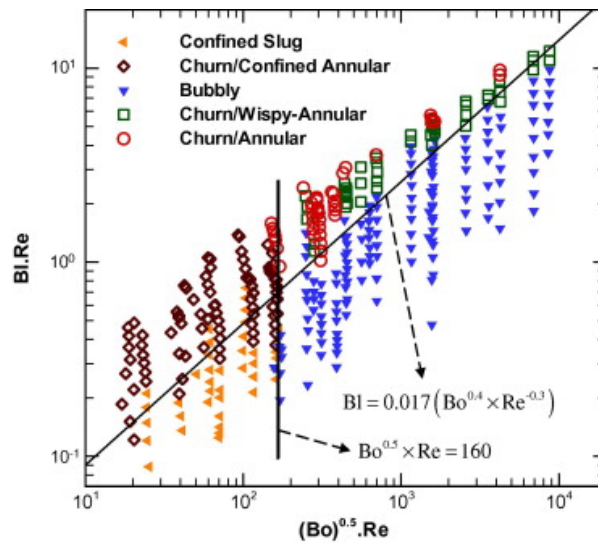
Figure 2.4: Flow regime transition as function of heat flux term and convective confinement number established in [41]

2.1.3. Flow boiling in microchannel

Boiling offers a method to utilize the latent heat of vaporization to remove heat from heated surfaces at a higher rate. Pool boiling refers to the process of boiling occurring from a heated surface that is submerged in a substantial volume of stagnant liquid. The study of pool boiling is fundamental in the flow boiling heat transfer research.[47] Boiling that occurs when fluid flows over a heated surface driven by either an external pump or buoyancy forces is referred to as flow boiling and is the focus of this research.[102] The following subsections explain the fundamentals of flow boiling and heat transfer mechanisms in microchannels.

Subcooled and saturated flow boiling

Flow boiling covers two regimes, including subcooled and saturated boiling, with both further subdivided into their sub-regimes.[29] Subcooled boiling occurs in a heated channel when the fluid's bulk is below the saturation temperature (T_{sat}), known as subcooled fluid. Both subcooled and saturated boiling can exist over a heated microchannel length, given that the fluid delivered at the inlet is below the saturation temperature for the inlet pressure. As the bulk fluid attains the saturation temperature over a certain length of the microchannel, saturated boiling takes place.

In subcooled boiling, nucleation sites are present in the heated wall, where the adjacent superheated (higher than saturation temperature) fluid causes the formation of bubbles. Subcooled boiling denotes the transition region from single-phase heat transfer to saturated boiling. A schematic of the transition process is shown in Figure 2.5. According to Collier and Thome [29], two divisions can be seen in the subcooled boiling region. The highly subcooled boiling zone starts with the onset of nucleate boiling (ONB), which is the point where the bubbles start to nucleate. After reaching their maximum size, bubbles depart from the nucleation site, represented as the point of bubble departure, z_{bd}, floating onto the subcooled bulk where bubbles experience partial or complete condensation. Heat transfer sources in the bubble nucleating region of subcooled boiling are identified as evaporation at the micro-layer beneath the bubble and superheated liquid layer, condensation in the bubble-subcooled liquid interface, and transient heat transfer.[113] [60] In Figure 2.5, T_{sat} = saturation temperature, inlet subcooling, $T_{sat} - T_{in} = \Delta T_{sub,in}$, T_w = wall temperature, T_f = bulk fluid temperature, ϕ = fluid phase, q'' = heat flux and rest as follows from the preceding.

The location, where thermodynamic quality, x_e = 0, sets the beginning of the saturated boiling flow. x_e can be computed by Equation 2.4, where, h_e = exit fluid enthalpy, $h_{l,sat}$ = saturated liquid enthalpy, and h_{fg} = latent heat of the liquid. This corresponds to a negative value for x_e in subcooled flow boiling.[117]

$$x_e = \frac{h_e - h_{l,sat}}{h_{fg}} \qquad (2.4)$$
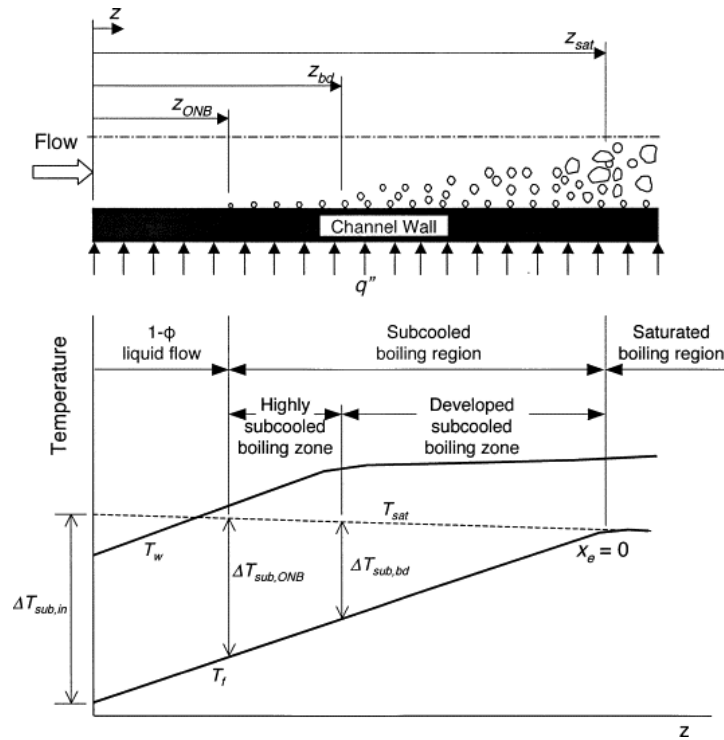
Figure 2.5: Single phase to saturated boiling transition [60]

In subcooled boiling, only bubbly flow is seen to persist.[59] On the contrary, in saturated boiling,

a rapid transition from bubbly to slug, churn, and annular flow regimes can be observed, induced by a high void fraction in saturated boiling (defined as the proportion of the channel's cross-sectional area that is occupied by the gas or vapor phase relative to the total cross-sectional area of the channel). Because of the disparities in void fractions, the heat transfer mechanism in saturated boiling differs from subcooled boiling.[61] Heat transfer in subcooled boiling consisting of bubbly flow regime is influenced by nucleate boiling where nucleated bubbles carry the heat transferred via superheated liquid close to heated wall. Once the bubbles depart, they condense into the cooler bulk liquid. In [61] at $x_e < 0.05$ and low heat fluxes, bubbly flow and nucleate boiling is reported as the main heat transfer mechanism. Similarly, according to [99] the bubble motion is said to increase the liquid convection leading to improved convective heat transfer. Likewise, saturated boiling heat transfer can be further divided into the contribution of nucleate and convective boiling components. Since saturated boiling is the main focus in this study, heat transfer mechanisms of saturated flow boiling components in a microchannel are discussed in the next subsection 2.1.4.

2.1.4. Saturated flow boiling heat transfer

Saturated flow boiling heat transfer processes are stated to be governed by nucleate boiling and convective boiling components, which are associated with heat transfer coefficients and flow patterns. Nucleate boiling involves the formation of bubbles at the heated surface, their growth, and departure. Convective boiling is related to heat transfer through conduction and convection in the liquid film and evaporation at the liquid-vapor interface.

It has been evident from several experimental investigations in conventional channels over the years that nucleate boiling is dominant when there is a strong dependency on heat flux and saturation pressure, while essentially independent of mass flux and vapor quality. On the other hand, an increase in heat transfer coefficient with an increase in mass flux and vapor quality signaled the dominance of convective heat transfer.[39] [65] [28] [111] Figure 2.6 shows the flow regimes transition throughout the heated length of microscale channel and corresponding dominant heat transfer mechanism for nucleate boiling and convective boiling. Furthermore, for nucleate boiling dominant heat transfer, most of the channel consists of bubbly and slug regimes whereas the annular flow takes over a large part of the channel in convective boiling dominant heat transfer.

A lot of researchers have proposed correlations to fit the experimental data for saturated flow boiling heat transfer in conventional channels. According to Fang et al. [33], these correlations could be categorized into seven types including enhancement factors, superposition, asymptotic, the largest mechanism predominant, nucleate boiling, flow pattern-based, and hybrid types. For example, Chen [25] had well formulated a heat transfer coefficient correlation based on the superposition model, taking the sum of the contribution of nucleate boiling and convective boiling mechanism.

Similar attempts have been made to compare the experimental data to the macro-scale flow boiling correlations to predict the heat transfer in the microchannel saturated flow boiling process. However, the existing heat transfer prediction method is unable to predict the heat transfer data in microscale channels.[88] [26] Moreover, there are significant differences in the experimental observations obtained from different authors who conducted experiments under the same test conditions. For just one example, Ribatski, Wojtan, and Thome [88] had mentioned in their review a discrepancy in the experimental results of flow boiling heat transfer in a microscale channel from two different researchers. They had experimented with almost similar conditions, but as seen in Figure 2.7, Kim, Sim, and Min [52] data shows an increase in heat transfer coefficient from 3 to 8 kW/m^2 for vapor quality of 0.2 to 0.8, whereas no such trend is visible from experimental data of Bang and Choo [11] with more or less same value of 2 kW/m^2. In the experiment of Kim, Sim, and Min, a square cross-sectional microchannel was used whereas in Bang and Choo's experiment, microchannel had a circular cross-section. It has been assumed that surface tension effects could cause the liquid layer around the bubble to thicken at corners of square cross-section and a thinner layer to be formed in the region away from the corners. This would cause higher evaporation rate at the liquid-vapor interface, which is much closer to the heated wall, leading to an increase in the heat transfer coefficient for a square cross-sectional microchannel of Kim, Sim, and Min. However, the large disparity between the two outcomes still could not be interpreted by such speculations.

Heat transfer in microchannel flow boiling is a complex phenomenon that can not be completely
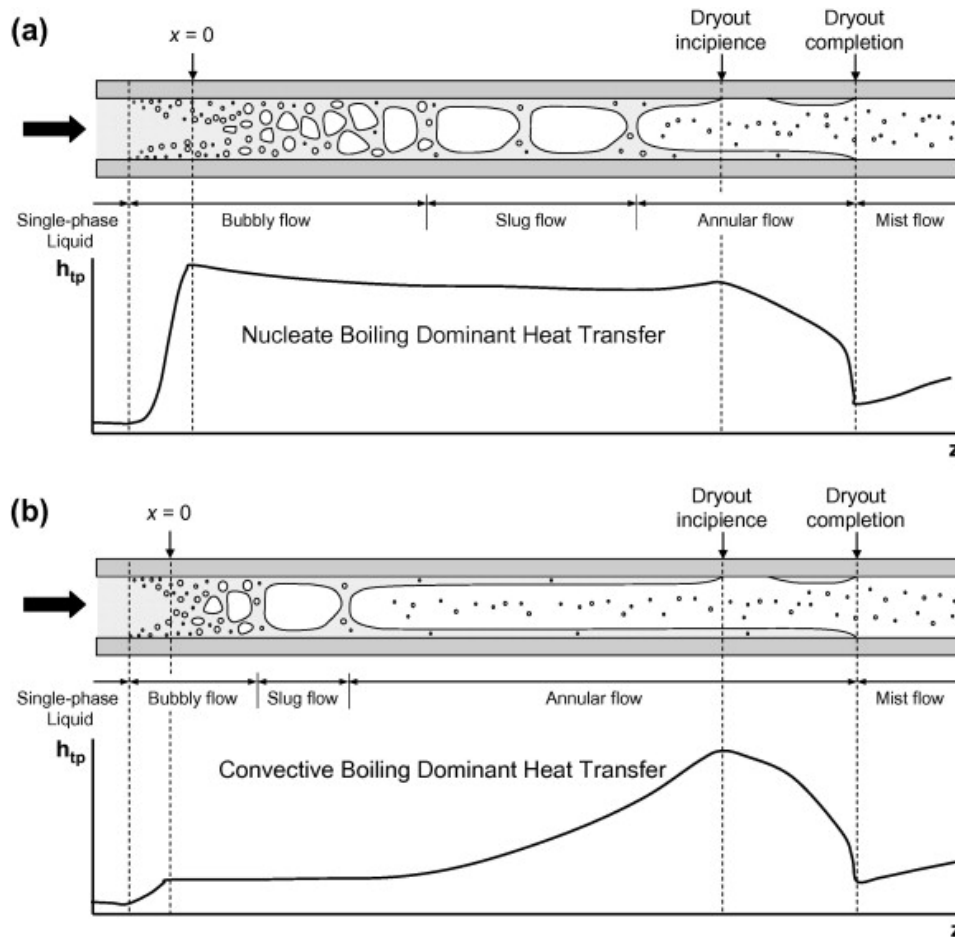
Figure 2.6: Change in two-phase heat transfer coefficient (h_{tp}) depending on the dominant heat transfer mechanism and flow regime variation over the heated length of micro-scale channel [53]

explained by the two mechanisms presented above. Nevertheless, several experiments as well as models have attempted to explain the heat transfer mechanism in microscale flows. However, none have reached an agreement as to which mechanism of heat transfer is dominant. Kandlikar [45] had noted that heat transfer in microchannels was nucleate boiling dominant and there were no effects of the convective boiling mechanism. In [46] however, Kandlikar explained the heat transfer mechanism compared to the nucleate pool boiling heat transfer. It was cautioned that convective contribution in flow boiling microchannels cannot be overlooked because of the non-dependence of heat transfer coefficient to mass flux. It has been assumed that heat transfer increases with mass flux for turbulent flows. Since the microchannel liquid flow is laminar, the heat transfer coefficient is independent of the mass flow rate.

In both pool boiling and microchannel flow boiling, microlayer evaporation, transient conduction, and microconvection were identified as the three main modes of heat transfer. During the bubble growth period in pool boiling, a bubble nucleated at the heated surface grows by evaporation of a microlayer formed beneath the nucleating bubble. The evaporating microlayer could leave a dry patch at the center due to its depletion, resulting in a very low heat transfer in that area. Upon the departure of the bubble, the cooler liquid flows into the heating surface previously occupied by the dry patch. Through transient conduction, a superheated liquid layer is formed at the heated surface where a new vapor bubble is nucleated again, repeating the cycle. Heat is then released by the superheated liquid at the evaporating interface (receding liquid-vapor interface) through microconvection. A nucleating bubble growth cycle in pool boiling can be seen in Figure 2.8.

In microchannel flow boiling, the bubble grows into an elongated bubble (slug pattern) by evaporation of the bulk liquid-vapor interface, and liquid slugs are formed in between the elongated bubbles.
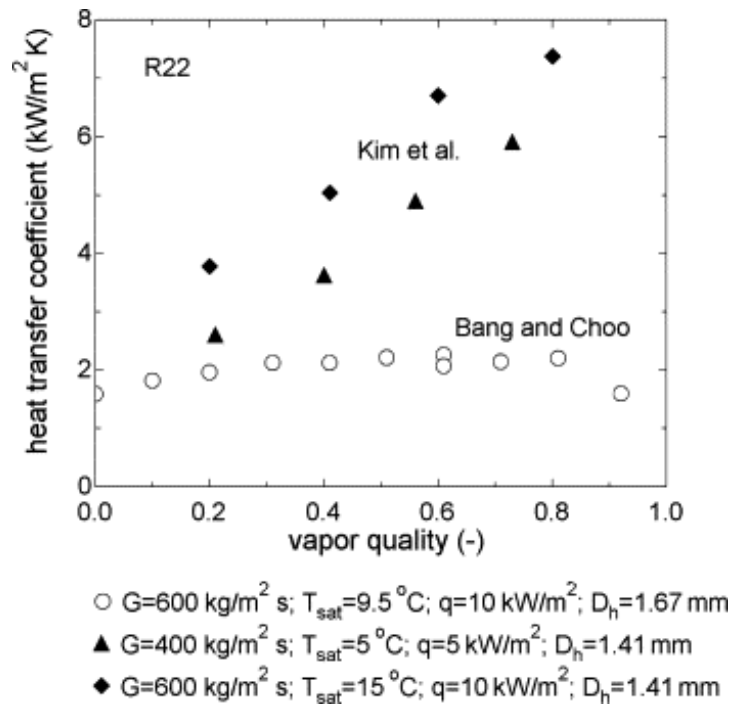
Figure 2.7: Heat transfer coefficient and vapor quality, from experimental results of Kim, Sim, and Min [52] and Bang and Choo. [11] [88]
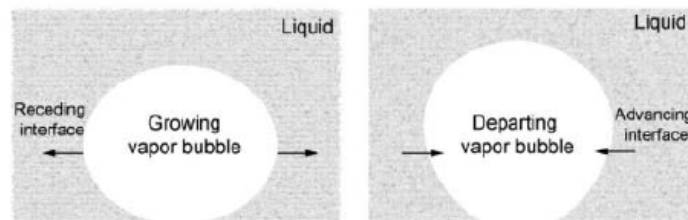
Figure 2.8: A bubble growth cycle in pool boiling [47]

Similar to pool boiling, a microlayer is formed in the heated surface region around the elongated bubble. The receding interface during bubble growth and advancing interface during the departure phase in pool boiling (Figure 2.8) corresponds to the downstream and upstream liquid-vapor interface of elongated bubble respectively in the microchannel, as is shown in Figure 2.9. The heat transfer in the liquid slug is described as complicated, particularly due to transient conduction at the wall and evaporation at the receding interface from microconvection.
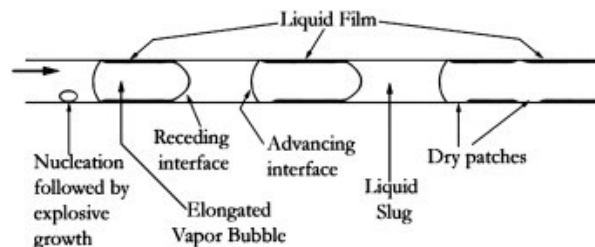
Figure 2.9: Elongated bubbles in microchannel flow boiling with interfaces similar to nucleate pool boiling receding and advancing interface [47]

An experimental study on flow boiling in a microchannel by Bigham and Moghaddam [16] similarly identified three heat transfer mechanisms for elongated bubble (slug flow) patterns in the microchannel.

Based on their analysis of the heat flux data of a sensor, variation in heat flux as an elongated bubble moves past a sensor is seen in Figure 2.10. Heat flux peaks when the bubble front passes through the sensor, where the thin film (microlayer) evaporation is the source of heat transfer. The decline in the heat flux, reaching a value lower than the single phase line, is due to the complete evaporation and dry-out of liquid towards the rear of the bubble. After this decline, a rapid increment in heat flux denotes re-wetting of the dried surface by liquid slug, where an extremely heated surface due to vapor contact causes high heat transfer to the liquid through transient conduction. At both sides of the bubble, within the liquid slugs, microconvection with higher heat transfer than single-phase can be seen. Karayiannis and Mahmoud [49] had speculated nucleate boiling to be dominant, given the similarity of thin film evaporation compared to the nucleate pool boiling microlayer evaporation process.
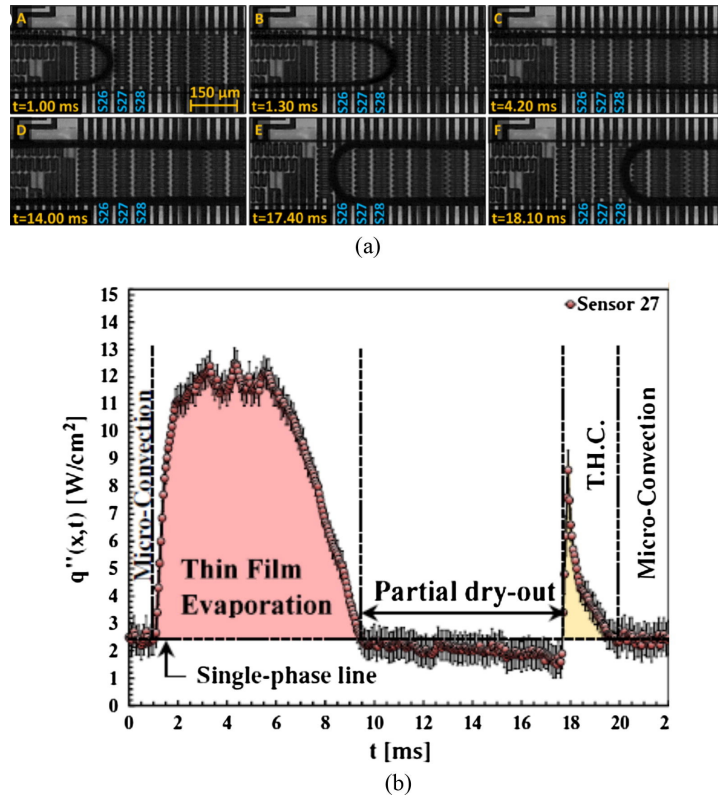
Figure 2.10: (a) Elongated bubble flow along the microchannel over time, with (b) corresponding heat transfer mechanism and heat flux measured at temperature sensor [16]

A significant body of research, including works by [58], [12], [61], [9], has identified nucleate boiling as the dominant heat transfer mechanism. In contrast, others, such as [44] [87], [78], [5], have concluded that convective heat transfer is predominant in microchannels. Overall, there is still no consensus on the primary heat transfer mechanism in these studies.

2.1.5. Relevance to VLM microchannel

The literature study on flow boiling in heat dissipation microchannel presented significant findings relevant to VLM microchannel flow. Based on the definition of the microchannel non-dimensional numbers, in subsection 2.1.1, the channels in VLM can be categorized as microchannel explained in section 3.1. From the above discussion, it is known that the VLM microchannel exhibits saturated flow for most of the microchannel length, depending on the degree of subcooled flow at the entrance. VLM microchannel confined bubble flow characterized by an elongated bubble known as slug flow covering the entire microchannel cross-section is expected. Although not desired in cooling microchannels, complete dry out of the VLM microchannel is anticipated by merging of the elongated bubbles to form annular flow. Further, complete vaporization is expected because of the high heat flux and lower mass flow rate associated with the VLM microchannel flow.

It was realized that much of the research literature still struggles to agree on the dominant heat transfer mechanism of the microchannel. Two heat transfer methods were recognized, nucleate and convective. Nucleate heat transfer is related to the bubble nucleation, growth, and departure from the nucleation sites. During this time, heat is released through a phase-change process at the microlayer formed underneath the nucleating bubble. After departure, the conduction of heat forms a superheated liquid, and the cycle of new bubble formation and release of heat at the interface continues to occur. In conventionally sized channels, the increase in the heat transfer coefficient with increase in heat flux relates to the dominance of nucleate boiling. However, dependence on mass flux is directly linked to the dominance of convective boiling. In convective boiling, heat is transferred via evaporation at the already formed bubble-liquid interface. For slug flow regimes, a similar microlayer evaporation process supplemented by complexities of conduction and microconvection in the liquid slugs was presented. Also, heat transfer coefficients measured through experimental data, and its unpredictability was pointed out. Thus, the findings will be used in this study to characterize the VLM microchannels, including their heat transfer characteristics and to explain the heat transfer process rather than determining which boiling heat transfer mechanism is dominant in the VLM microchannel flow. The results on heat transfer coefficients are influenced by numerous factors including heat flux, mass flux, degree of inlet subcooling, microchannel cross-section, etc. which mandates a detailed data analysis. Determining the major heat transfer mechanism in the VLM microchannel is thus out of scope in the current study.

2.2. Micronozzle

There is no distinctive measure of differentiating a micronozzle from conventional nozzles. But in the literature, micronozzles are generally referred to as small-sized nozzles generating thrust in scale of μN-mN operating at Reynolds numbers of 10 to 10^3. Conventional nozzles are in the range of Reynolds $>>$1000. At the microscale, viscous effects, flow transition characteristics, and related factors play a significant role. Micronozzles are thus characterized by the low Reynolds number and associated flow characteristics. This study focuses on MEMS-based micropropulsion systems.

2.2.1. Space propulsion

This section presents the basic theory on the performance of space propulsion systems.

Nozzle flows

The thruster or rocket engine consists of two important parts: chamber and nozzle. In the chamber, high energy and high-pressure gases are generated, which are fed to the nozzle. The nozzle consists of a convergent and divergent section, which accelerates the gases flowing from the chamber and expels them to space at high velocities to produce thrust. The minimum area between the convergent and divergent sections of the nozzle is called the nozzle throat, the area at the end of the nozzle is called the nozzle exit area, and the area at the beginning of the nozzle is called the nozzle inlet area, Figure 2.11. [118]
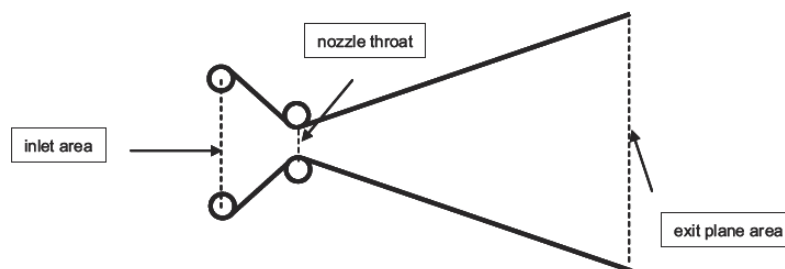
Figure 2.11: Nozzle shape
[118]

The shape of the nozzle is determined by an area-velocity relation, Equation 2.5, where, M = flow Mach number, u = flow velocity, and A = nozzle cross-sectional area.

$$(1 - M^2)\frac{du}{u} = -\frac{dA}{A} \tag{2.5}$$

Area-velocity relation is derived for a compressible isentropic flow through a nozzle, based on laws of conservation of mass, energy, and Poisson relation [118]. According to this relation, to accelerate a subsonic flow (M < 1) at rest to supersonic velocities (M > 1), the flow must be subsonically expanded through a convergent duct (flow velocity increases with a decrease in cross-sectional area), until it reaches sonic velocity (M=1) at the minimum area throat. Next, the flow should be further expanded through a diverging duct (flow velocity increases with an increase in cross-sectional area) to reach supersonic speed.

Propulsive Performance

The performance of propulsive systems/thrusters is measured by two performance parameters: thrust and specific impulse. Thrust is a force generated by propulsion system to push the spacecraft/rocket forward. Thrust is given by rocket thrust equation in Equation 2.6, where F = thrust, $\dot{m}$ = propellant mass flow rate, V_e = nozzle exit velocity, p_a = ambient pressure, p_e = exit pressure and A_e = nozzle exit area.

$$F = \dot{m} \cdot V_e + (p_e - p_a) \cdot A_e \tag{2.6}$$

As seen in Equation 2.6 thrust has two contributions given by a "momentum term" and a "pressure term". Depending on the difference, $(p_e - p_a)$, between pressure at nozzle exit p_e and ambient pressure p_a, the pressure term can be either positive, zero or negative. Zero pressure term would mean the pressure at nozzle exit equals the surrounding ambient pressure, this is called an optimum nozzle expansion or adapted nozzle. The adapted nozzle is referred to as a nozzle with optimum expansion ratio, as the nozzle design allows maximum thrust to be achieved when p_e = p_a. This relation can be derived mathematically by taking the derivative of the thrust equation, Equation 2.6. Similarly, the positive pressure term refers to under expansion and the negative pressure term refers to overexpansion.

In the case of an adapted nozzle, the thrust equation can be written as F = $\dot{m} \cdot V_e$, but optimum expansion is not always possible although desired. So thrust is often written in terms of equivalent velocity as Equation 2.8.

$$V_{eq} = V_e + \frac{(p_e - p_a)}{\dot{m}} \cdot A_e \tag{2.7}$$

$$F = \dot{m} \cdot V_{eq} \tag{2.8}$$

Specific impulse is a measure of total impulse produced divided by the weight of propellant, Equation 2.9. A higher specific impulse would mean, that the rocket or spacecraft can produce a given amount of thrust with lower propellant consumption.

$$I_{sp} = \frac{\int_0^t F \cdot dt}{g_0 \cdot \int_0^t \dot{m}dt} \tag{2.9}$$

For a constant mass flow and equivalent velocity over time, I_{sp} is given by Equation 2.10.

$$I_{sp} = \frac{V_{eq}}{g_0} \tag{2.10}$$

2.2.2. Micronozzle performance

Small scale and low-pressure levels in micronozzle results in lower Reynolds number than in conventional sized nozzles. At lower Reynolds number, low thrust micronozzle suffers with thick viscous boundary layer at the divergent sections and associated performance degradation which are normally negligible for conventional sized nozzles. This means 1D isentropic assumption does not provide good prediction for the micronozzle performances.

In micronozzles, the thick viscous boundary layer formed at the divergent section wall often causes blockage of the flow and reduces the effective area ratio. This causes the actual mass flow rate to be lower than the predicted mass flow rate based on the geometric throat area. The discharge coefficient C_d captures this effect. A thick viscous boundary layer also tends to slow down the flow in the vicinity of the wall, turning the flow subsonic close to the wall. It allows disturbances to flow upstream from the exit towards the throat, potentially leading to flow separation. Viscous effects thus cause significant performance losses and are important to account for in the design of VLM micronozzle.

In this regard, various experimental procedures have been adopted to measure performances of micronozzles. Rothe [89], had experimented with nitrogen gas as propellant to investigate the flow in convergent-divergent nozzle with throat diameters of 5 mm and 2.5 mm. Nozzle discharge coefficient (C_D), which refers to the ratio of actual mass flow rate to the ideal mass flow rate, was also presented for Reynolds number in the range of 10^2 to 10^3. A decrease in C_D from 0.9 to 0.75 was shown for Reynolds number decrease from 1000 to 100. Similar reduction in the thrust and specific impulse efficiency (actual thrust and specific impulse compared to ideal thrust and specific impulse of 1D isentropic flow respectively) with decrease in Re < 1500 was demonstrated by the nitrogen gas experiments conducted by Bayt [13]. Torre [103] had also specified that the nozzle with thrust in the range of 1 mN incurs performance loss of about 10% due to viscous effects.

Number of studies haven been performed to optimize the micronozzle design in order to mitigate the effects of viscous boundary layer. Experimental data of Williams and Osborn [107] indicated that using a higher divergence angle, and smaller area ratios improved the nozzle efficiencies. Using a higher divergence angle for the same area ratio results in smaller length of the micronozzle. Consequently, reducing the length over which the viscous boundary layer growth can develop. Although higher divergence angle lowers the viscous effects, it also reduces the flow alignment at the exit of micronozzle. This would lead to geometric losses due to increase in traverse velocity component, affecting the thrust production.

Micronozzle geometry such as aerospike designs were also considered for improved performance. Unlike linear conical nozzles, aeropspike nozzle flow expansion is not bounded by the walls, as shown in Figure 2.12. In numerical analysis of Pearl, Louisos, and Hitt [84], both 2D and 3D aerospike micronozzles showed improvement in specific impulse efficiency by 0.15, compared to a 3D linear micronozzle at similar depths.

Torre had also concluded that wall surface roughness accounts for 18% of performance degradation due to the formation of weak shocks at the micronozzle divergent section. As such, the micronozzle performances are affected by several parameters like size, area ratio, geometry, divergence angle and surface roughness. Although investigation in effects of such parameters are not intended in the current study, they will be important to characterize the micronozzle performances. Thus, for successful operation, the performance of the micronozzle must be evaluated with greater accuracy than is possible using 1D isentropic flow assumptions.

2.2.3. Micro Electro Mechanical Systems (MEMS) micropropulsion

In this segment, overview of different micropropulsion concepts and few examples of MEMS micropropulsion systems developed are discussed based on [93], [23] and [66]. It is to be taken into account that MEMS devices like sensors can be a part of a larger system. However, MEMS micropropulsion considered in the following are thrusters that are entirely manufactured on silicon with MEMS technology. MEMS fabrication technology allows manufacturing an array of identical dies/chips onto a single wafer. Based on [67] and [37], in general, fabrication processes can be grouped into major categories
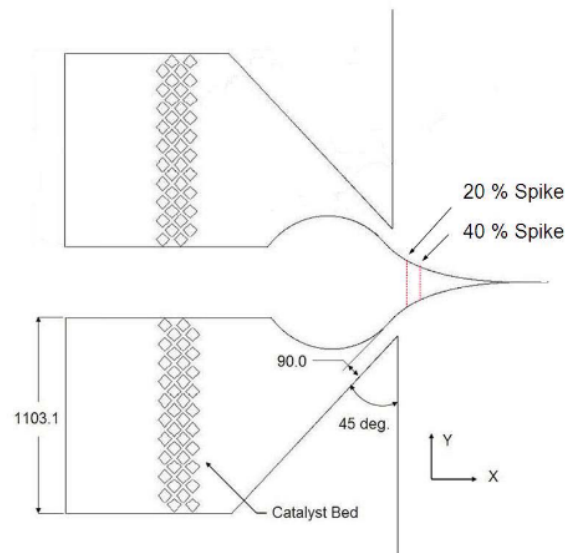
Figure 2.12: Aerospike nozzle countour
[120]

including

- Patterning (photolithography): used to transfer a pattern through a mask onto a photoresist layer using light.
- Additive processes (thin film deposition, thermal oxidation of silicon): used to deposit (semi)conductors, dielectric materials, insulator etc. on a wafer.
- Subtractive steps (wet etching, silicon anisotropic etching, plasma etching, and reactive ion etching): used in selective and controlled removal of material from a surface.
- Material modification (doping): used to alter the electrical properties of a semiconductor. In MEMS devices, typically used to form an electrically conductive layer such as a heater.
- Mechanical steps (wafer dicing, wafer bonding): dicing is used to separate dies in a single wafer to get individual chips and bonding is used to bond two wafers together.

According to [92], the category representing MEMS micropropulsion are:

Cold-gas microthrusters: This propulsion system generates thrust by accelerating pressurized gas propellant to high velocities through a converging - diverging nozzle. A complete MEMS cold gas propulsion system with 4 thrusters, providing a maximum thrust of 1 mN and specific impulse of 68 s per individual thruster with butane propellant, is developed by [56].

Solid propellant microthrusters: A solid propellant thruster produces thrust by combustion of solid propellant, referred to as grain. A planar-type solid propellant microthuster was fabricated with MEMS technique in [119].

Liquid propellant thrusters: This type of propulsion system typically has propellant stored in a liquid phase pressurized by a pressurant gas, that is transferred to a combustion chamber, where chemical energy is released to generate hot reaction gases. The hot gases enter the converging-diverging nozzle, where they are expanded and accelerated to high exhaust velocity to generate thrust. In [109], the design, fabrication, and testing of a liquid propellant microthruster using low-temperature co-fired ceramic (LTCC) tapes are introduced.

Electrospray thrusters: Electrospray thrusters use liquid propellant, either ionic liquid or liquid metal, to accelerate ions due to an electric field produced by a single extraction grid electrode. [23]. [31] has developed a MEMS electrospray microthruster that consists of an array of capillary emitters (213 emitters cm^{-2}) with integrated extractor/accelerator electrodes.

Micro-resistojets: In resistojets, propellant stored in either solid, liquid, or gaseous phases are heated electrically with resistance and accelerated to high velocities through a nozzle. Depending on the type of phase change that occurs, two types of resistojets can be identified, vaporizing liquid micro-resistojets (VLM) and low-pressure micro-resistojets (LPM). VLM uses liquid propellant, where phase change from liquid to gas occurs before accelerating it in a convergent-divergent nozzle. LPM or Free Molecule Micro-Resistojet (FMMR) works in very low-pressure range with the conventional converging-diverging nozzle removed. Instead, gas particles are accelerated by the collision of propellant particles with high-temperature walls of an expansion slot. A recent development of water-based MEMS VLM can be found in [57].

The focus of this research lies on the vaporizing liquid micro-resistojets (VLM), the context of which is discussed further in the following sections.

2.2.4. MEMS VLM research at TU Delft
The first MEMS VLM development at TU Delft dates as early as 2011 by Mathew [72]. The design as shown in Figure 2.13 used an integrated aluminum thin-film heater based on silicon wafer technology. Propellant enters from an inlet and is heated by the heater while flowing through a single channel.
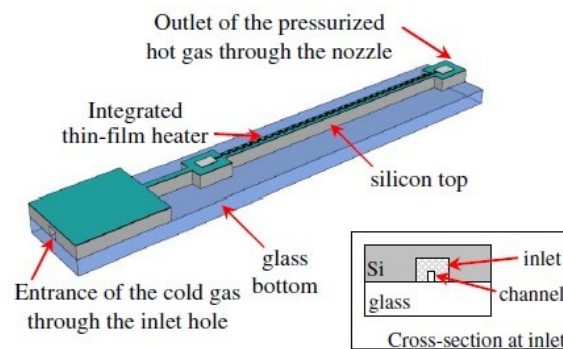
Figure 2.13: MEMS resistojet sketch
[77]

A second iteration of the MEMS VLM design called Dondersteen can be found in [86] by Poyck. Dondersteen as seen in Figure 2.14 used silicon carbide as a heating element, suspended at the centre of flow channels, to increase heat transfer to the flow and lower the heat loss to surroundings. Instead of single channel, multiple flow channels of various geometries were considered and etched on a silicon wafer.

The third VLM design was presented by Silva [92] as seen in Figure 2.15, consisting of the heater chamber with 5 parallel serpentine shaped microchannels and a convergent-divergent micronozzle. Differently to the suspension heating element at the center of the flow channel design of Poyck, heaters were placed external to the microchannel at the bottom silicon wafer. The VLM used an external molybdenum heater (2 types of heater) and microchannels (designs of channel included, large and small diamond pillars, and large and small serpentine pillars) made on a silicon wafer. The wafer was bonded with glass to observe flow behavior inside the thrusters. The channels and heater chamber had a modular design, with each module able to generate 1 W of heater power. Figure 2.15 shows a thruster fabricated on the wafer. An interface was made with Teflon and Aluminium to provide electrical as well as fluid connections, as shown in Figure 2.16.

In TU Delft, the new (fourth) generation of VLM has been proposed by Singh [95] shown in Figure 2.17. This design is based on the most recent (third) VLM design of Silva. This new VLM uses similar serpentine-shaped microchannels and the convergent-divergent micronozzle (bell-shaped and aerospike are also present). However, a new inlet design as shown in Figure 2.17 is proposed where instead of a hole etched normal to the flow direction, an interconnect aligning with the microchannel inlet is used.
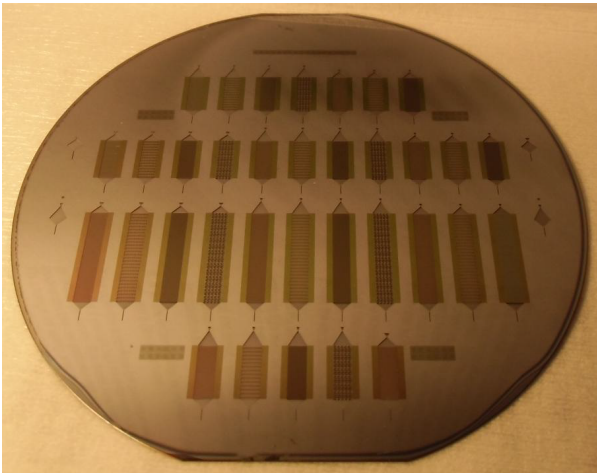
Figure 2.14: Test Dondersteen microthrusters on a silicon wafer
[86]
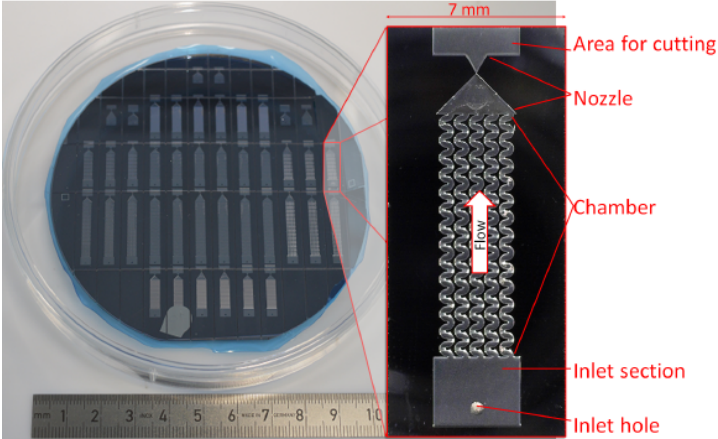
Figure 2.15: A wafer and one VLM from wafer zoomed in by Silva [92]
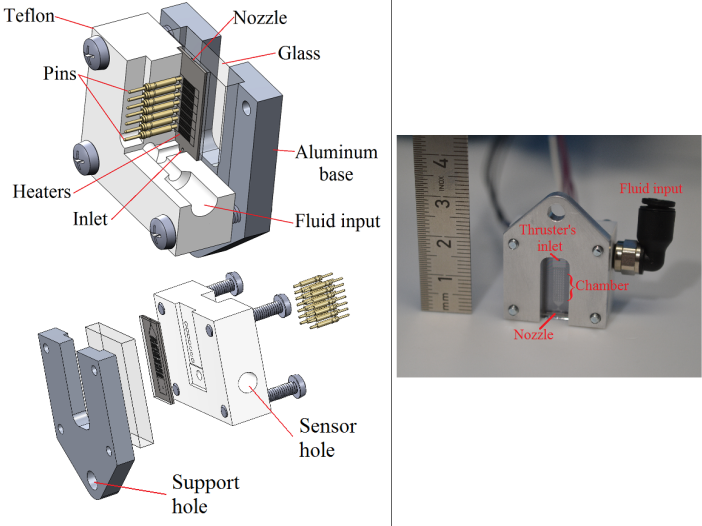
Figure 2.16: Thruster interface 3-D schematic and the interface photo
[92]
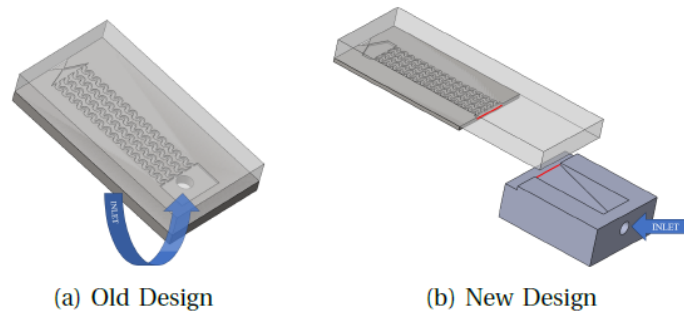
Figure 2.17: a) Old inlet design of Silva with propellant inlet hole, b) VLM design by Singh [95] consisting of axial flow inlet

2.3. VLM characterization methods

In between the development of the three generations of VLM, several researches were done to predict the performances and behavior of the VLM to improve the design and manufacturing processes for the next design iteration. The new features and improvements implemented in the design and development of the new generation of VLM were a result of many researchers' prior work on the investigation and characterization of different aspects of VLM design. Regarding the MEMS VLM system, characterization refers to the process of describing the properties and behavior of the system or device. There are three main aspects of MEMS VLM characterization: performance/operational, geometrical/mechanical, and electrical [94]. The characteristics of VLM can be measured with experiments (empirical relations), derived/observed from experiments (semi-empirical relations), or predicted by models (analytical, numerical).

Van Wees [104] had worked on characterizing the VLM design of Poyck using analytical and experimental methods. Makhan [71] had used an experimental method to characterize the performance of VLM design by Silva. Similarly, Kurmanbay [55] had worked on improving the heater chamber performance based on the design of Silva followed by an experiment for electrical characterization. Design of Silva was investigated by Ganani [36], focusing on the viscous losses of micronozzle at low Reynolds operation and comparing a linear and alternative aerospike nozzle geometry in terms of performance. Recently, Pappadimitriou [83] had analytically and experimentally characterized the performance of VLM based on the design of Silva.

Similarly, a more detailed analysis of fluid flow behavior for Poyck design was performed by Hanselaar in [40]. Hanselaar had adopted a numerical approach to model the fluid mechanics in VLM microchannels. Weinmiller [106] had used a lattice Boltzmann method (LBM) to simulate the fluid dynamics of VLM. Bianchi [14] had used the CFD modeling approach to assess flow boiling in microscale channels.

Outside of TU Delft likewise exists substantial research in the characterization of MEMS VLM. In 2001, Ye et al. [114] suggested a MEMS technology-based VLM design consisting of a micro-resistor, a vaporizing chamber, a nozzle, an inlet, and a microchannel. The microthruster chip was made up of two silicon wafers bonded together with an internal heating element. The VLM was tested with a water propellant, measuring maximum thrust of 2.9 μN with pulse power of 30 W.

Accordingly, Maurya, Das, and Lahiri [74] proposed MEMS VLM design fabricated by bonding two silicon wafers. The VLM was experimentally tested with water propellant. Resulted thrust was in the range of 5-120 μN for heater power of 1 W - 2.5 W. They also presented an analytical model for the same design.

The analytical study of Maurya, Das, and Lahiri [73] had been further researched by Bidabadi, Heidari, and Rahbari [15]. An analytical model extension had been presented based on the division of the VLM into three stages: vaporization, heating (temperature of vapor beyond vaporization point), and isentropic flow in the nozzle. The flow characteristics at each stage were derived based on the solution of theoretical equations.

Differently to the above described MEMS VLM, Chen et al. [24] proposed a design that uses solar energy to heat the propellant. The VLM consists of an injecting hole, injector way, heating channel,

and a converging nozzle (ejects subsonic flow). The VLM was manufactured on a silicon substrate and covered by a Pyrex glass. A 3D simulation of the aft section of the VLM (mostly the nozzle part) was performed using commercial CFD software. It assumed that the liquid evaporated completely before reaching the nozzle inlet. Effects of varying channel length and nozzle outlet width (size of the microthruster) along with varying wall temperatures and mass flow rates were simulated to observe their effects on flow characteristics in VLM. Based on the nozzle outlet width, the numerical model was able to predict thrust in the range of 1 to 6 mN. Similarly, the flow behavior was observed by conducting experiments revealing different flow patterns.

Cen and Xu [20] performed tests to characterize a MEMS VLM performance, relating it to the observed flow patterns in the VLM. The VLM was fabricated with MEMS technology by anodically bonding a silicon substrate and Pyrex glass. It was defined by an inlet, nine parallel microchannels, and a converging-diverging nozzle as seen in schematic Figure 2.18.
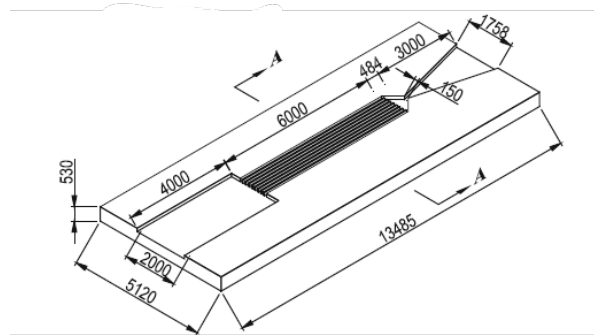
Figure 2.18: Schematic and size of Cen and Xu's MEMS VLM [20]

Kundu, Bhattacharyya, and Das [54] had developed a VLM fabricated by bonding two silicon wafers consisting of an inlet channel, vaporizing chamber, and converging-diverging nozzle, defined by its two external microheaters embedded on the top and bottom surfaces of the VLM device. Thrust of 1.06 mN and the specific impulse of 86 s were predicted with the CFD analysis. VLM was also tested experimentally using de-ionized water as the propellant. From experiments, the maximum thrust value obtained was 1.014 mN at a flow rate of 2.04 mgs^{-1}, power input of 3.6 W, and throat area of 130 μm x 100 μm. The resulting specific impulse was between 50-105 s.

Apart from silicon material, ceramics were used as an alternative to manufacture VLM by Karthikeyan et al. [50]. The low-temperature co-fired ceramic (LTCC) technology was used to fabricate the VLM on LTCC tape, comprising an inlet, an embedded resistive heater at the bottom, and a converging-diverging nozzle. The test was conducted with water as a propellant to measure thrust, temperature, and pressure in the VLM. The experimental testing measured an average thrust of 33.6–67.7 μN and a specific impulse of 3.4–6.9 s, for a flow rate of 1 mg/s and power variation of 7.1–9.2 W. Likewise, Cheah and Low [22] had designed a MEMS-scaled VLM based on high-temperature co-fired ceramic (HTCC) technology. VLM was fabricated on an HTCC zirconia tape. Through experiments, it was found that less power was required for microheaters deposited on the zirconia structure (low thermal conductivity and lower heat loss) to reach a certain temperature compared to heaters on silicon material. Thrust was measured at a maximum of 633.5 μN at a water flow rate of 1 μls^{-1} and a specific impulse of 31 s.

De Giorgi and Fontanarosa [32] had proposed a one-dimensional analytical model that coupled the boiling flow model of the heater chamber to the real nozzle flow model, as well as a two-dimensional and three-dimensional CFD model to predict the performances of the MEMS VLM. In this study, the VLM design of Cen and Xu [20] was used for analysis. The analytical model was divided into the solution of the two-phase flow in the heating chamber and vapor flow in the nozzle, as seen in Figure 2.19. The flow conditions at the entrance of the micronozzle were thus determined by the heating process model in the chamber. The heat exchange process of the two-phase flow at the inlet and heating cham-

ber was modeled by using relations from literature, particularly from relations of Tibiriçá et al. [101]. The gas flow model in the nozzle was based on the ideal rocket theory equations, taking into account the mass flow and exit velocity losses caused by the viscous boundary layer effects.
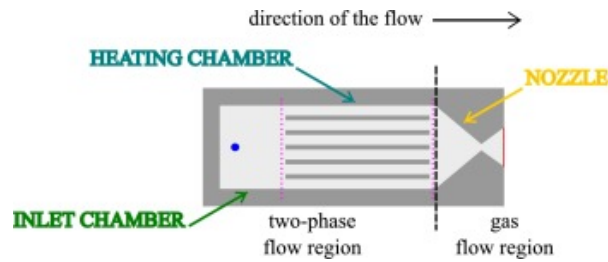
Figure 2.19: Flow phase division in the VLM by De Giorgi and Fontanarosa [32]

Throughout the study, a numerical tool predicting the performance of the VLM heater chamber coupled with a micronozzle was not found that was both more accurate than the analytical model and less resource-intensive (cost and facilities) than experiments. A similar trend was found in research performed outside of TU Delft, with studies focused on either a detailed flow study in microchannels or numerical simulation of micronozzles ([24], [54], [32]) that performed mostly analytic/experimental studies of VLM performance ([114], [73], [15], [24], [20], [54], [50], [22], [32]). Moreover, within TU Delft, the experiments or numerical simulations were performed using nitrogen as a propellant rather than water, which in reality is used to operate the VLM. Bianchi [14] had attempted to replicate experimental results of Yin and Jia [116] exhibiting characteristics similar to those observed in VLM microchannel using water. However, the specific geometry of the VLM microchannel was not modeled in the simulation. Thus, an attempt to perform a numerical simulation of the VLM microchannel coupled with a micronozzle to predict the performance of the VLM was found necessary.

2.4. Simulation motivation

The VLM is a single component that is composed of multiple microchannels with heaters beneath and a single micronozzle. Flow is supposed to be heated and vaporized completely in the microchannels before entering the micronozzle and expanding to supersonic velocities. According to the explanation in section 2.3, numerical simulation of complete VLM including the microchannels and micronozzle has not been attempted yet. There are various reasons to this end. In microchannels, water changes phase to vapor when heated. Such a multiphase flow is a complex phenomenon to model, with the heat transfer mechanism in micro-scale channels not completely understood or agreed upon in the literature found, as discussed in section 2.1. In addition, a single microchannel CFD simulation considered in this study involving phase change takes a couple of days to run, if not weeks, with the high-performance computing system available at TU Delft. The 5 microchannels with micro nozzle downstream together, VLM as a whole, would be even more complex to simulate taking into account the time and computing power available for the research. Thus, it was decided to simulate the two components separately and couple the simulation via a single parameter like mass flow or chamber pressure, which could be used to re-iterate the simulation and solutions. Although, in practice, this method was not feasible, as will be elucidated later in the respective parts of the simulation.

<div align="right">

3

</div>

Microchannel simulation

Microchannel flow boiling CFD simulation requires very high computing power combined with longer simulation times (in order of weeks for some simulations depending on mesh domain), so the simulations are run in Ansys Fluent 2024 R1 solver using 32 cores of the DelftBlue supercomputer at TU Delft. Results are extracted through Fluent, Tecplot 360 EX 2023 R1 and python plot library.

3.1. VLM microchannel design

The VLM heater chamber considered in this research comprises 5 parallel serpentine channels and 8 heaters. Microchannels offer a high surface area relative to their volume, allowing them to dissipate heat more efficiently than larger-scale channels.[91] Serpentine microchannels in addition are able to increase fluid mixing and thus enhance the convective heat transfer. The fluid mixing is attributed to the presence of counter rotating vortices in the fluid cross-section, which considerably enhances convective heat transfer than the pressure drop losses associated with curved serpentine microchannels.[1]

Water had been selected as the green propellant in addition to its capacity to provide high specific impulse performance.[92] As water enters through the inlet, it needs to be completely vaporized to gaseous phase before reaching the convergent part of the nozzle. The flow through the channel will thus contain a two-phase flow, including water and water vapor.

The geometry of a single serpentine is shown in Figure 3.1. The channels are etched onto a silicon substrate to a depth of 150 μm. The total width of the chamber is around 3 mm, encompassed by the 5 channels. The serpentine shape requires 14 replications to achieve a total length of around 9 mm, heating the propellant to completely turn into vapor.

The VLM microchannel dimensions stated above are summarized in Table 3.1. The conditions specified for the microchannel in subsection 2.1.1 were implemented in the VLM channels and confirmed to be satisfied, as detailed in Table 3.2. Properties of fluid including σ, ρ_L, ρ_V and μ_L are specified in Table 3.3. Hydraulic diameter and mass flux, are calculated from Equation 3.1 and Equation 3.2 respectively, where, A = cross-sectional area of single microchannel, p = perimeter, $\dot{m}$ = total mass flow rate, and N = number of channels. The mass flow rate through the microchannels is considered to be the maximum mass flow rate through the nozzle, as derived from ideal rocket theory in section 4.4.

$$d_h = \frac{4A}{p} \tag{3.1}$$

$$G = \frac{\dot{m}}{NA} \tag{3.2}$$
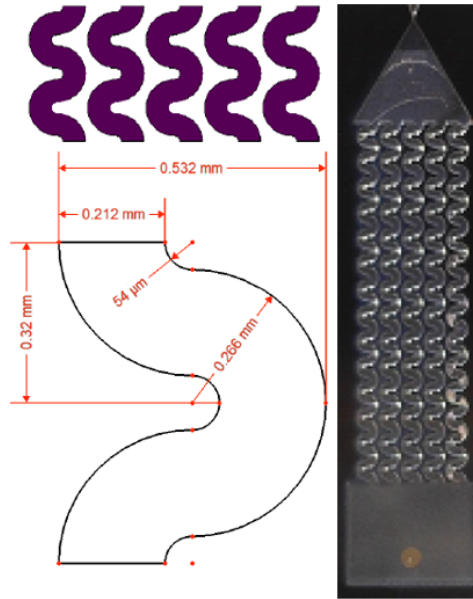
Figure 3.1: Single serpentine dimension (left) and 3rd generation thruster with serpentine channel design (right) [92]

Table 3.1: VLM microchannel dimensions

Dimensions	Values
Length [mm]	8.96
Width [mm]	0.212
Depth [mm]	0.15
Cross-sectional area (A) [mm^2]	0.0318
200 µm ≥ d_h >10 µm	175.6906

Table 3.2: VLM microchannel flow non-dimensional numbers

Bo<0.05	Co>0.5	Ga<160
0.004922	14.2534	0.3020

3.2. Governing equations

Multiphase flow refers to multiple phases of liquid, solid, or gas simultaneously existing together. It can be divided into four main groups: gas-liquid/liquid-liquid, gas-solid, liquid-solid and three-phase flows. These multiphase flow regimes can be further subdivided into separated, mixed, or dispersed flows. Followed by the description in section 2.1, annular flow in the channel with vapor core in the middle and liquid film at the walls is a separated flow. Similarly, droplets, particles, or bubbles immersed in a continuous phase are defined as dispersed flows. A mixture of dispersed and separated flows is also present, for instance, during transitions between flow regimes in a boiling flow channel.

There are two modeling approaches to multiphase flows. Euler-Euler and Euler-Lagrange approach. The Euler-Euler approach treats all phases as a continuum, whereas the Euler-Lagrange approach is based on single-particle tracking or following. Within the Euler-Euler framework, the Volume of Fluid (VOF) is used to model the microchannel flow boiling suitable in this study.

In a VOF model, the governing Navier Stokes equations are solved for immiscible and non-interpenetrating continuous phases. The continuity equation in Equation 3.3 [7] is solved for the volume fraction of a single secondary phase, which in this case is liquid water. It also determines the advection of the interface in the computational domain. An explicit VOF formulation is used, where the volume fraction transport equation is non-iteratively solved once per time step in a transient simulation. In Equation 3.3, α_q = volume fraction, ρ_q = density and $\vec{u}_q$ = velocity vector for phase q. S_M represents the mass transfer between the two phases. Volume fraction for the other (primary) phase (water vapor)

is obtained from Equation 3.4.

$$\frac{\partial(\alpha_q \rho_q)}{\partial t} + \nabla.(\alpha_q \rho_q \vec{u}_q) = S_M \tag{3.3}$$

$$\sum_{q=1}^{n} \alpha_q = 1 \tag{3.4}$$

Similarly, the momentum equation is given in Equation 3.5 [7] based on the volume fraction averaged density ρ in Equation 3.6 and dynamic viscosity μ in Equation 3.7 of the phases indicated with l=liquid and v=vapor. Here, $\vec{g}$ = acceleration due to gravity, p=pressure and $\vec{F}$= external forces.

$$\frac{\partial(\rho \vec{u})}{\partial t} + \nabla.(\rho \vec{u} \vec{u}) = -\nabla p + \nabla.[\mu(\nabla \vec{u} + \nabla \vec{u}^T)] + \rho \vec{g} + \vec{F} \tag{3.5}$$

$$\rho = \alpha_l \rho_l + \alpha_v \rho_v \tag{3.6}$$

$$\mu = \alpha_l \mu_l + \alpha_v \mu_v \tag{3.7}$$

The energy equation in the VOF model is represented by Equation 3.8 [7], where S_E denotes the energy source term, k_{eff} is effective thermal conductivity given by Equation 3.9 and E and T are mass averaged energy and temperature calculated as Equation 3.10.

$$\frac{\partial(\rho E)}{\partial t} + \nabla.(\vec{u}(\rho E + p)) = \nabla.(k_{eff} \nabla T) + S_E \tag{3.8}$$

$$k_{eff} = \alpha_l k_l + \alpha_v k_v \tag{3.9}$$

$$E = \frac{\alpha_l \rho_l E_l + \alpha_v \rho_v E_v}{\alpha_l \rho_l + \alpha_v \rho_v} \tag{3.10}$$

3.3. Numerical setup

In this section, the models used in the microchannel two-phase flow boiling are explained.

3.3.1. Surface tension model

In Fluent VOF model, surface tension forces are added as a source term to the momentum equation represented in Equation 3.11 based on the continuum surface force (CSF) method of Brackbill, Kothe, and Zemach [17] where, σ = constant surface tension coefficient, k = curvature of the interface, δ = Dirac function and $\hat{n}$ = unit normal vector to the interface. The curvature of the interface is defined by the divergence of the unit normal vector to the interface in Equation 3.12 and the unit normal vector is calculated from the gradient of volume fraction in Equation 3.13. A positive divergence denotes an outward curved interface (convex shape). The Dirac function is conditional, where the force is applied only to the interface between the two fluids/phases. The interface is described by the volume fraction of the fluid "n" with α_n = 1 representing the cell filled with phase "n", α_n = 0 means the cell is filled with another phase, and $0 < \alpha < 0$ indicating the presence of interface in the cell.

$$F_{CSF} = \sigma k \delta \hat{n} \tag{3.11}$$

$$k = \nabla.\hat{n} \tag{3.12}$$

$$\hat{n} = \frac{\nabla \alpha}{|\nabla \alpha|} \tag{3.13}$$

Near the wall boundary, the surface normal is adapted through the estimated contact angle θ between the gas-liquid interface and the wall with Equation 3.14, where, $\hat{n}_w$ and $\hat{t}_w$ are wall unit normal and tangential vectors respectively. Subsequently, the local curvature of the surface is adjusted to calculate the surface tension forces.

$$\hat{n} = \hat{n}_w cos\theta + \hat{t}_w sin\theta \tag{3.14}$$

3.3.2. Evaporation and condensation model

For the volumetric mass source term in the continuity equation, the Lee evaporation-condensation model [62] is implemented in the fluent, often found to be used in literature. The Lee model is described by mass transfers from liquid to vapor and vapor to liquid in Equation 3.15 and Equation 3.16 respectively, depending on the interfacial cell and saturation temperature. λ_e and λ_c are model constants known as time relaxation parameters with unit s^{-1}. Values of the parameter need tuning according to the problem, phase change process, flow rate, mesh size, etc., and are experimental. The literature reports a diverse range of relaxation parameters, spanning from 0.1 to 10^7 s^{-1}.[68] In this study, two pairs of relaxation parameters are applied. First implies an equal value of λ_e = λ_c = 1 s^{-1} as was done in [14] and second consists of reducing λ_e and increasing λ_c by 10.

$$\dot{m}_{l \rightarrow v} = \lambda_e \alpha_l \rho_l \frac{T_l - T_{sat}}{T_{sat}} \tag{3.15}$$

$$\dot{m}_{l \rightarrow v} = \lambda_c \alpha_v \rho_v \frac{T_v - T_{sat}}{T_{sat}} \tag{3.16}$$

The energy source term is calculated from the mass source term and latent heat h_{fg} as Equation 3.17.

$$S_E = S_M.h_{fg} \tag{3.17}$$

3.3.3. Thermophysical properties

Most of the flow boiling CFD models in the literature are found to use constant properties of water and water vapor, independent of pressure and temperature. Additionally, Fluent comes with data for real gas properties, which can be accessed through codes provided in Appendix A. RGP tables contain thermodynamic properties of materials as a function of saturation temperature and pressure in table format for a chosen range of temperature and pressure. In the present study, both the constant and the real water properties were experimented with. Results are presented for both types of simulation, and differences observed are explained in the respective sections. Constant properties of water and water vapor taken at the saturation temperature and operating pressure of 1 atm are tabulated in Table 3.3, obtained from NIST [63].

Table 3.3: Thermodynamic properties of water and water vapor used in the microchannel two phase flow simulation

Properties	water	water vapour
Saturation temperature T_{sat} [K]	373.120	373.120
Density ρ [kg/m^3]	958.370	0.598
Specific heat C_p [J/kg K]	4215.600	2079.900
Thermal Conductivity k [W/ m K]	0.677	0.025
Dynamic viscosity μ [Pa.s] / [kg/m s]	2.82E-04	1.22E-05
Latent heat of vaporization h_{fg} [kJ/kg]	2256.440	

3.3.4. Simulation initialization

In the current model, fluid is considered laminar with a Reynolds number of less than 1000, effects of gravity are considered negligible as explained in subsection 2.1.1, Newtonian fluid is assumed, and both fluid phases are considered incompressible because of relatively low velocity in the microchannels.

Numerical solutions in Fluent are based on the finite volume method (FVM) discretization of the governing Navier-stokes equation. The computational domain in FVM is divided into control volumes, over which the differential conservation equations are integrated, discretized, and algebraic terms are obtained for each cell /control volume. In the cell-centered finite volume method, variables are stored at the centroid of the cells, thus interpolation schemes are used to reconstruct values at cell faces.

For incompressible flow, the solution of the Navier-stokes equations involves a velocity field and pressure field that are coupled with each other. The momentum equation contains a pressure gradient term that needs to be known before solving the equation. The continuity equation is then used to satisfy the velocity field obtained from the momentum equation. A pressure-based solver with a segregated and coupled algorithm is available in Fluent to solve this pressure-velocity coupling. Segregated solvers like Semi Implicit Method for Pressure Linked Equations (SIMPLE) solve the velocity and pressure explicitly step-by-step. First, a guess of the pressure gradient is used to solve for the velocity field, which does not satisfy the continuity equation. The velocity field is corrected using an updated pressure field calculated with a pressure correction equation. This process is iteratively continued until the velocity field satisfies both of the continuity and momentum equations. Coupled solvers on the other hand are said to solve both velocity and pressure fields together in an implicit manner.

For microchannel flow boiling simulations in this study, either SIMPLE or coupled solvers are used as deemed appropriate (regarding time and convergence) for the specific microchannel simulation. Spatial discretization schemes are Green-Gauss cell-based for gradient, PRESTO! for pressure, second-order upwind for density, momentum, and energy, and Geo-Reconstruct for volume fraction. First-order implicit is chosen for time formulation. A non-dimensional Courant-Friedrichs-Lewy (CFL) number that characterizes time step size concerning the mesh size and transport velocity, CF<1 is used, ensuring the simulation stability. An initial time step size of 1e-7—1e-6 s is used with the adaptive time stepping method that adjusts the time step size depending on the CFL constraint.

$$CFL = \Delta t \frac{U}{\Delta x} \tag{3.18}$$

Convergence criteria also included the residuals to drop below 1e-3 for each time step in the transient simulation.

3.4. Validation

The microchannel flow boiling CFD model needed to be assessed against experimental data before applying the model to the VLM microchannel for flow characterization. Most of the literature focuses on the investigation of cooling fluids like refrigerants, while microchannel water boiling is not commonly found. Furthermore, VLM microchannel flow boiling experiment data was not found even if there were few experiments with water taking place. In literature, Yin and Jia microchannel was found to reliably show flow confinement and heat transfer characteristics and process with water as the boiling fluid. Moreover, Bianchi [14] had also attempted to reproduce Yin and Jia's experimental results, including the bubble formation and growth process. Thus, the CFD flow boiling model is tested against the results from Yin and Jia's microchannel experiment in terms of bubble formation and growth as well as the heat transfer performance.

3.4.1. Microchannel

A comparison of the two microchannels is presented in Table 3.4. Particularly noticeable is the high heat flux in VLM microchannel compared to Yin microchannel as VLM microchannel are designed to completely vaporize fluid within the microchannel before it enters the micronozzle downstream. While in heat dissipation devices it is preferable to have liquid layer always present (or dry-out phase is delayed for as long as possible) as vapor has low thermal conductivity and is not able to dissipate as much

heat. Similarly, a higher mass flux is closely linked with better convective heat transfer performance in cooling devices. This means the flow boiling process in the validation simulation of Yin microchannel will not consist of dry-out phase, different to what is predicted for the VLM microchannel. In this case, it is assumed that dry-out occurs faster in VLM microchannel (due to smaller dimension and higher heat flux in VLM microchannel) than in the cooling microchannel of Yin. But until the dry-out phase occurs, heat transfer processes in both VLM microchannel and Yin microchannel can be expected to be comparable. Both microchannels conform to the confinement condition of Co > 0.5, which explains that surface tension forces are more prevalent and gravity effect can be neglected as described in subsection 2.1.1. Reynolds number of the flow at the inlet suggests that both microchannels encounter laminar flows. Other dimensional features of VLM microchannel are relatively smaller compared to the Yin microchannel. Nevertheless, both channels satisfy the microchannel conditions and the flow characteristics are assumed to be similar. The mass flux and heat flux for VLM microchannel is calculated based on the chocked mass flow rate and amount of heat required for water vaporization and temperature increment given in section 4.4 for the chosen VLM operating pressure.

Table 3.4: Microchannel from Yin and Jia [116] experiment and VLM microchannel comparison

	D_h [mm]	Length [mm]	Crosssection [m^2]	Mass flux [kg/m^2 s]	Heat flux [kW/m^2]	Co	Re
Yin	0.667	100.000	5.000E-07	20.000	64.700	3.756	47.338
VLM	0.176	8.960	3.180E-08	6.698	318.974	14.253	4.178

3.4.2. 2D Computational domain

In the beginning, a 3D model was considered, however computational time for a 2D multiphase flow boiling would be near or more than 7 days with even the supercomputer Delftblue.[14] The simulation time for a 3D multiphase model would be even longer and would also add to the complexities of flow boiling. Furthermore, a 2D model of cooling microchannels showed good prediction of heat transfer. [115] Considering the time constraint for MSc research, taking into account the time required to simulate the micronozzle as well, and the good prediction shown by the 2D model, the 3D model was discarded.

In Yin's experiment, water enters through the inlet at temperature $T_{f,in} = 23°$ C = 296.15 K. Water is then heated through three sides of the microchannel that has a rectangular cross-section as shown in Figure 3.2, where T_{tci} = temperature of thermocouples, H_{ch} = channel height, W_{ch} = channel width, q_w = wall heat flux, f = fluid and w = wall. The fourth side is a Pyrex glass plate to observe the flow boiling process. Flow at the inlet of the microchannel is subcooled by $\Delta T_{sub} = 77°$ C, at an inlet pressure of 1 atm.
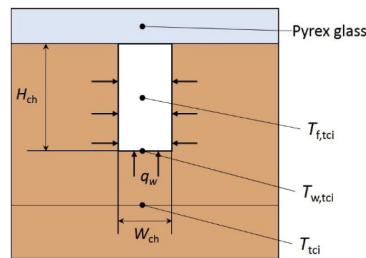
Figure 3.2: Rectangular cross-section of the tested microchannel in [116]

The Yin microchannel is 100 mm in length. In the experiment, 10 thermocouples are placed at an equal distance to measure the data to calculate the heat transfer coefficient. Experimental results of the Yin microchannel present mostly saturated boiling, consisting of slug and annular flow. This is a result of heating the water over time, soon after which most of the microchannel is covered by the slug and annular regime. Over time, a very small section of microchannel towards the entrance remains subcooled with x_e < 0 as seen from the experimental data point in Figure 3.13.

In a 2D approximation of the microchannel flow in the CFD domain, using the full length means a bigger computational domain, higher mesh cell count, and thus the larger computational power plus time in order of weeks. It is aimed in this study to keep the computational time as minimal as possible. The study also aims to reproduce the results of saturated flow boiling in the microchannel presenting

the slug and annular flow regime as observed in the Yin experiment. So the section of the microchannel where saturated boiling is present is taken for the CFD model. This part of the microchannel is taken without losing the Yin experimental heating process, as shown in Figure 3.3. Starting with an inlet subcooled temperature of 296.15 K would mean waiting for the fluid temperature to rise over time, which unnecessarily prolongs the phase change process for the transition to slug flow and annular flow.

A way to prevent waiting for the subcooled flow to heat up over time in the CFD simulation is to take the CFD inlet temperature as the temperature at or near the point in the Yin microchannel where the saturated boiling starts during the experiment. This inlet temperature is estimated based on the length of the microchannel where subcooled flow is present, $L_{sub} \sim 20$ mm given by Equation 3.19, where, G = mass flux, C_{pl} = specific heat of liquid at constant pressure, and $T_{sat,0}$ = saturation temperature at the point where thermodynamic vapor quality x_e = 0 representing the start of the saturated flow.

$$L_{sub} = \frac{GW_{ch}H_{ch}C_{pl}(T_{sat,0} - T_{f,in})}{q_w(W_{ch} + 2H_{ch})} \tag{3.19}$$

So the temperature at the entrance of the CFD domain is taken equal to the temperature at or near the point, where saturated boiling starts in the Yin microchannel experiment, resulting in $T_{inlet,cfd}$ = 369.051 K. For a 2D CFD domain, in Equation 3.20, x denotes the length along the direction of flow, H_{ch} representing the distance between the top and bottom wall in a 2D rectangular microchannel domain, G = 20 kg/m^{2}s and q_w = 323.5 kW/m^2. From the experiment, the value of heat flux q_w = 64.7 kW/m^2 is used in this study.

$$T_{inlet,cfd} = T_{f,in} + \frac{q_w x}{GH_{ch}C_{pl}} \tag{3.20}$$

The heat flux is based on the amount of heat exchanged at all three walls of the microchannel visualized in Figure 3.2. However, in the 2D CFD domain, it has been assumed that the same amount of heat is applied through the heated bottom wall of the microchannel. Heat flux is thus calculated based on the wetted area, $A_w = W_{ch} \times x$ with x representing the simulated section length of the microchannel.

Following the preceding description, the subcooled length is around 20 mm. Taking into account that the flow needs to develop in the microchannel, around 1 mm before the start of saturated boiling point is taken as the inlet of the 2D CFD domain, and the corresponding temperature is used. The simulation domain chosen consists of a two-dimensional rectangular microchannel measuring 30 mm in length, with the bottom surface subjected to a uniform heat flux. The length is chosen to represent the Yin microchannel saturated flow boiling and taking into account the domain covers over half the length of the experimented length. Such that enough data points can be obtained to plot the heat transfer coefficient data as observed in Figure 3.13. In the CFD model, there will be backflow at the outlet. It is allowed in the model but is not physical and does not happen in the Yin microchannel section that is taken as the domain. So the region near the outlet of the CFD domain is not representative, and it is not taken as a data point for the results of the heat transfer coefficient.
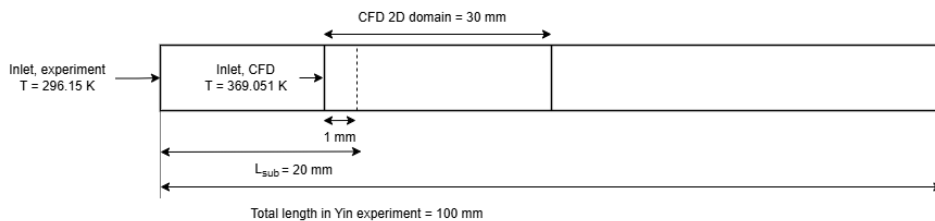

Figure 3.3: 2D CFD domain for Yin microchannel simulation (dimensions are not to scale)

Boundary conditions
The boundary conditions are imposed at the microchannel computational domain's inlet, outlet, and walls. At the inlet, the velocity profile obtained through a single-liquid phase simulation of the microchannel flow is assigned. Flow temperature at the inlet is T_{inlet} = 369.051 K. The experiment was conducted at atmospheric pressure, as such the outlet static pressure of 1 atm is specified. Backflow at the outlet is allowed, where the liquid volume fraction is taken from the neighboring cell, and a saturation temperature of 373.12 K is used. Both walls are stationary and are set with no-slip conditions. A constant heat flux of 323.5 kW/m^2 is provided at the bottom wall. A contact angle of $\theta = 10^\circ$ is chosen from [14]. Flow is initialized with an entire microchannel filled with liquid water, translating to liquid volume fraction = 1 for flow initialization. In the evaporation condensation model, two sets of relaxation parameters are defined. As these parameters are to be tuned, in line with results obtained by Bianchi $\lambda_e = \lambda_c = 1$ s^{-1} are used in one case. In another case, $\lambda_e = 0.1$ s^{-1} and $\lambda_c = 10$ s^{-1} is applied. The variations in the obtained results are discussed in the respective sections.

3.4.3. Validation results
Based on the above discussion, three cases can be defined, summarized in Table 3.5. Results for all three cases mentioned are detailed below, focusing on bubble formation, bubble growth dynamics, and heat transfer performance.

Table 3.5: Yin microchannel cases simulated for validation

Yin microchannel	Dimension	Relaxation parameter	Fluid properties
Case 1	Width = 1 mm	$\lambda_e = 0.1$ s^{-1} $\lambda_c = 10$ s^{-1}	Constant
Case 2	Width = D_h = 0.667 mm	$\lambda_e = 0.1$ s^{-1} $\lambda_c = 10$ s^{-1}	Real
Case 3	Width = D_h = 0.667 mm	$\lambda_e = \lambda_c = 1$ s^{-1}	Real

In case 1, the 2D rectangular domain consists of the top and bottom walls separated by the height (H_{ch} = 1 mm in Figure 3.2) of the microchannel in the Yin experiment. Figure 3.4 presents a part of the 2D mesh containing 196,964 elements with a uniform cell size of 12.5 μ m. All the meshes are made in ICEM CFD. Although a cell refinement study is desired, due to the amount of time spanning more than a week for a single flow boiling simulation, the cell size has been determined from values used in the literature. [14] [43]. At the beginning of the research, case 1 was simulated with constant properties of water and water vapor, width = 1 mm, and initial time step size $\sim$ 1e-07 s (10 times smaller than the time step size used for cases 2 and 3). At the time, case 1 did not show any confinement effects. Multiple reasons were hypothesized at the time. The reason could have been the very small time step chosen for accuracy, as even after more than around 10 days, bubble confinement could not be seen. Another suspicion was the use of the height (instead of the smaller hydraulic diameter) of the microchannel = 1 mm to separate the top and bottom walls of the 2d rectangular domain. This greatly increases the mesh domain and corresponding computation time. The third suspected reason was that the properties of water were not accurate enough to capture the details of the bubble formation and growth. Thus, this led to cases 2 and 3 where, instead, the much smaller hydraulic diameter = 0.667 mm was decided to be used. A higher initial time step size was chosen taking into account that CFL<1. To accurately capture the bubble formation process, a more accurate RGP table was used for the properties of water and water vapor, which uses the properties of the fluid at the corresponding pressure and saturation temperature.
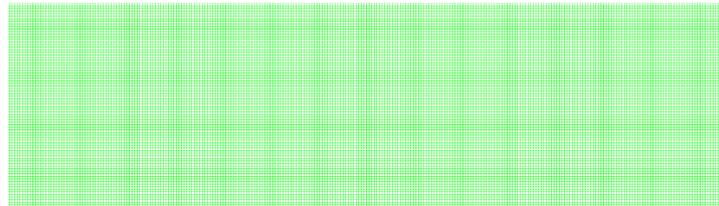
Figure 3.4: A section of 1 mm x 30 mm 2D mesh for case 1 of the Yin microchannel CFD flow boiling simulation

Consequently, in cases 2 and 3 the hydraulic diameter of the microchannel was utilized to separate

the top and bottom walls of the 2D microchannel. The corresponding mesh is a 0.667 mm x 30 mm domain with 132,051 elements with the same cell size as used for case 1. A part of the mesh is shown in Figure 3.5. RGP tables were used for the properties of water and water vapor. Two pairs of relaxation parameters were tested and initial time step size ∼ 1e-6 was used.
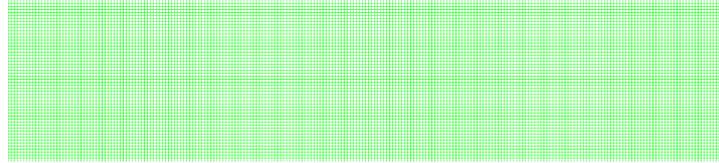
Figure 3.5: A section of 0.667 mm x 30 mm 2D mesh for case 2 and 3 of the Yin microchannel CFD flow boiling simulation

Not enough time was available to test all the parameters that were considered to affect the simulation time and bubble confinement process, but additional conditions were tested towards the end of the research with the remaining time. The first additional condition included 2D microchannel domain width = 1 mm, real properties of water, initial time step size in the order of 1e-06 s and λ_e = 0.1 s^{-1} λ_c = 10 s^{-1}. Second one included the same scenario with $\lambda_e = \lambda_c$ = 1 s^{-1} . It was observed that the flow phenomenon did not exhibit any confinement effects. Rather large chunks of deformed bubbles could be observed (like a churn flow) that began to transition into a wispy annular type regime. It was assumed that the 2D microchannel domain width in these conditions was not small enough for the confinement of the bubble seen in the microchannel.

Similarly, a third additional case of microchannel width = 1 mm, constant properties of water, $\lambda_e = \lambda_c$ = 1 s^{-1} with initial time step size ∼ 1e-06 was tested. It could not be completed as it took around 10 days for even the bubble to nucleate at the bottom wall and rise. This shows that the larger mesh size increases the computation load and time required.

Flow Visualization

Yin and Jia's microchannel experiment presented the record of the bubble growth process for the heat flux of 64.7 kW/m^2 with degree of subcooling $\Delta T_{sub} = 77^{\circ}$ C. Figure 3.6 shows the process where the bubble is nucleated at the heated surface, grows in size and is ultimately confined by the walls, changing the shape from somewhat spherical to an elongated bubble. This is because the bubble is allowed to grow in the flow direction and is confined in the width direction, characteristic of a microchannel effect.
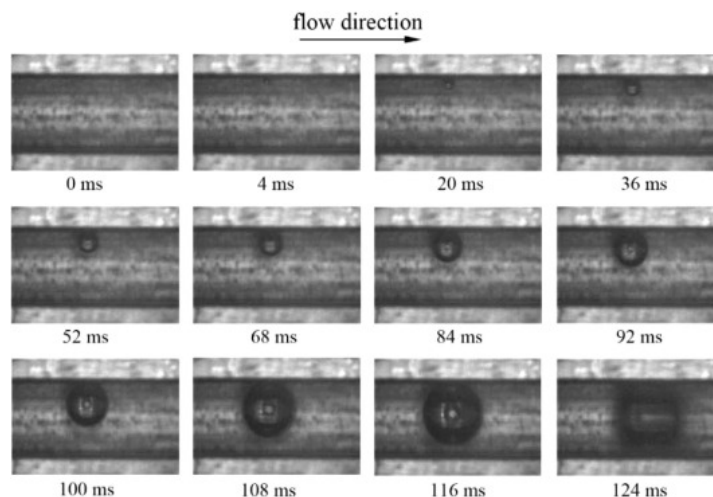
Figure 3.6: Yin and Jia's microchannel bubble growth process observed during the experiment

The experiment also confirms the presence of a thin liquid layer at the wall, throughout the flow regime transition from bubbly, slug to annular flow in the microchannel. Shown in Figure 3.7 is a thin liquid layer in microchannel elongated bubble flow.
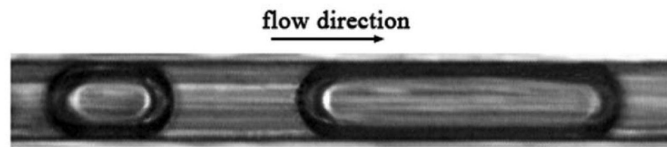
Figure 3.7: Thin liquid film around the elongated bubble [116]

The simulation results of the three cases presented in Table 3.5 will thus be compared against the flow pattern observed in Yin and Jia's microchannel. Below flow boiling in the microchannel is represented by blue liquid regions and red vapor bubble regions defined by the vapor volume fraction of 1 for vapor bubble and 0 for liquid, extracted from the simulation results. Flow in the microchannel is shown in sections of length, as the view of the whole simulated length of the microchannel does not show bubbles in detail. The zoomed-in view of the sections is shown, with flow direction in the microchannel interpreted as entering from the top left and exiting from the bottom right. Sometimes three layers of sections are presented to better illustrate the bubble shape/bubble agglomeration captured in the microchannel length. The region near the outlet is not included as it does not represent the flow observed in the Yin microchannel experiment as previously explained.

Case 1

As explained in the beginning, case 1 is presented for completeness, since the flow confinement effect of the microchannel could not be observed in this case. This case was run for around 158 ms, but nucleation of the bubble in the bottom heated channel only started at around 32.66 ms. The nucleating bubble grew and detached, floating away from the heated surface. The bubble then amalgamated with other bubbles, which expanded the size of the bubble. However, the bubble couldn't grow to the size of the microchannel cross-section. Instead, bubbles slid along the top and bottom wall periodically over time, bouncing off the walls. It was suspected that the higher value of the condensation parameter used could have hindered the growth of bubbles, with the bubble condensing more often as it floated away from the heated surface towards the cooler bulk flow. However, as explained previously under additional tests using the same model with equal relaxation parameters of 1 s^{-1}, the bubbles still could not grow large enough for the same time considered. So the microchannel width was suspected to not be small enough, to enforce confinement to the bubbles in the 2D domain, or the simulation needed to run for longer periods due to the large mesh domain size, which was not possible in this research.
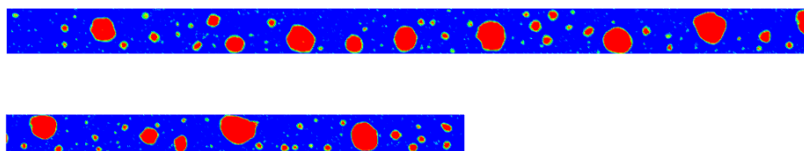
Figure 3.8: Flow pattern seen at flow time = 158 ms in simulation case 1 with width = 1 and λ_e = 0.1 s^{-1} λ_c = 10 s^{-1}. Two continuous sections of the microchannel are shown in part for easier viewing. Flow enters from the top left inlet and exits from the bottom right.

Case 2

A slug flow pattern characterized by elongated bubbles was observed in the simulation of case 2. The bubble shape and growth are shown for different points of flow time in the simulation in Figure 3.9 and Figure 3.10. Similar to the flow in Yin and Jia's microchannel test, the bubbles nucleated at the surface of the bottom heated wall. The bubbles began to expand in size and once it was big enough, detachment of the bubble occurred. Bubble size grew by coalescing with other bubbles. In this case, the bubble growth was confined by the microchannel walls. An elongated bubble shape took place, with the bubble surrounded by a thin film. The liquid layer is present all through the slug flow regime. Also seen are small bubbles entrained in the liquid slug and the bubbles combining to form an annular flow. The dry-out phenomenon did not occur or was not simulated for the cases.

Case 3

A flow pattern similar to that observed in case 2 is also seen in this scenario, although equal relaxation

Figure 3.9: Flow pattern seen at flow time = 71 ms for case 2 with width = 0.667 mm and λ_e = 0.1 s^{-1} λ_c = 10 s^{-1}. Flow enters from the top left inlet and the flow direction is towards the right.
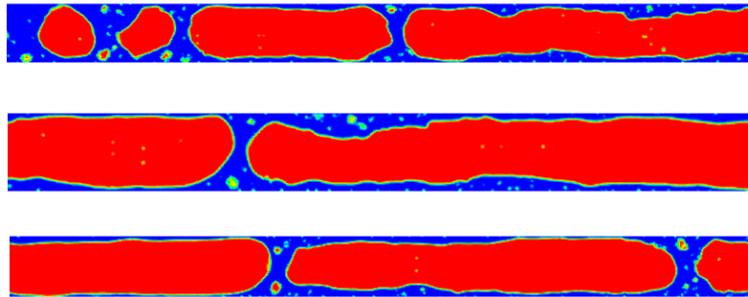
Figure 3.10: Flow pattern seen at flow time = 99 ms for case 2 with width = 0.667 mm and λ_e = 0.1 s^{-1} λ_c = 10 s^{-1}. Flow enters from the top left inlet and flow direction is towards the right.

parameters are applied in this case. The elongated slug flow regime and bubble merging into resultant annular flow are shown in Figure 3.11 and Figure 3.12 respectively. A subtle difference can be observed in terms of the bubble shape in Figure 3.12 compared to case 2 in Figure 3.10 at similar flow times. The liquid flow between the wall and the elongated bubble in case 3 is wavy, while it's more flat in case 2. Similarly, the noses of the elongated bubbles exhibit greater deformation in case 3, deviating further from a thinner rounded shape typical of slug flow bubbles. From this point of view, case 2 represents the Yin microchannel experiment flow much better than case 3. To further emphasize, case 2 uses an evaporation relaxation parameter that is 10 times less and a condensation relaxation parameter of 10 times higher than the value used in case 3. It represents a lower rate of evaporation from the liquid to vapor phase, reducing the bubble's growth rate, and indicating more stable conditions. A faster transition from vapor to liquid phase indicates efficient heat dissipation from the heated walls.
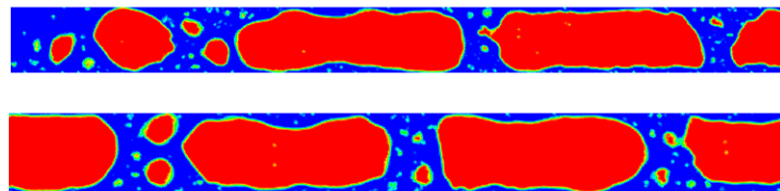
Figure 3.11: Flow pattern seen at flow time = 70 ms for case 3 with width = 0.667 mm and $\lambda_e = \lambda_c$ = 1 s^{-1}. Flow enters from the top left inlet and flow direction is towards the right.

The completely different bubble shapes seen in case 1 could be the result of using a bigger 2D microchannel width separating the top and bottom walls. As explained previously, three additional tests were run for the same computational domain of 1 mm x 30 mm. These tests used different pairs of relaxation parameters, real/constant properties, or higher time step size. In all said setups, the flow
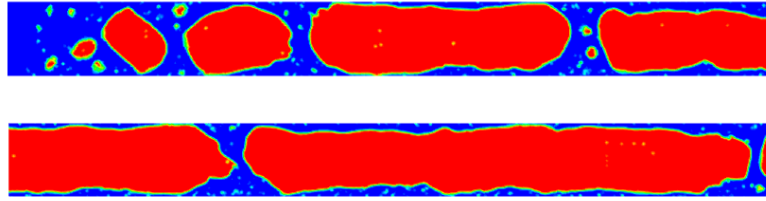
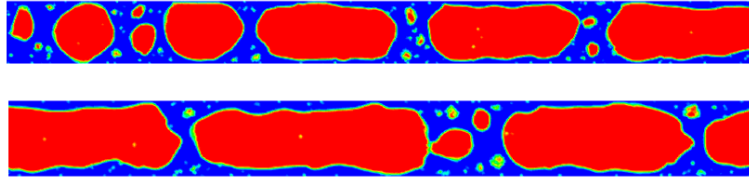**Figure 3.12:** Flow pattern seen at flow time = 97 ms for case 3 with width = 0.667 mm and $\lambda_e = \lambda_c$ = 1 s^{-1}. Flow enters from the top left inlet and flow direction is towards the right.

confinement could not be seen. So this rules out the other parameters and leaves the size of the 2D microchannel domain width as the only parameter that could affect the flow confinement. To some extent, utilizing fluid properties at saturation temperature and pressure from RGP tables could have enhanced the accuracy of bubble formation and growth predictions. However, as the characteristic bubble elongation within the microchannel could not be successfully replicated, its effects could have been outweighed by the effects of the large width of the 2D microchannel domain. This means the 2D width is simply not small enough or does not represent the microchannel dimension for microchannel confinement effects to take place.

Heat transfer characteristic

In [116], the heat transfer performance is measured through the heat transfer coefficient calculated using Equation 3.21, where the temperature of fluid along the direction of flow, $T_{f,x}$, is given by Equation 3.22 for a single wall heated channel in subcooled flow region. For saturated flow regions, the temperature of the fluid is assumed to be equal to the saturation temperature.

$$h_x = \frac{q_w}{T_{w,x} - T_{f,x}} \tag{3.21}$$

$$T_{f,x} = T_{f,in} + \frac{q_w x}{GD_h C_{pl}} \tag{3.22}$$

The heat transfer coefficient was measured by the experiment of Yin for a heat flux condition of 64.7 kW/m^2 and mass flux, G = 20 kg/m^{2}s considered in this study, is shown in Figure 3.13.

Heat transfer coefficient as a function of thermodynamic quality is plotted for the 3 cases simulated and compared with Yin's experimental data. In Figure 3.13, the heat transfer coefficient rises quickly at lower thermodynamic quality due to high heat transfer during phase change from single phase to initial bubbly flow. It reaches a maximum at the thermodynamic quality of around $x_e \sim 0.19$. After which, the heat transfer coefficient decreases along the channel. This corresponds to the flow pattern observed, on which the heat transfer performance is dependent. At the medium thermodynamic quality of $0.1 < x_e < 0.3$, short elongated confined bubbles are said to be observed in the microchannel flow. In this regime, heat is transferred through the phase change and evaporation at the liquid-vapor interface around the elongated bubble also known as the microlayer. Microlayer evaporation has been established as the main heat transfer process in [116]. Since the elongated bubble becomes longer and eventually connects to form the annular flow associated with higher thermodynamic quality, the liquid layer thus depletes along the flow, reducing the evaporative heat transfer rate along the channel. This causes a decrease in heat transfer performance along the microchannel length.

With the presence of a liquid layer, a similar trend in the increase of heat transfer performance with peak value at medium thermodynamic quality and decline afterward is visible in Figure 3.14 and Figure 3.15, for the cases. But case 2 is the closest to the Yin experimental results, with maximum heat transfer performance for Yin $\sim$ 24 kW/m^{2}K and case 2 $\sim$ 23.9 kW/m^{2}K. However, the maximum occurs
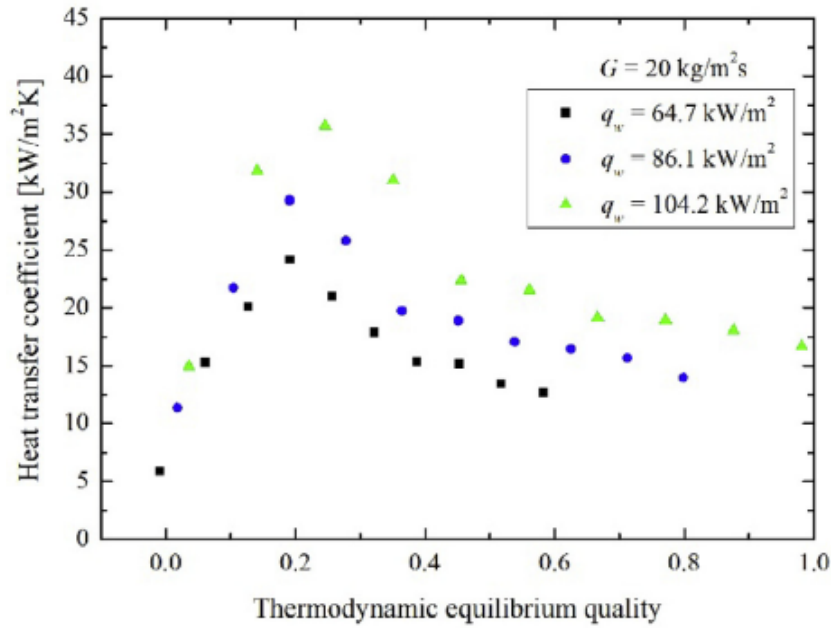
Figure 3.13: Heat transfer coefficient for multiple heat fluxes measured by Yin and Jia's microchannel flow boiling experiment

at a higher thermodynamic vapor quality of $x_e \sim 0.19$ in Yin data, whereas for case 2 $x_e \sim 0.1$. Since the thermodynamic vapor quality range of around 0.1-0.3 has been considered for the short elongated bubble regime where heat performance is at its best, the difference in x_e at which the maximum occurs could be considered negligible. A higher heat transfer performance seen for case 1 is associated with the explained phenomenon of bubbles departing and bouncing off the walls, which increases convection in the fluid as well as the bubble dumping heat away from the walls and condensing in the cooler bulk liquid.
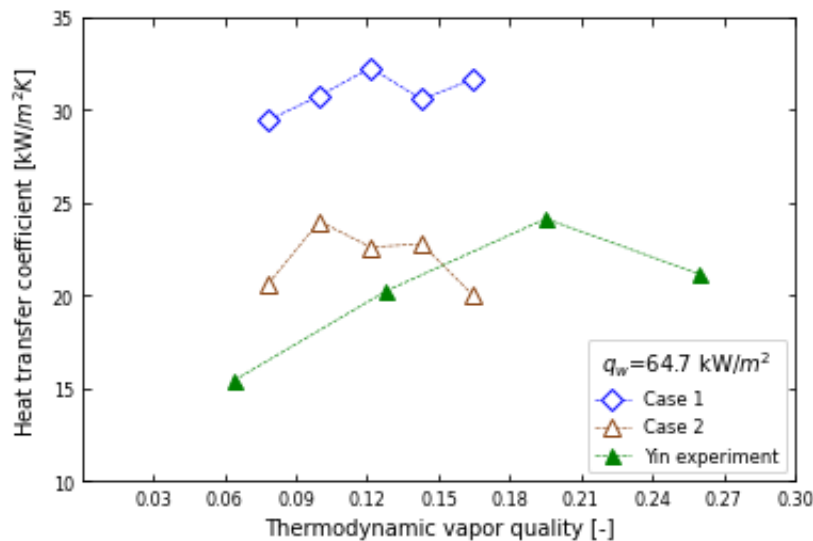
Figure 3.14: Heat transfer coefficient as a function of thermodynamic vapor quality along the heated microchannel surface in case 1 and case 2 compared to Yin microchannel experimental results

This is in line with flow visualization results, where case 2 best represents the flow observed in the Yin microchannel experiment. As seen from the bubbles in the flow visualization above, validation simulation for cases 2 and 3 can reproduce the thin film layer and confined bubbles are present as observed in the Yin microchannel experimental data. Furthermore, the heat transfer coefficient of case
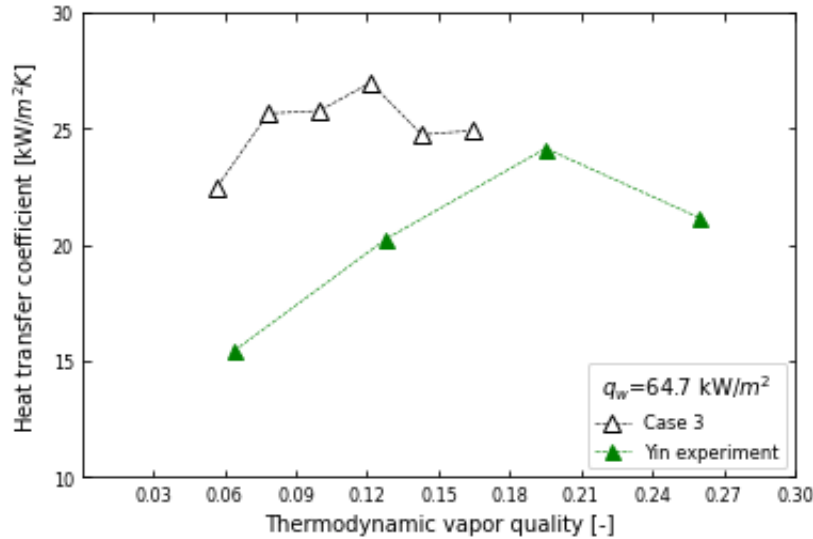
Figure 3.15: Heat transfer coefficient as a function of thermodynamic vapor quality along the heated microchannel surface in case 3 compared to Yin microchannel experimental results

2 closely resembles the peak performance and thermodynamic quality at which the peak occurs (thermodynamic quality at which heat transfer coefficient peaks is not exactly equal) of the Yin microchannel experiment. This leads to partial fulfillment in the validation of the 2D microchannel CFD model. Since there are slight differences regarding values of heat transfer coefficient and thermodynamic qualities as seen plotted in Figure 3.14 and Figure 3.15, a complete fulfillment can not be confirmed. Such slight differences are assumed to arise as the CFD model is an approximation of the 3D microchannel experiment.

3.5. Numerical results

This section describes results from VLM microchannel simulation based on the CFD model discussed in the preceding sections. The computational domain and boundary conditions applied in the model are explained, and the flow characteristics of the VLM microchannel are presented.

The dimensional and non-dimensional characteristics of the VLM microchannel simulated in this study are described in Table 3.1 and Table 3.2 respectively of section 3.1. According to this, the 2D domain is specified as a rectangular section measuring 0.15 mm x 8.96 mm. A mesh with a uniform cell size of 3.75 μm was constructed. The mesh contains 100,422 elements in total. This cell size is based on the number of elements of the 2D mesh used for the validation study of the Yin microchannel experiment. The number of mesh elements is in the order of 132,051 for the Yin microchannel 2D mesh, much larger than the 2D domain of the VLM microchannel. By maintaining a similar order of mesh elements for the VLM microchannel, a fine enough mesh is ensured. A part of the mesh is shown in Figure 3.16. Water flow is assumed to enter the 2D CFD domain at an inlet temperature of T_{inlet} = 370 K, which is near saturation temperature around the starting point of saturated boiling, as was explained in subsection 3.4.2. In reality, there will be a subcooled section near the entrance, which will not be simulated in the CFD model. However, this will also not affect the calculation, as the CFD model is simply simulating the saturated boiling of the VLM microchannel taking into account the temperature that water achieves throughout the subcooled length. Only the bottom wall of the microchannel is heated for this simulation as well, with constant wall heat flux = 318.974 kW/m^2. The rest of the boundary conditions are adopted as explained in subsection 3.4.2.

The 2D domain used for the CFD model of VLM microchannel lies in the x-z plane of the 3D serpentine VLM microchannel shown in Figure 3.17. As explained initially, serpentine microchannels are associated with enhanced convective heat transfer due to flow mixing caused by vortices formed in the cross-section as well as axial flow direction. This is attributed to the centrifugal forces provided by
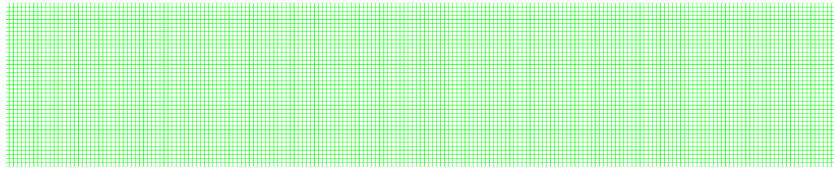
Figure 3.16: 2D Mesh used in the simulation of VLM microchannel flow boiling

the curved feature or periodic bending of serpentine microchannels compared to straight microchannels. [1] In the 2D approximation of the VLM microchannel flow, this additional enhanced heat transfer is not accounted for. In this context, in a serpentine microchannel, improved heat transfer can lead to a more homogenous temperature of the bulk liquid and heated wall, meaning a higher heat transfer coefficient can be predicted, according to Equation 3.21. This would mean the 2D VLM microchannel model would underpredict the heat transfer coefficient. However, an underprediction is better than an overprediction in this regard. Because, for the same heat transfer rate and temperature gradient, a lower heat transfer coefficient would require more heated surface area ($\dot{Q} = hA(T_2 - T_1)$). Overestimating the heat transfer coefficient can result in underestimating the heated surface area required. This miscalculation may leave insufficient surface area for effective boiling, potentially leading to incomplete vaporization of the liquid. Although characteristics like flow velocity and curvature could affect the impact of centrifugal forces compared to the surface tension effects on two-phase flow in serpentine microchannels. Based on this, the centrifugal forces could be deemed negligible or non-negligible. It was not researched in the scope of this thesis, but in general, the underprediction of the heat transfer coefficient seems satisfactory in this framework. Therefore, the 2D CFD model can satisfactorily represent the flow boiling of the VLM microchannel and the resulting heat transfer coefficient will be important to characterize the heat transfer rate and corresponding heating power required.
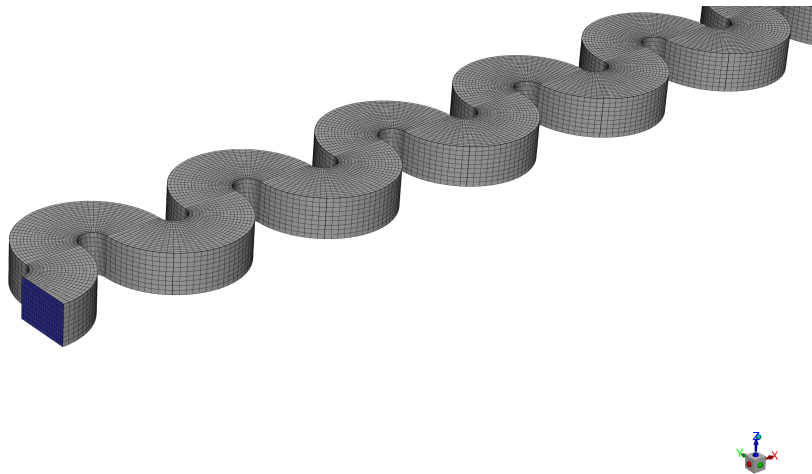
Figure 3.17: 3D Mesh for the serpentine VLM microchannel flow

Aligned with the cases established in subsection 3.4.3, three cases are also defined for the VLM microchannel simulation conditions. These cases are named and differentiating conditions are summarized in Table 3.6. Another VLM microchannel case not mentioned in the table represented by $\lambda_e = \lambda_c =$ 1 s^{-1} and constant water properties was run, but could not be completed within the remaining research time. Regardless, similar flow behaviors observed in case sim 71 are expected, so the fourth case is not considered for the following discussion.

Table 3.6: Three VLM microchannel simulation cases tested in this study

VLM microchannel simulation identifier	Relaxation parameter	Fluid properties
sim 71	$\lambda_e = 0.1$ s^{-1} $\lambda_c = 10$ s^{-1}	Constant
sim 81	$\lambda_e = 0.1$ s^{-1} $\lambda_c = 10$ s^{-1}	Real
sim 82	$\lambda_e = \lambda_c = 1$ s^{-1}	Real

3.5.1. Flow pattern and heat transfer performance

The flow patterns observed are presented in Figure 3.18, Figure 3.20 and Figure 3.21 for sim 81, sim 82, and sim 71 respectively. In Figure 3.18 and Figure 3.20 flow confinement is visible by the characteristic feature of the bubble shape elongated in the axial direction and confined by the width of the microchannel. As explained previously, water entering at a temperature near the saturated temperature of the water is heated by the bottom wall where vapor bubbles are nucleated, depart at a maximum departure diameter, and are grown to the size of the microchannel cross-section. When the confinement effects are taking place, slug bubbles are visible. However, differently from what was encountered in the validation study of Yin's microchannel flow, the elongated bubbles are seen to form a vapor patch at the wall. A zoomed-in view of the observed vapor bubble patch is shown in Figure 3.19. This has been attributed to the intense evaporation at the microlayer formed beneath the vapor-liquid interface to the point of disappearance of the layer. During bubble motion, the dry patch is re-wetted with the cooler liquid flow and the cycle continues.[16]
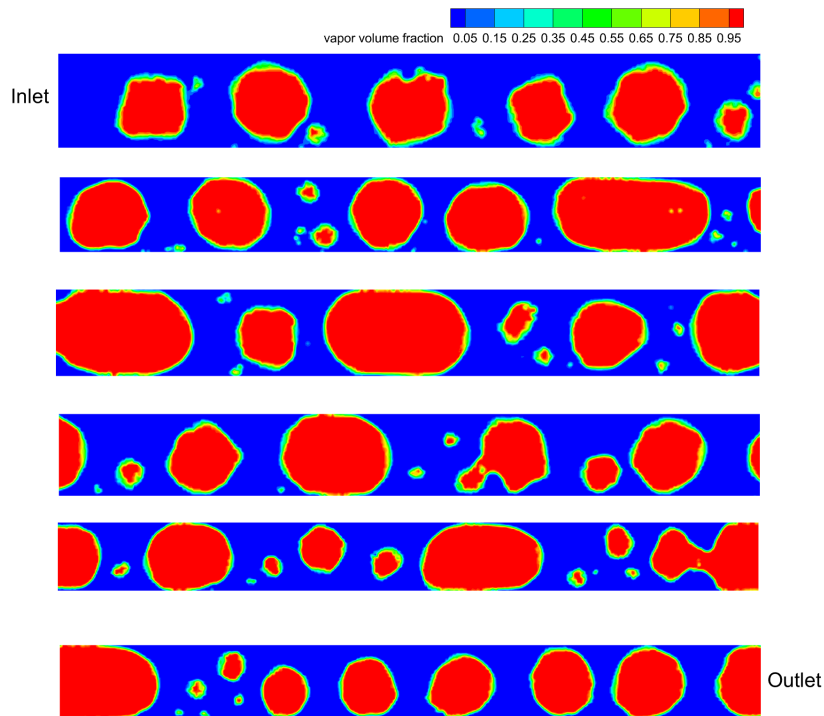
Figure 3.18: Flow pattern observed in VLM microchannel flow boiling simulation sim 81 at flow time = 13 ms

An unexpected phenomenon is the vapor patches formed at the top wall, which was not directly heated in the model. Several reasons can be associated with the vapor patch observed at the top wall. In [34], the liquid layer is said to be thicker at the corners of the 3D square cross-section compared to the uniform thickness of liquid around a circular channel, which in general causes the thinning of the liquid layer in the sides of the bubble. Similarly, surface tension effects in the confined spaces of the microchannel could cause the liquid to deplete at the top and bottom of the bubble interface. At the same time, the bubble motion can also cause uneven liquid distribution, resulting in the disappearance of the liquid at the top of the bubble. A more simplistic reason could be that the heat transfer from the
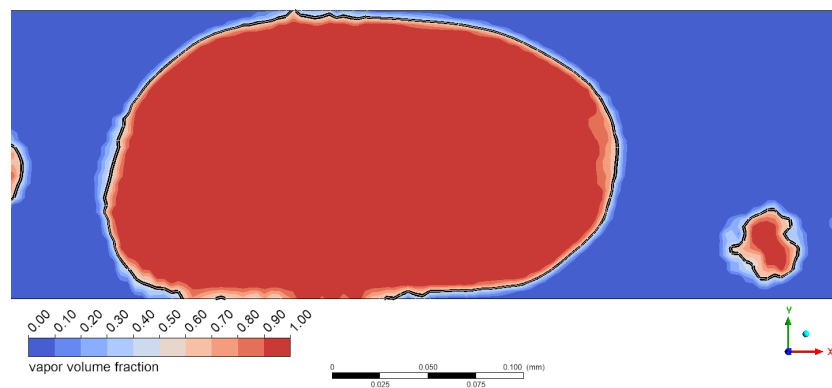
Figure 3.19: Vapor patch formed at the heated wall of the VLM microchannel sim 81. The black line corresponds to a vapor volume fraction of 0.5.

vapor causes the top liquid layer to evaporate at the vapor-liquid interface.

Moreover, the VLM microchannel is fabricated to heat up the fluid until dry out such that no liquid phase enters the micronozzle. Which is why the heat flux is higher than in cooling microchannels. The mass flux used in the VLM microchannel simulation is also relatively lower than Yin's microchannel model. A lower mass flux could lead the flow to dry out with faster evaporation of the liquid. That would mean the flow pattern observed could then be characteristic of the VLM microchannel.

In any case, the vapor patch observed seems to be a temporary attachment to the wall, since it is re-wetted with liquid once the bubble moves along the microchannel. This is evident due to the absence of hot spots that can develop on the wall if prolonged vapor patches are present. The vapor phase cannot remove heat as effectively as the liquid phase, increasing the temperature of the wall instead. The time-averaged wall temperature for all three simulation cases plotted against the thermodynamic vapor quality can be seen in Figure 3.22. The almost constant temperature of the wall maintained along the microchannel length with no sudden spike in temperature indicates that the wall is not extremely heated as would be the case with hot spot formation, and flow is approaching a quasi-steady state. Although for sim 81 there is an increment in the time-averaged wall temperature at the beginning of the microchannel length. This outcome likely resulted from the combination of the very low evaporation constant applied in this particular case and the initially reduced heat removal capacity of the single-phase liquid. Compared to the higher heat removal via latent heat in the two-phase slug flow regime occurring downstream, this leads to a rise in the microchannel wall temperature. Likewise, a higher temperature of the wall is seen in sim 71. As seen in Figure 3.21, no presence of slug flow can be confirmed even after simulating much longer than the other two cases. This result is similar to the results obtained in the validation study of the Yin microchannel flow case 1 under similar conditions. Since slug flow is associated with a higher heat transfer rate via microlayer evaporation, its absence in the microchannel flow of sim 71 means a lower heat transfer performance than the other cases with a slug flow regime present. As a result, heat input raises the wall's temperature in sim 71. This is also evident from the heat transfer coefficient plotted and presented in Figure 3.23.

Heat transfer coefficient, plotted in Figure 3.23, is calculated depending on the time-averaged wall temperature and bulk fluid temperature of the flow. Heat transfer performance of the VLM microchannel in sim 82 best resembles the measurements fit obtained by Yin experiment, as shown in Figure 3.13. According to this, peak heat transfer performance is achieved at the moderate thermodynamic quality of $0.1 < x_e < 0.3$, followed by a decline in the performance due to the thinning of the liquid layer as the bubbles become longer and merge into annular. However, in the VLM microchannel simulations, the annular flow could not be reproduced accurately.

Throughout the simulation, it was evident that CFL<1 ensured that the method was accurate. A
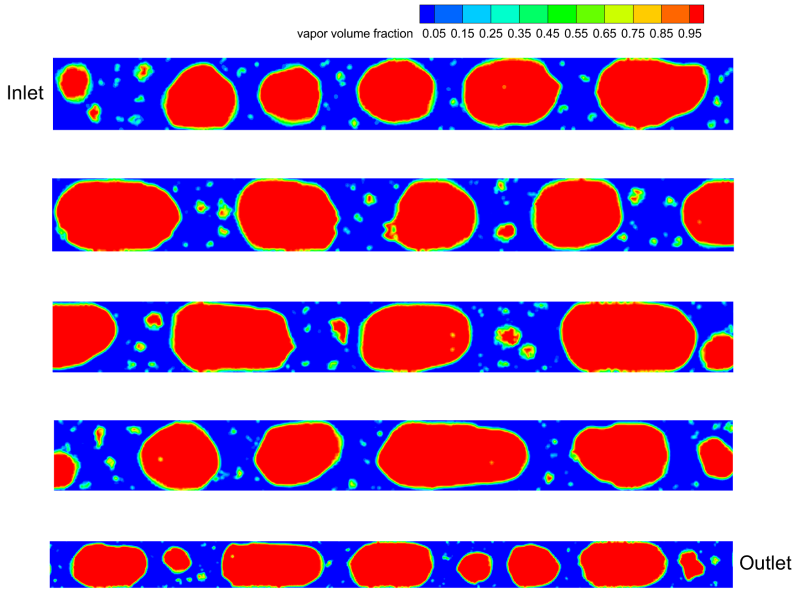
Figure 3.20: Flow pattern observed in VLM microchannel flow boiling simulation sim 82 at flow time = 12 ms.
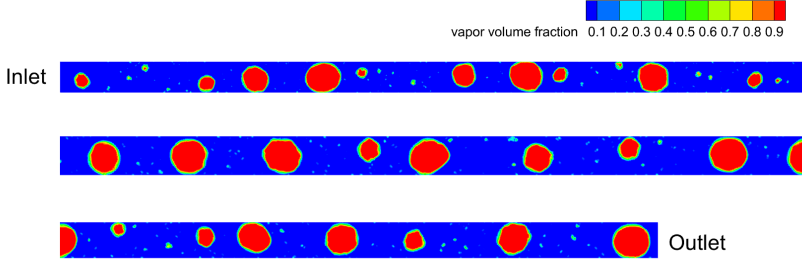
Figure 3.21: Flow pattern observed in VLM microchannel flow boiling simulation sim 71 at flow time = 54 ms.
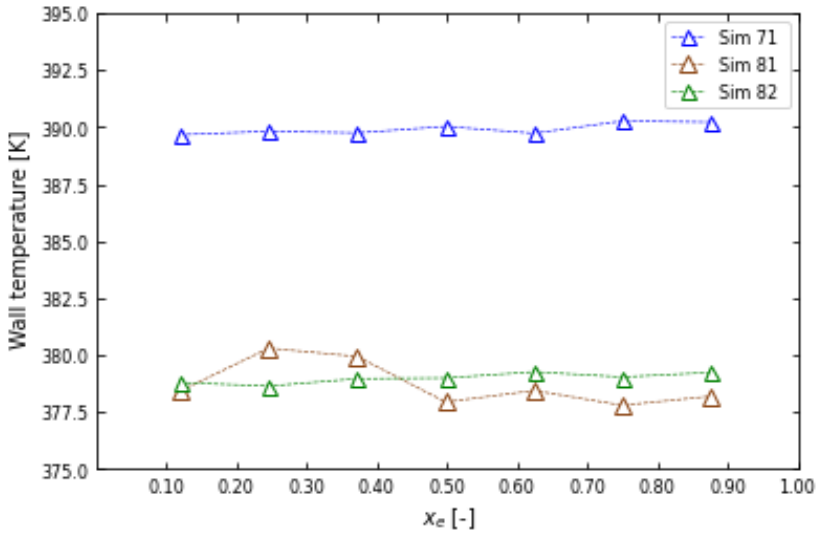
Figure 3.22: Time-averaged wall temperature against thermodynamic vapor quality along VLM microchannel

section of the CFL number field of the solution for sim 82 for instance is shown in Figure 3.24. But as flow started transitioning to a longer elongated bubble the CFL constraint could not be enforced by the solver. This could be the limit of the solver itself, even though different methods including reducing time step size, using fixed time stepping method, using a low CFL value, etc. were tested but failed to improve. Nonetheless, with the results obtained, the VLM microchannel flow heat transfer performance is best represented by conditions of sim 82. For the other conditions, no certain trend is apparent. A brief increase or decrease in heat transfer performance along the microchannel is observed, which could be caused by the bubble motion associated with vapor patch formation and re-wetting along the microchannel.
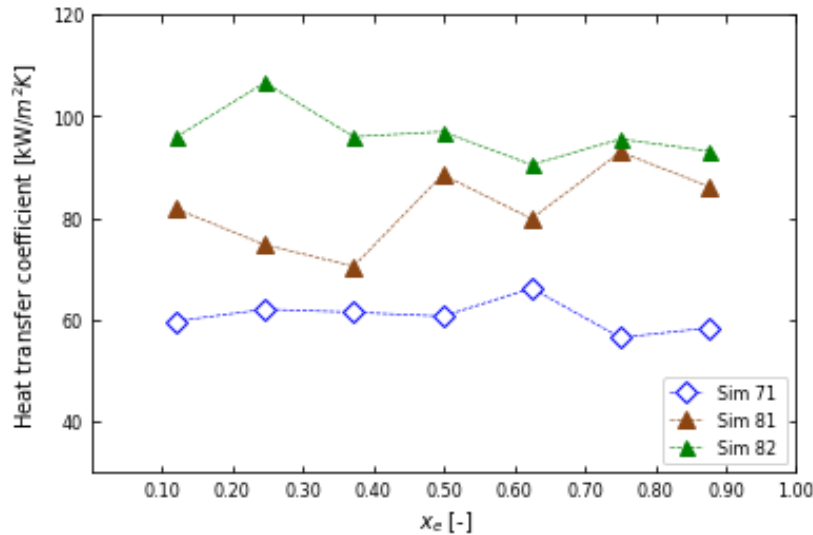
Figure 3.23: Heat transfer coefficient against thermodynamic vapor quality of the VLM microchannel
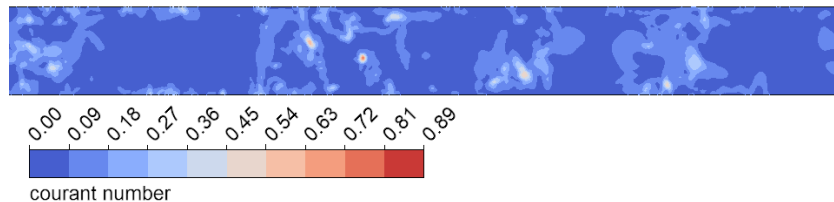
Figure 3.24: Courant number field during the sim 82 VLM microchannel flow boiling simulation

3.6. Concluding remarks

In the preceding section, the CFD modeling approach for the two-phase flow boiling in microchannel was presented. The results of the CFD simulation of the microchannel flow were laid down. The results included validation of the CFD microchannel flow model against experimental data of Yin and Jia [116]. In the study, the numerical results could not completely reproduce the heat transfer performance of Yin's microchannel boiling flow. Although the heat transfer coefficient was quantitatively similar and comparable trend in the performance along the microchannel was observed. Furthermore, the model was able to replicate the thin film layer observed in the Yin microchannel boiling flow.

This was followed by the VLM microchannel flow boiling model results, including flow visualization and heat transfer coefficient along the microchannel surface. From the description above, it is evident that the VLM microchannel flow observed is different from the one seen in the validation study of Yin microchannel flow. Similar heat performance behavior compared to one of Yin microchannel

flow could be demonstrated for a specific condition applied to the VLM microchannel model. But this means the model, especially the evaporation and condensation model, is dependent on the estimated empirical parameter to define the phase change rates. Because of the experimental nature of the relaxation time constants used in the model, it needs to be further analyzed for sensitivity. Apart from the modeling details, the two-phase flow boiling in the microchannel is a generally complex subject that is frequently debated among researchers. Especially the heat transfer mechanism in the microchannel can not yet be conclusively agreed upon, with similar experimental models resulting in different heat transfer performance in microchannels as explained in section 2.1. This meant the CFD model of the VLM microchannel has uncertainties that need to be researched more, but are not in the scope of this study. Overall, VLM microchannel flow results are still useful, as they undeniably present the bubble confinement effects characteristic of microchannel flow. The heat transfer performance of the VLM microchannel is also comparable to experimental data, regardless of the model's dependency on empirical constants.

Moreover, the best representative of VLM microchannel flow boiling was found to be present in the case: sim 82. According to this, the average heat transfer coefficient along the microchannel is 96.351 kW/m^2. The average wall temperature and fluid bulk temperature along the microchannel are 378.998 K and 375.680 K respectively. These are time-averaged values. With this information known, the average heat transfer rate ($\dot{Q} = hA(T_w - T_f)$ as previously mentioned) over the heated surface can be calculated to be 0.607 W for a single microchannel. For the VLM considered in this study containing 5 parallel microchannels the average power input from the heater required is $\sim$ 3.036 W, assuming the heater has no inefficiency. In reality, however, the heaters are inefficient and there will be losses to the environment, demanding more power to compensate for losses. Based on the heat transfer performance along the VLM microchannel predicted by the model, diminished heat transfer can occur in reality during the transition to the annular and dry-out phase, suggesting again a high power loss to the surroundings. It has to be noted that due to the numerical instability of the CFL criteria, the transition into the annular flow and the dry-out phase could not be simulated accurately for VLM microchannel boiling flow. Similarly, until the time flow was simulated in the model, no thermal instabilities/ hotspots were identified that could spike the wall temperature. This means even higher heat flux could be maintained at the heated wall. However, it is to be noted that heat flux was uniformly applied in the model, which will not be completely true during operation. For the supplied heating power and size of the microchannels, a lower mass flow rate is also important to vaporize the liquid water faster. So mass flow rate control should be implemented at the inlet of the real VLM.

3.7. Coupling problem

The coupling problem of the microchannel simulation with that of the micronozzle still remains. It was intended that initially the microchannel would be modeled and simulated in the solver with an inlet boundary condition of mass flow rate obtained from the 1D isentropic flow solution of the micronozzle. After the micronozzle simulation results were obtained, the more accurate 3D mass flow rate would be used to reiterate the microchannel flow simulation until the mass flow rate in the two solutions was matched. In reality, however, the simulation time for the two-phase boiling in the microchannel was too long within the time constraint of this research to even consider re-iteration. During the progression of research, due to the already complex nature of microchannel flow simulation as described above, such an approach seemed invalid. To be noted is that the microchannel flow boiling CFD model results heavily depended on the values of initialization parameters and boundary conditions, meaning slight changes could result in divergence of the solution. This meant the approach to tune the inlet boundary conditions to try to match the mass flow rate with the micronozzle simulation results could not work. With above-explained uncertainties observed in the model, this approach was deemed infeasible and thus the coupling of numerical models could not be achieved. However, plausible results are obtained from the simulations of microchannel and micronozzle as described in the respective chapters.

In the comparison of the microchannel and micronozzle simulations, the 3D micronozzle CFD model very closely resembles the real VLM operation. The micronozzle model was implemented with slip boundary conditions at the micronozzle walls at the chamber pressure of 1 atm and ambient pressure equal to the real VLM operating condition of 30 Pa (near vacuum, in line with the vacuum chamber pressure). The real VLM can be chosen to operate at different ranges of pressure based on the amount

of thrust required. The micronozzle model can simulate a wide range of pressures, as long as very low pressure introducing completely rarefied flow at the divergent section of the micronozzle is prevented. However, the model handles partial rarefaction well enough. Similarly, the micronozzle CFD model was also confirmed to be validated against the experimental performance data of Cen and Xu, which demonstrates deviations within 10% for mass flow, thrust, and specific impulse of the micronozzle.

Comparatively, the 2D microchannel CFD model being 2D already makes it less close to the actual operational conditions of real VLM. 3D effects were not taken into account in the model. The outlet pressure of the 2D microchannel domain was taken at 1 atm pressure, equal to the chamber pressure used in the micronozzle. However, flow reversal was allowed in the microchannel model, which makes the end section of the microchannel simulation inaccurate. The reason heat performance along this section was not used in the results. The inlet conditions used also greatly impact the flow boiling process. In the CFD model, $T_{inlet} \sim 370$ K was taken, which is the temperature near the point in the microchannel where saturated boiling starts. This point is around 1.022 mm from the inlet of the real VLM microchannel length. This does not necessarily affect the heat transfer process but is less representative of the real VLM geometry compared to the micronozzle simulation. So in the 2D CFD model, a fixed section of the microchannel is used rather than the actual geometry. Moreover, the 2D straight rectangular domain is also an approximation of the serpentine microchannel shape, which does not take into account the curvature effects on the fluid mixing and eventual enhanced heat transfer performance. Although, as explained previously, this does not largely affect the approach taken in the CFD two-phase model. Moreover, the CFD model of the microchannel is sensitive to the input variable and heating condition, which greatly determines the flow behaviors and numerical stability of the simulation. This makes the microchannel model applicable at a limited range of boundary conditions, and the implementation of different operating conditions of real VLM does not guarantee accurate solutions. Thus, micronozzle simulation is closer to real VLM operational conditions than the microchannel model.

4

Micronozzle simulation

4.1. VLM micronozzle design

Micronozzle design considered in the numerical study is a linear convergent-divergent micronozzle of the new generation VLM microthrusters manufactured by Singh [95]. A linear micronozzle can be described by the following parameters illustrated in Figure 4.1 and stated in Table 4.1. The values for throat width, convergent half angle, divergent half angle, and area ratio have been obtained from [95]. Throat longitudinal radius and contraction approach radius are chosen from the conventional nozzle values found in [118]. A requirement based on the prior heater chamber's dimension has driven the micronozzle's inlet width. The outlet width can be calculated based on the area ratio, and other parameters can be computed from the given nozzle dimensions.
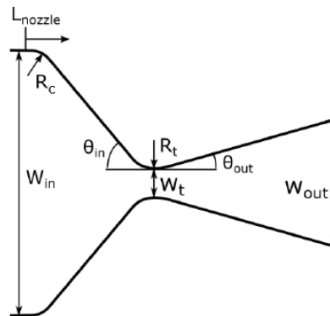
Figure 4.1: Linear convergent-divergent schematic with nozzle definition parameters [36]

Table 4.1: VLM micronozzle parameters

Parameters	Symbol	Values	Unit
Throat width	W_t	50	μm
Nozzle slit height	h_{nozzle}	150	μm
Convergent half angle	θ_{in}	70	deg
Divergent half angle	θ_{out}	60	deg
Throat longitudinal radius	$R_t = W_t/2$	25	μm
Contraction approach radius	$R_c = 0.05 W_{in}$	150	μm
Area ratio	A_e/A_t	20	-
Exit width	W_{out}	1000	μm
Inlet width	W_{in}	3000	μm
Converging part length	L_{con}	554.361	μm
Diverging part length	L_{div}	288.675	μm

4.2. Numerical modelling method

Fluid flow can be modeled either as a continuum, treating the fluid as a continuous medium characterized by macroscopic properties such as density, pressure, temperature, and velocity, or based on molecular models that determine the fluid as a collection of discrete molecules.[35] Continuum flow assumption is relevant in various flow field domains. However, as the size of devices reduces, different flow regimes emerge, and continuum assumptions may no longer remain valid.

The validity of the continuum model can be specified by a dimensionless Knudsen number, which compares the mean free path (λ) to the characteristic length scale of the flow: Kn = $\frac{\lambda}{L}$. The mean free path refers to the mean distance traveled by molecules between collisions. A higher Knudsen number is associated with larger rarefaction effects, where the continuum approach is not accurate. Flow regimes are differentiated based on the Knudsen number with continuum Kn < 0.01, slip 0.01 < Kn < 0.1, transitional 0.1 < Kn < 10 and free molecular Kn > 10.

With their diminished size, flow in micronozzles tends to experience rarefaction, particularly towards the end of the divergent section, changing from continuum flow in the convergent section to transition regime in the divergent and free molecular in the region downstream from the exit of the micronozzle. This demands models that are valid in a wide range of Knudsen numbers. The direct simulated Monte Carlo (DSMC) method is one such model that applies to the full flow regimes. However, this method is extremely expensive on computational as well as time resources. For micronozzle flow operating at very low pressures, continuum flow persists over the convergent section, and rarefaction effects start toward the end of the divergent section. Using DSMC for such simulation, although seems straightforward, is a more computational burden, especially for Knudsen number less than around 0.01. From [103], it is found that for low Kn numbers, the grid, and time step size requirement grows with a reduction in Kn, which implies that resource increases with Knudsen in order of $1/Kn^4$. Even though DSMC is valid for the whole range, using it for continuum regime flow encountered in the micronozzle's convergent part has penalties in computational time and power. An alternative method to numerically study the flow in micronozzles is the CFD method based on Navier-Stokes equations using slip flow conditions that take into account some rarefaction effects until Kn < 0.1 or using higher order slip conditions until Kn < 0.3.[35] [110] Several researchers have simulated micronozzle flow using the DSMC method and/or CFD method.

In [69], Liu et al. had applied both DSMC and continuum method with slip boundary condition to predict the flow field of a 2D micronozzle with a throat width of 30 μm using nitrogen gas. It was stated that both methods provided a good prediction of the flow field in the range of Kn from 0.0088 to 0.026, but due to flow expansion towards the nozzle exit lip, a difference in the results was seen, specifically as local Kn reached 0.045.

Likewise, both DSMC and continuum approaches were used by Alexeenko et al. [3] in the numerical study of micronozzle, where it was found that the two methods were consistent in the micronozzle flow solution. However, it was also noted that more differences were found near the nozzle exit lip as flow expanded.

Torre [103] presents a comparison between the CFD and DSMC methods, as well as a hybrid CFD/DSMC method. According to the numerical study that had been performed for micronozzle with throat Knudsen in the range of 0.008-0.125, strong rarefaction effects were seen for throat Knudsen larger than 0.01. Beyond throat Knudsen of 0.01, the continuum approach was thus deemed inaccurate even with higher-order slip flow models.

Consequently, DSMC is not considered in this study because of its high computational costs (around 100 million computational particles [36]) and lengthy simulation times, requiring weeks to months for single micronozzle simulation. With the relatively accurate prediction capability of the CFD method, this study will use the method with slip flow conditions using the threshold value of Torre to prepare the micronozzle simulation conditions. In the current study, the CFD software Ansys Fluent 2024 R1 is used to simulate the micronozzle flow. All micronozzle flow simulations were performed in Fluent's pressure-based coupled compressible flow solver. The simulation is run on 8 cores AMD Ryzen 7 5700U processor. Later on, to speed up the simulation time, cases were also run with the high

computing power of DelfBlue.

4.3. Governing equations

In CFD simulations, the fluid dynamics is based on the governing equations of continuum fluid flow and heat transfer, presented in Equation 4.1, Equation 4.2 and Equation 4.3. They mathematically represent the three conservation laws, including mass conservation, Newton's second law (F = m a), and the first law of thermodynamics of energy conservation respectively.[105] The equations are stated in the compressible form of a Newtonian fluid, which is relevant in the numerical simulation of this study.

$$\frac{\partial \rho}{\partial t} + \nabla.(\rho \vec{u}) = 0 \tag{4.1}$$

$$\frac{\partial (\rho \vec{u})}{\partial t} + \nabla.(\rho \vec{u} \vec{u}) = -\nabla p + \nabla.\vec{\tau} + \rho g \tag{4.2}$$

$$\frac{\partial (\rho E)}{\partial t} + \nabla.(\rho E \vec{u}) = -\nabla.(k \nabla T + (\vec{\tau}.\vec{u})) \tag{4.3}$$

$$\tau = \mu \left((\nabla \vec{u} + \nabla \vec{u}^T) - \frac{2}{3}(\nabla.\vec{u})I \right) \tag{4.4}$$

$$E = e + \frac{|\vec{u}|^2}{2} \tag{4.5}$$

where, ρ = density, $\vec{u}$ = velocity, p = pressure, k = thermal conductivity, μ = dynamic viscosity, e = specific internal energy, and I = identity tensor.

In Equation 4.1, the first term on the left-hand side denotes the rate of change of mass per unit volume and the second term on the left-hand side is a convective term representing the net flow of mass across fluid element boundaries. Similarly, the time rate of change of momentum/energy terms and convection terms can be identified in the other equations.

The above-governing equations provide 5 equations (1 continuity, 3 momentum, and 1 energy equation) with 6 unknown flow-field variables specifically, ρ, p, u, v, w, and e. To close the system, two equations are needed. Assuming a perfect gas, the first is the equation of state: p = ρRT and the second is a thermodynamic relation: e = C_vT, where, R = specific gas constant and C_v = specific heat at constant volume. [6]

4.4. Theoretical performance

To characterize the thrust and specific impulse performances of a thruster, it requires that mass flow $\dot{m}$, exhaust velocity V_e, and exit pressure p_e are known. These parameters can be estimated using equations provided by the ideal rocket theory. To be specific, the ideal rocket theory provides equations that relate pressure, temperature changes through a nozzle to exhaust velocity. It is based on several assumptions. Some of the most important assumptions made by the ideal rocket theory are gaseous propellant state in the chamber, homogenous gas with constant composition, gases following ideal gas law, calorically perfect gas, steady, one-dimensional, and isentropic nozzle flow, negligible frictional and other external forces, negligible gas velocity in the chamber, etc. However, these assumptions are no longer valid for 3D mironozzle flow. For instance, in the micron scale of the micronozzle, viscous forces become important which can no longer be assumed as negligible. Nevertheless, ideal rocket theory equations are used to predict the performances for micronozzle in comparison to the numerical results. Also, ideal equations provide an approximation for parameters to be used in the numerical simulation setup.

The mass flow rate is given by Equation 4.6, where R = specific gas constant, p_c = chamber pressure, T_c = chamber temperature, A_t = nozzle throat area, Γ = Vandenkerckhove parameter.

$$\dot{m} = \frac{\Gamma \cdot p_c \cdot A_t}{\sqrt{R \cdot T_c}} \tag{4.6}$$

The Vandenkerckhove parameter is defined as Equation 4.7 with γ = specific heat ratio.

$$\Gamma = \sqrt{\gamma} \cdot \left(\frac{2}{\gamma + 1}\right)^{\left(\frac{\gamma+1}{2(\gamma-1)}\right)} \tag{4.7}$$

Exhaust velocity can be calculated by Equation 4.8, where $\frac{p_e}{p_c}$ is a ratio of pressure at nozzle exit to pressure in chamber.

$$V_e = \sqrt{\frac{2\gamma}{\gamma - 1} \cdot RT_c \cdot \left(1 - \left(\frac{p_e}{p_c}\right)^{\left(\frac{\gamma-1}{\gamma}\right)}\right)} \tag{4.8}$$

The pressure ratio can be calculated by solving Equation 4.9, where, $\frac{A_e}{A_t}$ is the ratio of nozzle exit area to nozzle throat area.

$$\frac{A_e}{A_t} = \frac{\Gamma}{\sqrt{\frac{2\gamma}{\gamma-1} \cdot \left(\frac{p_e}{p_c}\right)^{\left(\frac{2}{\gamma}\right)} \left(1 - \left(\frac{p_e}{p_c}\right)^{\left(\frac{\gamma-1}{\gamma}\right)}\right)}} \tag{4.9}$$

The VLM microthruster performances are driven by the requirements stated in [81]. According to this, the minimum thrust provided by the microthruster shall be 0.12 mN and a maximum of 3 mN, power consumption by the heater shall not be higher than 4 W and internal pressure shall not exceed 10 bar. Additionally, the current simulation assumes a continuum fluid flow represented by the throat Knudsen requirement Kn < 0.01 as noted in section 4.2.

Based on the area ratio $\frac{A_e}{A_t}$ of 20 and Equation 4.9, the pressure ratio $\frac{p_e}{p_c}$ = 0.002618 can be calculated. The chamber pressure range can be chosen, and the corresponding nozzle exit pressure can be computed with $\frac{p_e}{p_c}$. For the given chamber pressure, considering water enters the heater chamber at a room temperature of 20° C and exits as completely vaporized gas at around T_c = 500 K [32], the mass flow rate for the sonic condition at the throat can be calculated with Equation 4.6. Using mass flow rate, pressure ratio, and exit velocity with Equation 4.8, the thrust delivered is given by Equation 2.6.

Power required to heat the liquid water at the heater chamber, turning it into vapor, is computed as a sum of sensible heat (heat needed to increase the temperature of liquid and vapor) and latent heat of vaporization. The heat required is calculated from the enthalpy data acquired from the NIST [63] database at the corresponding pressure and saturation temperature.

Similarly, the Reynold number at the throat Re_t is calculated from Equation 4.10 where, ρ = density of vapor, V = velocity, D_h = hydraulic diameter, $\dot{m}$ = mass flow, μ = dynamic viscosity and A_t = throat cross-sectional area.

$$Re_t = \frac{\rho V D_h}{\mu} = \frac{\dot{m} D_h}{\mu A_t} \tag{4.10}$$

Knudsen number at the throat is computed as Equation 4.11 with known Re_t where, M = throat Mach number, γ = specific heat ratio and Re_t = Reynolds at throat.

$$Kn = \sqrt{\frac{\gamma\pi}{2}} \frac{M}{Re_t} \tag{4.11}$$

Based on the 1D ideal rocket equations, the mass flow rate, thrust, Isp, power consumption, Reynolds number at the throat, and Knudsen at the throat for a range of chamber pressure is presented in Table 4.2. It is evident from the values obtained that the VLM microthruster aligns with the maximum thrust requirement of 3 mN until a chamber pressure of 2 bar. The operating pressure range is further limited to 1.01325 bar by the maximum power consumption requirement of 4 W. Since it was found in the literature that the upstream microchannel numerical simulation is mostly performed at an operating pressure equal to atmospheric pressure, a pressure of 1.1032 bar has been included in the pressure range. As observed in the table, the VLM microthruster operated at 1.01325 bar satisfies the maximum thrust and power requirement. Similarly, Knudsen at throat values do not exceed the 0.01 point, beyond which the continuum approach is inaccurate. Thus, the simulation setup for the VLM micronozzle in the subsequent section will approximate the pressure of 1.01325 bar at the heater chamber microchannel followed by a micronozzle. Similarly, the Reynolds number is low enough for the flow to be considered laminar, which is further supported by the results of Torre [103]. According to this, there is little time and space for turbulence in the micronozzle to develop. As such, all simulations in this study assume laminar flow and do not present a turbulence model.

Table 4.2: Micronozzle performance based on 1D ideal rocket theory

p_c [bar]	Mass flow [mg/s]	Thrust [mN]	Isp	Q [W]	Re_t	Kn
0.5	0.526	0.643	124.767	1.496	361.324	4.005e-03
1	1.051	1.291	125.203	2.990	722.649	2.003e-03
1.01325	1.065	1.308	125.209	3.029	732.224	1.976e-03
1.5	1.577	1.939	125.349	4.482	1083.973	1.335e-03
2	2.102	2.587	125.422	5.972	1445.298	1.001e-03
2.5	2.628	3.234	125.465	7.459	1806.622	8.011e-04
3	3.153	3.882	125.494	8.945	2167.947	6.675e-04

Properties of water vapor and VLM dimensional characteristics used in the calculation above are provided in Table 4.3.

Table 4.3: Properties of water vapor and VLM dimensional characteristics

Parameters	Values
gamma [-]	1.333
R [J/ kg K]	461.497
μ [Pa s]	1.45E-05
A_t [m^2]	7.5E-09
D_h [μm]	75
p_e/p_c	0.0026

4.5. Numerical setup

This section provides details on thermophysical properties used in the model, boundary conditions applied, and the simulation initialization method.

4.5.1. Thermophysical properties

In section 4.3, the five equations govern the fluid flow behavior with the following specified thermophysical models applied.

Density ρ

Under low pressure and high temperatures, water vapor tends to behave like an ideal gas. In the fluent solver, the density for a compressible fluid can be estimated based on an ideal gas law, described in

Equation 4.12, where, p = local static pressure, R = universal gas constant, M_w = gas molecular weight and T = temperature.

$$\rho = \frac{p}{\frac{R}{M_w}T}$$

(4.12)

Dynamic Viscosity μ

Sutherland [96] had provided an approximation to the dynamic viscosity, μ, depending on temperature of the ideal gas. Sutherland's law, as expressed in Equation 4.13, is centered on the kinetic theory of ideal gas and intermolecular forces. The three-coefficient Sutherland model includes μ_0 = reference viscosity, T_0 = reference temperature, and S = effective temperature or Sutherland constant. Viscosity and temperature data from NIST [63] were used to fit the relation below, resulting in the Sutherland constant. Table 4.4 shows the values for the three coefficients used.

$$\mu(T) = \mu_0 \left(\frac{T}{T_0}\right)^{3/2} \frac{T_0 + S}{T + S}$$

(4.13)

Table 4.4: Sutherland reference values and constant defining temperature dependent dynamic viscosity

μ_0 [Kg/ m s]	9.14E-06
T_0 [K]	279.79
S [K]	498.789

Specific heat c_p

Within fluent's material properties, specific heat capacity (c_p) can be modeled as a function of the fluid's temperature in the polynomial form written below in Equation 4.14.

$$c_p(T) = A_1 + A_2 T + A_3 T^2 + ...$$

(4.14)

[76] contains large thermodynamic data for several gases and liquids species. It also provides a relation fitted in the fourth polynomial order shown in Equation 4.15 for specific heat as a function of temperature, including water vapor. In the temperature range of $200 \leq T \leq 1000$ K, the values of the coefficient given are $a_1 = 4.20$, $a_2 = -2.04e-03$, $a_3 = 6.52e-06$, $a_4 = -5.49e-09$ and $a_5 = 1.77e-12$. For a temperature range of $1000 \leq T \leq 6000$ K, the coefficients are $a_1 = 2.68$, $a_2 = 2.97e-03$, $a_3 = -7.74e-07$, $a_4 = 9.44e-11$ and $a_5 = -4.27e-15$.

$$\frac{c_p(T)}{R} = a_1 + a_2 T + a_3 T^2 + a_4 T^3 + a_5 T^4$$

(4.15)

Similarly, Cooper [30] had accurately replicated values of specific heat (c_p/R) of water vapor fitted to the data of Woolley [108]. But Cooper equation needed to be accommodated to a polynomial form used in fluent properties input. A fourth-degree polynomial was thus fitted to the c_p values of Cooper, as represented in Figure 4.2 The resulting single equation is valid for a wide range of temperatures $50 \leq T \leq 5000$ K and exactly accurate in the range of $130 \leq T \leq 2000$ K compared to [76]. This is why the equation was used for the micronozzle c_p model. As a result, coefficients in form of Equation 4.15 are $a_1 = 4.0560, a_2 = -0.0007845, a_3 = 3.0140e-06, a_4 = -1.5928e-09, a_5 = 2.7242e-13$. Figure 4.3 shows a good agreement of the fit obtained with the relation of [76].

Thermal conductivity k

Thermal conductivity is modeled based on the kinetic theory of ideal gases. In fluent, thermal conductivity for ideal gases is defined by Equation 4.16 where R = universal gas constant, M_w = gas molecular weight, c_p = specific heat capacity, and μ = dynamic viscosity.

$$k = \frac{15}{4} \frac{R}{M_w} \mu \left[\frac{4}{5} \frac{c_p M_w}{R} + \frac{1}{3} \right]$$

(4.16)
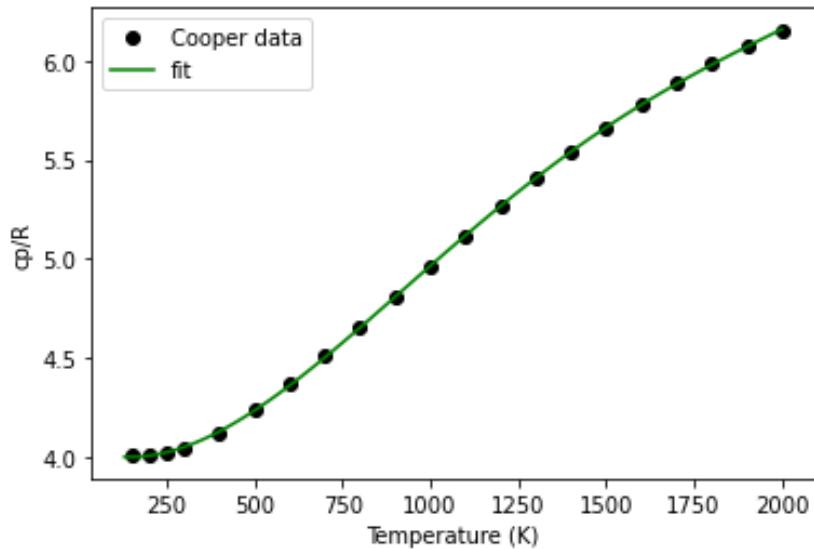
Figure 4.2: Cooper data fitted to a fourth degree polynomial
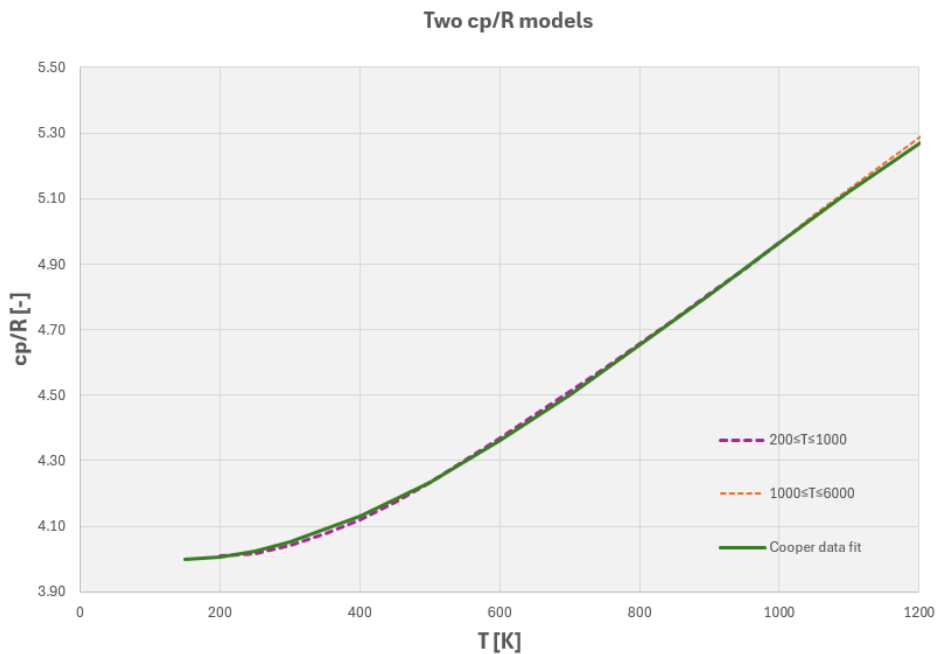
Figure 4.3: Cooper fit compared to the McBride, Gordon, and Reno [76] relation for two temperature ranges.

[8]

4.5.2. Boundary conditions
Boundary conditions are applied to the computational fluid domain to solve the flow, which is explained below.

Computational domain
Flow through the micronozzle is represented in the computational domain as shown in Figure 4.4, where the fluid inlet, micronozzle walls, plume walls, symmetry, and outlet are shown. A quarter of the micronozzle is taken due to the symmetric nature of the flow solution for the micronozzle. Since the solution is computationally extensive, this helps reduce the resources and time for simulation. The computational mesh for the CFD simulations has been built in ICEM CFD available with Ansys which

are presented in the respective sections below. These boundary conditions are subsequently discussed in the following.
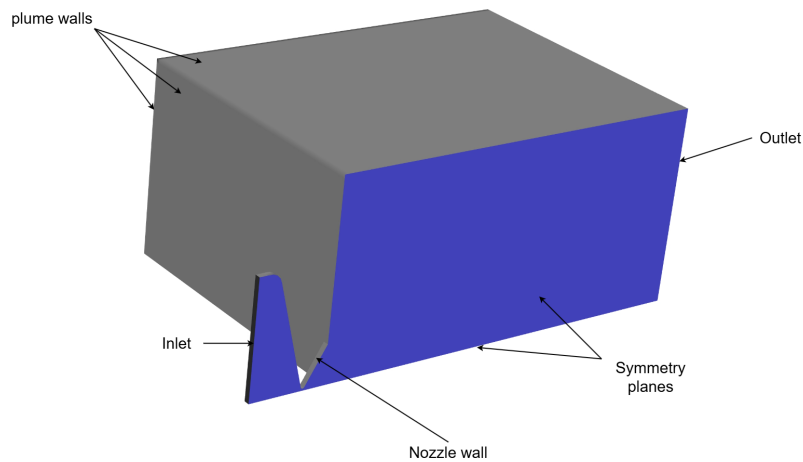
Figure 4.4: Fluid computation domain used in the micronozzle flow simulation

Inlet

The inlet of micronozzle was chosen as a pressure inlet where total pressure $P_{0,inlet}$ and total temperature $T_{0,inlet}$ of the flow needs to be specified. Flow is initialized with a subsonic compressible flow at the inlet.

Walls

The micronozzle's walls are modeled as adiabatic walls with negligible heat transfer between fluid and wall. Several studies including [70] [4] [85] support this model. Since the operation timescale of microthruster is much smaller than the time scales concerning heat transfer, such a model had been deemed appropriate for the study. Thus, a zero heat flux is assigned at the micronozzle walls.

Navier-stokes equations are usually solved with no-slip boundary conditions, where near-wall flow velocity is zero for a stationary wall. However, as the characteristic length of the structure becomes comparably similar to the flow molecular mean free path λ, flow experiences a discontinuity in velocity and temperature at the wall-normal direction. The velocity of flow can not be assumed zero at the wall as shown in Figure 4.5, the flow appears to be slipping.
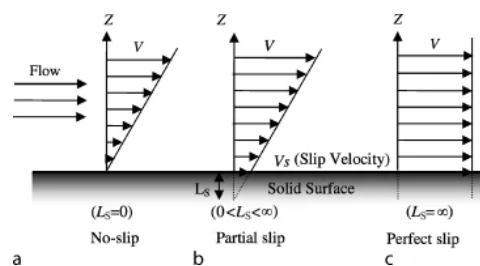
Figure 4.5: a) Velocity at the wall in a) no-slip b) partial slip and c) perfect slip condition. Velocity is zero at an imaginary distance below the wall called slip length (L_s) in partial slip.

[82]

Following what was previously mentioned in section 4.2, the Navier-Stokes-based equations with appropriate slip conditions are accurate until micronozzle throat Kn<0.01, beyond which rarefaction effects invalidate the use of continuum hypothesis. The slip conditions are applied at the micronozzle wall boundary through the slip boundary formulation in fluent. It uses Maxwell [75] model for slip velocity

and temperature jump stated in Equation 4.17 and Equation 4.18 respectively, where, u = x-component of velocity, T = temperature, g = gas, w = wall, n = direction perpendicular to the wall, x = direction tangential to the wall, σ = tangential momentum accommodation coefficient (TMAC), α = equivalent thermal accommodation coefficient (TAC), μ = gas dynamic viscosity, ρ = gas density, and λ = molecular mean free path.

$$u_w - u_g = \left(\frac{2 - \sigma}{\sigma} \right) \lambda \frac{\partial u}{\partial n} + \frac{3}{4} \frac{\mu}{\rho T} \frac{\partial T}{\partial x} \tag{4.17}$$

$$T_w - T_g = \frac{2 - \alpha}{\alpha} \lambda_T \frac{\partial T}{\partial n} \tag{4.18}$$

λ_T represents an equivalent thermal mean free path described by Equation 4.19.

$$\lambda_T = \frac{2}{(\gamma + 1)} \frac{k}{\rho c_v} \sqrt{\frac{\pi}{2RT}} \tag{4.19}$$

In Equation 4.17, the second term denotes the effect of the temperature gradient along the wall driving the motion of rarefied flow from cold to warm regions. This effect is known as thermal creep. Tangential accommodation coefficient σ ranges from 0 to 1, where 0 represents no exchange of momentum with the wall by gas during a collision and 1 represents complete accommodation of wall tangential momentum by gas, i.e., gas molecules lose their tangential momentum to the wall.

Appropriate values of the momentum and thermal accommodation coefficients were assessed throughout the literature. In [10], the experimental measurement for silicon substrate using nitrogen, argon, and carbon dioxide, stated TMAC values in the range of 0.75-0.85 but was not available for water vapor. Likewise, Yamaguchi et al. [112] tested with water to evaluate the values of TMAC and TAC. However, a platinum surface was used in their experiment rather than silicon. Louisos and Hitt [70], had used values of TMAC = 0.85 in their numerical study. TMAC value of 0.8 was used by De Giorgi and Fontanarosa [32]. Thus, as approximated values in the following simulations, σ = 0.8 and α = 0.85 are taken.

The plume walls (also outlet) are domains extended far downstream of the actual exit of the micronozzle such that it does not affect the nozzle exit flow. These plume walls can be modeled as outlets where fluid flows out across the boundaries. However, this led to flow reversals at the wall surfaces. Although not problematic in itself, it makes it difficult to detect errors. So the plume walls are modeled as inviscid walls which prevent the flow from exiting the domain while causing no viscous effects on the wall.

Outlet
After initialization of the flow field as a subsonic flow at the inlet, the micronnozzle flow can turn sonic at the throat, and a supersonic flow expansion can occur in the divergent section with a high enough pressure ratio for the given micronozzle area ratio. The outlet extending downstream of the exit is chosen as a pressure outlet where static pressure (ambient pressure) needs to be imposed. In the outlet boundary domain, flow could be both subsonic and supersonic. The specified static pressure is used at locations where the flow is subsonic. While pressure value is extrapolated from the interior supersonic section at the boundary location where the flow becomes supersonic. Also, backflow is allowed at the outlet such that the solution is physical, unlike what was done in [36].

4.5.3. Simulation initialization
Before the total pressure at the inlet and static pressure at the outlet could be specified to let the simulation run, it was important to maintain the given pressure ratio such that the solution did not diverge. The simulation is conducted in a vacuum environment with outlet pressure around 30 Pa whereas the chamber pressure inlet is much higher in the range of 1 bar (1×10^5 Pa). This pressure ratio of around 10000, leads to a high pressure gradient near the pressure inlet. Due to this, the solver tends to diverge, resulting in an inaccurate pressure field near the inlet.

Thus, the pressure at the inlet was gradually linearly increased over a certain period (5e-5 s), in the

transient solver. A coupled scheme for pressure velocity coupling is applied for the solution with second-order spatial discretization and first-order implicit transient formulation. The Courant–Friedrichs–Lewy (CFL) of 0.2 was used. Based on the mesh cell size and CFL number, an adaptive time stepping method with an initial time step size in the order of 1e-9 s to 1e-8 s was used. During the simulation, residuals at each time step are required to decrease below 1e-6. Once the required pressure ratio is established, the simulation is run for an additional period until a steady state condition is reached, which is represented by a constant Mach at the micronozzle exit. Additionally, the mass flow rate balance between the inlet and exit and pressure at the throat and exit are monitored to determine flow convergence.

Following the assessment of convergence, the flow field is processed to generate the characteristic contour of the flow field like Mach, and micronozzle performances are computed through the solver post-processing functions and mathematical computations available in fluent.

4.6. Numerical performance parameters

The performances of the micronozzle are defined mainly by thrust and specific impulse, as explained in subsection 2.2.1. From simulations, measured thrust is given by the integral form in Equation 4.20 where the first term represents momentum, the second is a pressure term and the third is a viscous stress that is applied to the thrust. [85] The equations below consist of ρ = density, $\vec{u}$ = velocity vector, $\vec{n}$ = unit normal vector, A_e = micronozzle exit area, p = exit pressure, p_a = ambient pressure and $\vec{\tau}$ = viscous stress tensor.

$$F_{CFD} = \iint_{A_e} \vec{u}(\rho\vec{u}.\vec{n})dA_e + \iint_{A_e} (p - p_a)\vec{n}dA_e - \iint_{A_e} (\vec{\tau}.\vec{n})dA_e \qquad (4.20)$$

Similarly, specific impulse is calculated as :

$$I_{sp,CFD} = \frac{F_{CFD}}{\dot{m}_{CFD}.g_0} \qquad (4.21)$$

Where mass flow $\dot{m}_{CFD}$ is computed from Equation 4.22

$$\dot{m}_{CFD} = \iint_{A_e} \rho(\vec{u}.\vec{n})dA \qquad (4.22)$$

Area-integrated mass flow rate, pressure, and viscous stress at the exit of the micronozzle can be obtained from the simulation solutions. The theoretical one-dimensional isentropic solution of the micronozzle based on ideal rocket theory (IRT) as explained in section 4.4 can be compared to the numerical performance of the micronozzle through the following parameters: discharge coefficient C_d, thrust efficiency η_F, and specific impulse efficiency $\eta_{I_{sp}}$ as computed from Equation 4.23, Equation 4.24 and Equation 4.25 respectively.

$$C_d = \frac{\dot{m}_{CFD}}{\dot{m}_{IRT}} \qquad (4.23)$$

$$\eta_F = \frac{F_{CFD}}{F_{IRT}} \qquad (4.24)$$

$$\eta_{I_{sp}} = \frac{I_{sp,CFD}}{I_{sp,IRT}} \qquad (4.25)$$

4.7. Validation

The above-described settings for the micronozzle flow with partial rarefaction must be tested against experimental data to provide validity to the simulation results for the VLM micronozzle. In literature, the experimental works by Cen and Xu [20] have been found to use water to test a MEMS-based VLM's performance. Figure 4.6 shows a schematic of the VLM used in the experiments, consisting of 9 parallel microchannels to vaporize the water and convergent-divergent micronozzle. They have been etched onto a silicon substrate with a depth of 120 μm. Dimensional characteristics of the micronozzle are shown in Figure 4.7 and tabulated in Table 4.5. [32] had attempted to validate their results by CFD simulation of the same micronozzle geometry of Cen and Xu.
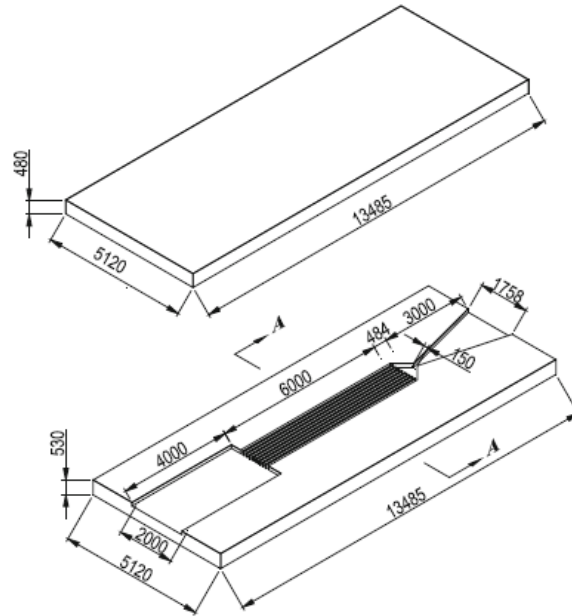
Figure 4.6: Cen and Xu's VLM structure
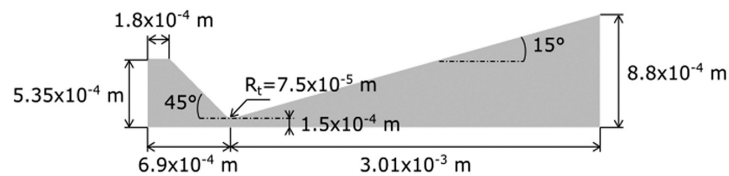
Figure 4.7: Cen and Xu's micronozzle geometry obtained from [38]

Table 4.5: Cen and Xu micronozzle dimensional characteristics

Micronozzle dimension	Values
Inlet width, W_{in} [μm]	1120
Throat width, W_t [μm]	150
Exit width, W_{out} [μm]	1760
Convergent angle, θ_{in}	45°
Divergent angle, θ_{out}	15°
Area ratio, A_e/A_t	11.733

In this study, Cen and Xu's micronozzle has been tested with the CFD simulation settings described above to reproduce their experimental results on performance. For the said simulation, total pressure and temperature at the inlet are taken from the experimental data, $P_{0,inlet}$ = 1 bar and $T_{0,inlet}$ = 453.15 K ($180^\circ C$). Cen and Xu observed that back pressure on the order of a hundred pascals had no significant impact on the thrust force. Thus, at the outlet, ambient static pressure assigned is, P_{outlet}

= 500 Pa. Although the VLM micronozzle of this study operates in almost vacuum condition of 30 Pa achieved by the vacuum chamber of the faculty.

For the 3D mesh of the micronozzle, the downstream stretched dimension of the domain is calculated in the direction of x = 10 W_{out}, y = 5 W_{out} and z = 50 z_{depth}. The 3D mesh is presented in Figure 4.8, which comprises 558,589 cells with the smallest cell size equal to 3.57 μm. Due to the combined simulation time associated with both micronozzle and microchannel simulation exceeding weeks to a month, the grid refinement study was not considered in this study. Instead, the grid was compared to that of [32], where a 2D grid refinement study was performed for the same micronozzle and under similar conditions including total pressure at inlet $\sim$ 2 bar and inlet temperature $\sim$ 505.58 K. According to this, three levels of refinement including fine, intermediate, and coarse meshes were tested. An intermediate-level mesh refinement with around 516,360 cells for 3D micronozzle mesh was considered accurate enough for the simulation, depending on the study.
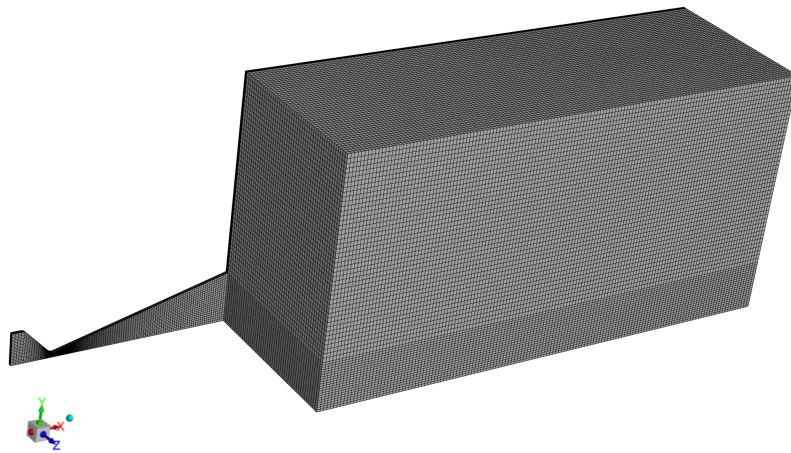
Figure 4.8: Mesh for Cen and Xu's micronozzle CFD simulation with the respective axes.

With mesh and numerical setup in place, the simulation was run until a steady state condition was reached, indicated by a constant Mach number at the exit of the micronozzle. Mach contour of the flow field is shown in Figure 4.9.
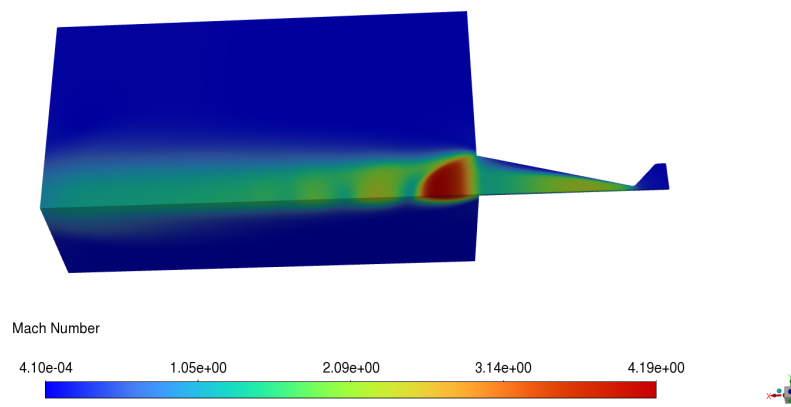
Figure 4.9: 3D Mach contour of Cen and Xu's micronozzle simulation

Although plume modeling is not focused on the current study, interesting patterns are seen in Figure 4.9. The plume Mach pattern is comparable to an underexpanded nozzle exhaust shown in
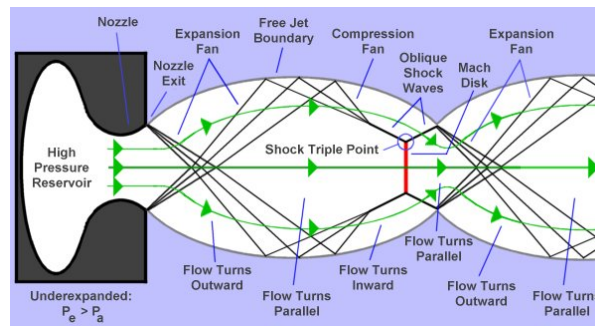
Figure 4.10: Plume in an underexpanded nozzle [90]

Figure 4.10 with nozzle exit pressure higher than the ambient pressure ($P_e > P_a$). The Mach contour obtained is also consistent with the Mach contour achieved by the CFD simulation of De Giorgi and Fontanarosa which makes use of a slightly different set of inlet and outlet conditions to what was simulated for this study. Observed in the Figure 4.9, the underexpanded exhaust gases propagate through the set of expansion and compression waves until the gases gradually adjust with the external ambient pressure. In the nozzle exit lips, a pair of expansion waves can be seen to form, which are reflected and merged into oblique shocks forming a normal Mach disc, behind which an increase in pressure forms a region of subsonic flow.

In Figure 4.11, the throat Knudsen number can be observed as less than 0.01 which is the boundary of the continuum flow hypothesis from Torre. Similarly, in the rest of the divergent section, the local Kn is within the slip flow regime of 0.1. Flow thus satisfies the limit, and the continuum assumption is valid for this micronozzle.
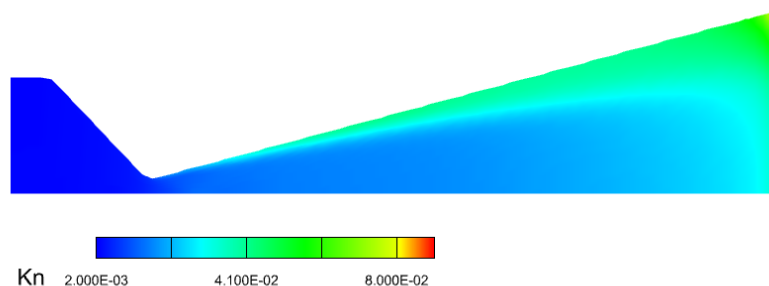
Figure 4.11: Cen and Xu's micronozzle local Knudsen

Mach contour in the convergent and divergent section is further explained in section 4.8. Since the primary objective is to compare the micronozzle performance with experimental data of Cen and Xu, mass flow rate, thrust, and specific impulse are computed and presented in Table 4.6. The CFD results and experimental data from Cen and Xu show a variance within a 10% margin. The mass flow rate shows a large difference, although the simulation made sure that the imbalance was kept to a minimum, resulting in the mass flow rate at nozzle inlet = 2.58e-06 kg/s and exit = 2.54e-06 kg/s. Contours like Mach were not found in Cen and Xu's data, as the experiment mostly focused on performance. As such, the numerical setup is established and validated for the VLM micronozzle simulation.

4.8. Numerical results

The geometry of the next generation TU Delft VLM micronozzle is detailed in section 4.1. Figure 4.12 shows the mesh used for the simulation. The extended domain dimension is again calculated in the direction of x = 10 W_{out}, y = 5 W_{out}, and z = z_{depth}. Unlike during meshing of Cen and Xu's micronozzle,

Table 4.6: CFD and experimental data comparison

	Cen and Xu experiment	CFD model	Difference [%]
Mass flow [mg/min]	140	**152.19**	8.707
Thrust [mN]	1.98	**2.09**	5.533
Specific impulse [s]	85.9	**84.825**	1.251

the domain in the z-direction is taken equal to the nozzle depth. There are several related reasons, the first being the focus on performance prediction, rather than plume modeling. As long as the pressure outlet did not influence the nozzle exit and thrust produced, this is considered acceptable. Secondly, the exhaust plume followed a nozzle exit rectangular cross-sectional shaped path known from the simulation of Cen and Xu micronozzle. To reduce the computational and time resources, the mesh domain is thus limited to the depth of the micronozzle. Lastly, the solver showed divergence errors stemming from the low-pressure locations in the z-direction extended domain where the pressure dropped below 0 Pa, which is nonphysical. This was only evident after multiple runs that implemented various techniques to prevent such errors, including plume mesh refinement and increment of mesh cell quality, which did not suffice. Furthermore, a similar downstream domain configuration is seen in the study of [64]. The resulting mesh consists of 97,652 cells, with much finer cells on the order of 1.316 μm near the throat area and coarser cells on the order of 37.037 μm near in plume regions. Confidence in the mesh is derived from the 3D mesh refinement study of micronozzle in [36] where mesh consisting of around 100,000 cells was considered fine enough to calculate the micronozzle performances. The micronozzle total length in [36] is longer (due to lower convergence and divergence angles than used in the current study), the inlet width is the same, the outlet width is smaller by $\sim$ 200 μm, and the throat width is similar. Based on this, the VLM micronozzle size in this study is similar to or even smaller than the micronozzle size of [36]. The conditions under which the simulation was performed are also similar, with inlet pressure in the range of 0.2-3 bar and ambient pressure at 30 Pa. Thus, the number of cells used for the VLM micronozzle's 3D mesh in this study is in similar order.
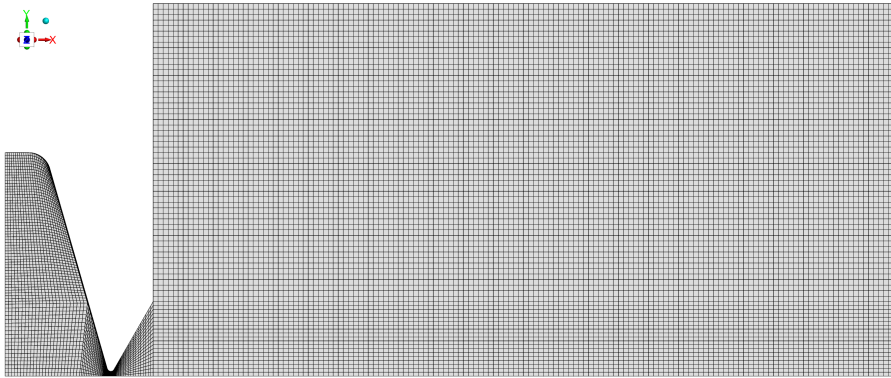
Figure 4.12: VLM micronozzle 3D mesh

For the simulation as mentioned in section 4.4, inlet total pressure, $P_{0,inlet}$ = 1.01325 bar and inlet total temperature $T_{0,inlet}$ = 500 K is assigned to the inlet boundary of the mesh. At the outlet boundary, ambient static pressure, P_a = 30 Pa, is applied. As explained in subsection 4.5.2, partial slip conditions are applied to the micronozzle walls. The flow solution obtained is explained as follows, supported by the Mach, pressure, and Kn contours.

Figure 4.13 shows the Mach contour of the flow in VLM micronozzle obtained from the simulation. 3D viscous layers are illustrated in Figure 4.14, where subsonic layers are seen near the walls. Compared to a 2D micronozzle, viscous effects in a 3D micronozzle are associated with subsonic layers not only at the top and bottom walls but also at the walls perpendicular to the z-direction/ depth direction. Subsonic layers in 3D micronozzle flow are characterized by the overlap of the subsonic layers at

the corners arising from adjacent walls, visible in Figure 4.15. The depth and divergence angle of the micronozzle are very closely interrelated with each other concerning the thrust performance and the subsonic portion present in the micronozzle cross-section. A detailed investigation of the relation is out of the scope of the present study. However, several points can be noted when compared to the results found in the literature. In [36], nitrogen flow in linear micronozzles with etch depth = 100 μm, throat width W_t = 45 μm and area ratio $A_e/A_t = 16.971$ were numerically compared for different divergence angles of $15°$, $30°$ and $45°$. Regarding the subsonic portion of the micronozzle exit cross-sectional area, the results for low Reynolds number indicated a significant reduction in subsonic area with an increase in divergent angle from $15°$ to $30°$. But such a decline in the subsonic area was not apparent for an increase from $30°$ to $45°$. As this analysis did not investigate the effects of micronozzle depth on the subsonic layers, it could not conclusively explain the effect of the increasing divergence angle on the reduction of cross-sectional subsonic area.

A more detailed analysis of the 3D micronozzle viscous boundary layer, found in [70], presents a comparison of the effects of depth on the subsonic cross-sectional area for the same range of divergence angles. The study was performed for a micronozzle area ratio of 6.22 and etch depth of 25 to 400 μm. At lower throat Reynolds number (Re $\leq$ 300) with depths of micronozzles around 25-50 μm, the $30°$ divergent micronozzle showed almost no supersonic flow, with the subsonic layer growing large enough to merge into a complete subsonic flow. Between the micronozzle depth of 100 to 200 μm, the largest divergence angle of $45°$ had the smallest portion of the subsonic layer in the cross-sectional exit area. As such, the viscous effects were smaller for increasing divergence angle and micronozzle depth.
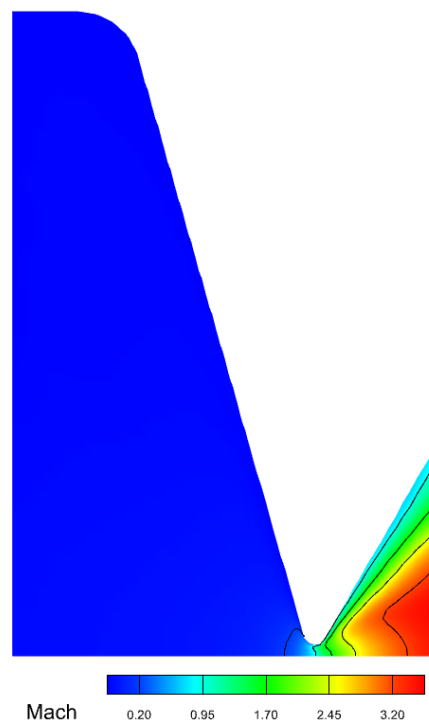
Figure 4.13: VLM micronozzle mach contour

In the current study of micronozzle flow, the divergence angle ($60°$), area ratio (20), throat width (50 μm), Reynolds ($\sim$ 732.224), and etch depth (150 μm) are all higher than the third generation linear micronozzle of [36]. The divergence angle is particularly higher than that found in the literature. Based on the discussion above, a larger divergence angle and depth would cause the reduced subsonic cross-sectional area seen in Figure 4.15 compared to the simulation of previous micronozzle by Ganani [36]. This is related to the large divergence angle associated with diminished viscous layer growth along the top and bottom walls due to the reduced distance through which the flow boundary layer traverses. This can be noticed in Figure 4.16 where the subsonic layer thickness is increasing towards the nozzle
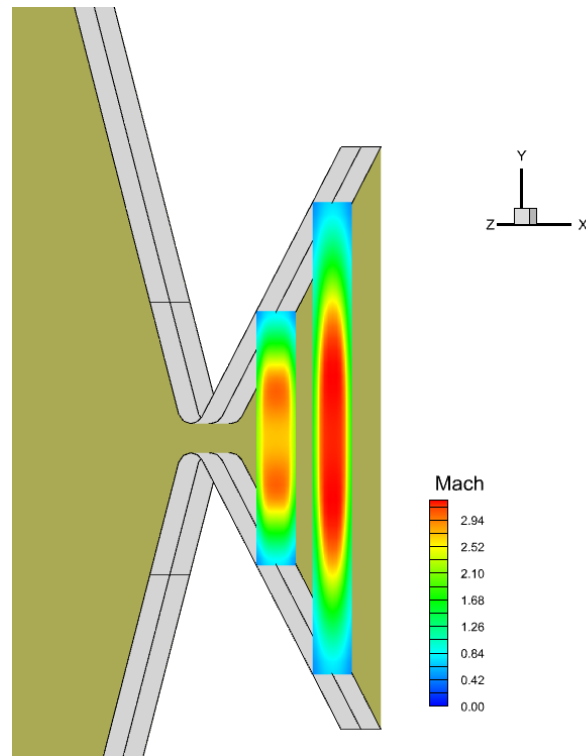
Figure 4.14: VLM micronozzle cross-sectional Mach contour shown at around 50 % and 75 % distances from the throat

exit, as this distance shortens the thickness of the layer is limited at the exit.

Also observed is the absence of a visible subsonic layer at the walls perpendicular to the depth direction. The subsonic layer on the wall is seen away from the core flow towards the top and bottom walls. This could be due to the rapid expansion of supersonic core flow through the nozzle and the boundary layer being too thin, almost negligible. Regardless, a more thorough analysis covering the effects of other parameters including area ratio, throat width, and Reynolds number is necessitated for a conclusive remark.

In line with what was noted in subsection 4.5.3, the high-pressure ratio over the micronozzle inlet to the outlet was gradually maintained, which was further exacerbated by the high-pressure gradient imposed by the abrupt convergent angle of 70°. For a long time, flow entering the domain created a high-pressure region near the inlet, where fluid particles slowed down along the convergent surface. Due to the sudden bend in the geometry, rather than gradual, flow entering the domain tended to separate and flow out of the domain. The flow reversal and flow out of the domain caused the solver to diverge. To get the solver running, the entrance region could be extended such that backflow does not occur at the inlet. However, due to time constraints, an artificial barrier was used instead by the solver to prevent flow from leaving through the inlet boundary, so the solution does not diverge. In reality, this phenomenon is likely to occur, which should be prevented for the device to perform as predicted and prevent instability. The pressure field is shown in Figure 4.17 and the pressure ratio of static pressure to the total chamber pressure obtained can be seen in Figure 4.18. With ambient pressure P_a = 30 Pa assigned at the outlet, the resulting area-averaged micronozzle exit pressure P_e = 1048.856 Pa, indicating an underexpanded nozzle.

In Figure 4.19, the Knudsen flow field is displayed. A continuum flow assumption was made before the simulation was initiated, dependent on the throat Knudsen number calculated in section 4.4 with throat Reynolds and Mach number determined for a 1D micronozzle. The assumption implies a throat Kn<0.01 would correspond to a continuum medium with partial rarefaction present. As evaluated from the simulation results on Knudsen, the value of Knudsen around the throat is 0.01, and a large part
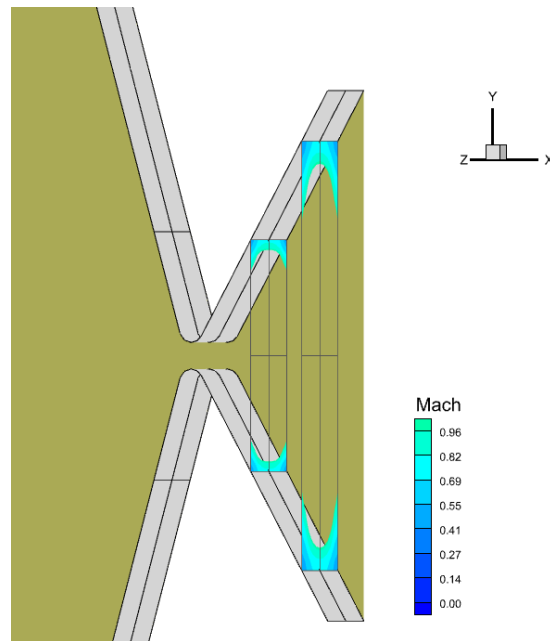
Figure 4.15: Subsonic layer portion with Mach<1 of the micronozzle cross-sectional area and the transparent area representing supersonic core flow
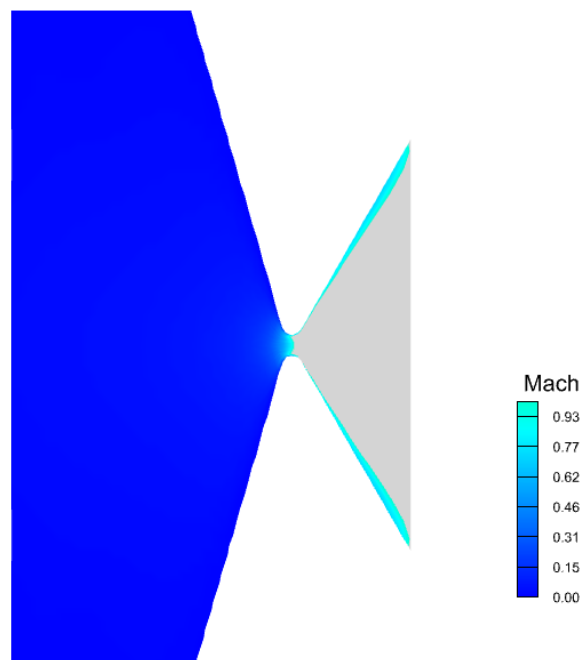
Figure 4.16: VLM micronozzle subsonic layer growth along the divergent section top and bottom walls

of the divergent section is indeed within the slip flow regime. Only part of the divergent section towards the corner is seen to exceed the slip regime limit. This is partly because of the ambient pressure of 30 Pa unlike the pressure of 500 Pa used in the validation simulation in section 4.7, which causes the flow to expand to very low pressures, reaching a higher Knudsen number than was anticipated. Irrespective of the above, the continuum flow is still valid for most of the nozzle flow.

The resulting performances of the linear micronozzle extracted from the numerical simulation and described in section 4.6, include exit mass flow = 0.972 mg/s, thrust = 1.161 mN, and I_{sp} = 123.925.
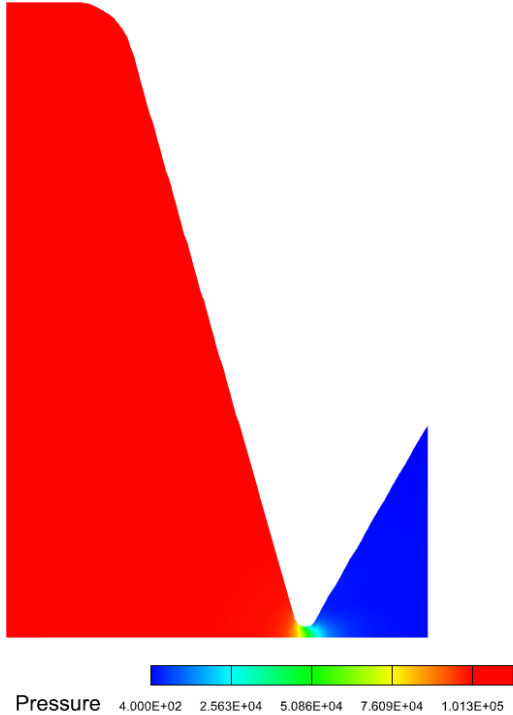
Figure 4.17: VLM micronozzle pressure field
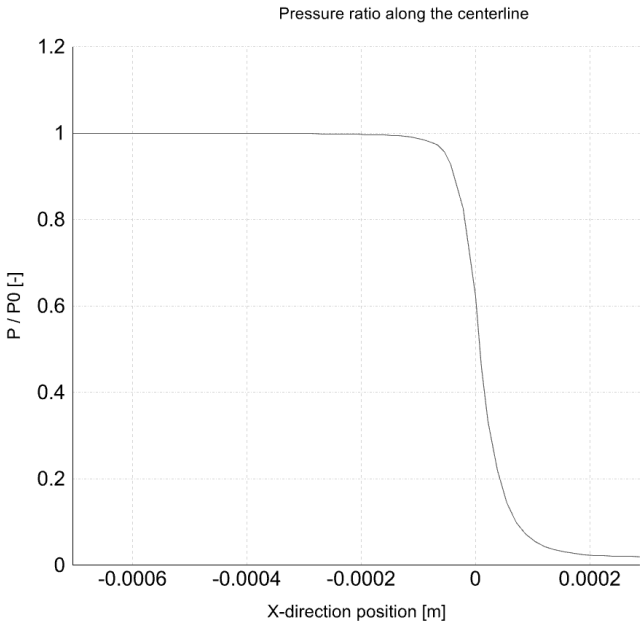
Figure 4.18: Static pressure to total pressure ratio (P/P_0) along the micronozzle centerline from entrance to exit.

C_d, η_F and η_{Isp} are calculated for the microchannel flow compared to the performance of idealized 1D micronozzle flow calculated in section 4.4. These values are assessed based on the third-generation micronozzle numerical performance investigated by Ganani [36]. In that study, for the ranges of throat Reynolds 500-1000, 45° divergent linear micronozzle was found to exceed performances of other 15° and 30° linear micronozzles. Table 4.7 presents the findings from the current study performed for a throat Reynolds of ~ 732.2. As can be observed, the current micronozzle performance is the highest
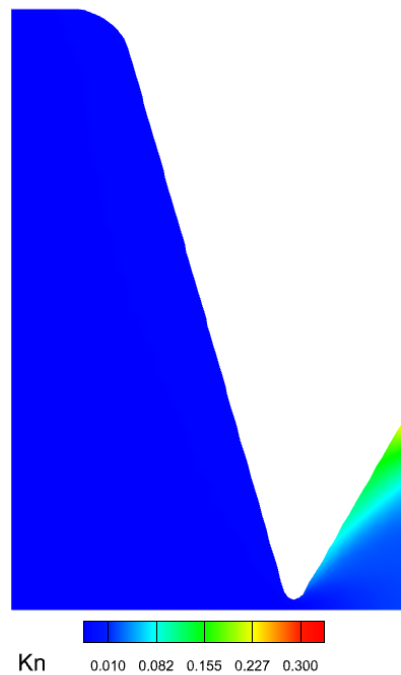
Figure 4.19: VLM micronozzle Knudsen contour

for all parameters. It must be noted that the performances obtained by Ganani are based on nitrogen gas as a propellant, whereas water vapor has been used in this study.

Table 4.7: Numerical performances of the fourth/new generation VLM microthrusters compared to the third generation VLM

	$Re_t \sim 732.224$	Ganani, $Re_t \sim 500\text{-}1000$
C_d	0.913	0.86-0.88
η_F	0.888	0.72-0.756
η_{Isp}	0.990	0.84-0.86

4.9. Concluding remarks

Numerical results included the validation study, which validated the performances of Cen and Xu micronozzle within 10% deviation from the experimental data. The VLM micronozzle simulation resulted in performance characterization including mass flow, thrust, and specific impulse. Flow field characteristics were demonstrated in mach contour, pressure contour, and ratio plots. Discharge coefficient and nozzle efficiencies were calculated as well and compared to that of the third-generation micronozzle under a similar throat Reynolds number.

Mach contours and subsonic layers (Mach<1) over the divergent section walls together with the values of discharge coefficient show the effects of the viscous boundary layer. Compared to Ganani's micronozzle, the visible subsonic layer seen in the VLM micronozzle (also indicated by the discharge coefficient value of 0.913) has greatly reduced, allowing a greater fraction of the divergent section to expand into supersonic flow. This is an improvement in the design of the VLM micronozzle, provided by the higher divergence angle. As explained previously, a higher divergence angle allows the flow to expand rapidly and shortens the total length of the micronozzle for the same area ratio. In consequence, viscous effects can not take place as fast and as further over the micronozzle length due to limited growth of the viscous boundary layer. This means no drastic change/correction in the geometric throat area is needed, since the effective area ratio is similar to the actual geometric area ratio. Although a

small portion of the divergent cross-section is covered by the subsonic layer, this is much more satisfactory compared to Ganani's micronozzle and is expected to improve performances in the real VLM.

Thrust efficiency on the other hand, although better than Ganani's micronozzle does not improve significantly compared to the improved discharge coefficient. A comparable enhancement was expected since thrust performance also benefits from the lower contribution of viscous effects and the viscous effects are very small. The source could be the same higher divergence angle. Although it reduces the viscous effects, it simultaneously promotes geometric loss associated with stronger non-axial velocity components. This means the divergence angle of the VLM micronozzle should be designed to balance the geometric losses and viscous losses. Another option could be operating the real VLM at a higher operating pressure than 1 atm, leading to a higher mass flow rate and thrust production and compensating for the geometric loss. However, this has penalties on the heater vaporization power plus lower heat transfer effects.

Another prediction that can be made from the CFD simulation not immediately apparent through the performance parameter is the flow instability occurring from the flow reversal near the entrance. Although not a problem with the simulation, this can affect the real VLM operation. This effect is suspected to be a consequence of the high convergent angle, as explained previously. The high convergence can help shorten the length of the micronozzle, but it does not prove as essential as the magnitude of the divergence angle. Because most of the flow in the convergent section is subsonic and viscous boundary layer effects are mostly prevalent in the divergent part, the convergence angle could be reduced for the VLM design. This is predicted to help reduce the flow reversal and pressure losses.

Finally, some comparison of the operation conditions resulting from the micronozzle simulation and the one used in the microchannel model could be made to appreciate the differences. The mass flow rate obtained from the VLM micronozzle simulation needed to be matched with the mass flow rate at the microchannel. The first simulation of the microchannel was initiated based on the chocked mass flow rate value at the inlet and outlet pressure of 1 atm. Simultaneously, the micronozzle model was run with pressure at the inlet of 1 atm and assuming the temperature of water vapor $\sim$ 500 K. Afterward, the microchannel flow model was evaluated, where it was found that backflow occurs at the outlet. To counteract this, results away from the outlet where backflow effects were not present could be taken. However, due to the numerical instability of the microchannel flow complete transition to vapor could not be achieved. This means results of the flow field near the outlet of the microchannel could not be compared to the micronozzle inlet conditions. So the mass flow rate matching by re-iterating the microchannel simulation with the corresponding inlet conditions could not guarantee better results. Combined with the reasons stated in section 3.7, coupling of the two models was thus not achieved.

5

Conclusions and recommendations

In the chapter, the main conclusions derived from the thesis work are presented in section 5.1 and the recommendations for further research are given in section 5.2.

5.1. Conclusions

The objective of this research as reiterated here is to evaluate the performance of next-generation MEMS (micro electro mechanical systems) VLMs (vaporizing liquid micro-resistojet) by creating a numerical simulation model for the heater microchannel and micronozzle of the VLM and validating the model using existing experimental data. To this end, a multiphase flow computational fluid dynamics (CFD) model using the Volume of Liquid (VOF) method was implemented to simulate the two-phase flow occurring in the VLM microchannel and the micronozzle flow solution with water vapor as the propellant was achieved using a pressure-based solver with partial flow rarefaction effects implemented through slip flow conditions in the model. VLM consists of five parallel serpentine microchannels which were reduced to a single straight microchannel for simplification of purposes in this study. A 2d rectangular microchannel mesh was employed in the solver to obtain the flow solution. Conversely, a 3D linear convergent-divergent micronozzle with convergence angle $\theta_{in} = 70^{\circ}$, divergence angle $\theta_{out} = 60^{\circ}$ and throat width W_t = 50 μm was modeled in CFD to evaluate the micronozzle performances. A quarter of the 3D geometry was used due to the symmetric nature of the micronozzle flow. Both of the numerical models were validated against the experimental data, as explained below. The aim of the research is further detailed through the research questions, which are answered as follows:

How accurately can the heater microchannel and micronozzle of next-generation MEMS VLMs be numerically simulated to predict flow characteristics and assess VLM performance?

The sub-questions for the main research question are:

What are the flow characteristics and performance parameters that can be determined through numerical simulation of VLM heater chamber and micronozzle?

VLM microchannel flow simulation resulted in the visualization of flow patterns in the microchannel and heat transfer characteristics were obtained with the transient averaged wall temperatures and fluid bulk temperature extracted from the simulation results. In the VLM microchannel flow boiling process, bubble nucleation, growth, and flow regime transitions can be observed. Characteristic bubble elongation due to the confinement effect of the microchannel is present in the VLM microchannel flow. The main heat transfer mechanism of microlayer evaporation beneath the vapor-liquid interface was identified in the process.

Similarly, VLM micronozzle simulation with partial slip flow model was used to extract the thrust, specific impulse, mass flow rate and nozzle efficiencies compared to 1D isentropic flow including, dis-

charge coefficient C_d, thrust efficiency η_F and specific impulse efficiency η_{Isp} of the micronozzle at the operating chamber pressure of 1 atmospheric pressure (atm). Mach contours, 3D subsonic boundary layers, and Knudsen contours were presented as well.

Can a better accuracy on performance prediction be achieved by coupling the individual simulation of VLM heater chamber and micronozzle?

Results of the VLM microchannel boiling flow were compared to Yin and Jia's experimental data presented in [116]. The model presented uncertainties that could not be quantified in this study, and the accuracy of the model could not be quantified as well. However, the heat transfer performance results obtained for the VLM microchannel using relaxation parameter values of $\lambda_e = \lambda_c = 1$ s^{-1} are in line with the trend obtained for Yin's microchannel flow in the experiment. Under the said conditions, the VLM microchannel heat transfer coefficient reached it peak value of 106.57 kW/m^2 at moderate thermodynamic quality, x_e of 0.25. This value is much higher compared to that of Yin's however it must be noted that a very high heat flux was imposed to the VLM microchannel bottom wall at a relatively lower mass flux conditions. Furthermore, the heat transfer coefficient in Yin's experiment was calculated based on the fluid saturation temperature, whereas for the VLM microchannel, the fluid bulk temperature was utilized which is much closer to the wall temperature resulting in a higher heat transfer coefficient.

The 3D micronozzle flow modeling results were compared to the experimental results of Cen and Xu [20] where microthruster was tested with water to evaluate the performance of the thruster. In this regard, mass flow rate, thrust, and specific impulse were compared and a difference of around 8.7 %, 5.5 %, and 1.2 % was achieved respectively. The model was validated with an acceptable inaccuracy margin of 10 %, confirming its reliability. Furthermore, the next-generation VLM performance was compared with the third-generation micronozzle performance evaluated in [36] using cold nitrogen gas at throat Reynolds number in the range of $Re_t \sim 500 - 1000$. The performance predicted by the model for the new generation VLM micronozzle with water vapor flow was higher with C_d = 0.913, η_F =0.888 and η_{Isp} = 0.990 obtained at $Re_t \sim 730$.

Individual simulations were assessed as explained, however, since the coupling of the two numerical models could not be performed, the accuracy of the coupled model could not be achieved in this study. Such a coupled model was not feasible, as the microchannel flow boiling CFD model presented uncertainties regarding the evaporation condensation model used in the simulation. The model uses an empirical parameter that defines the phase change rate. This parameter needed to be estimated based on the experimental observation. Such data is not widely available in the literature, so the value used in the model is based on values used for similar modeling found in the literature. Furthermore, the already complex flow phenomenon of microchannel flow boiling had to be coupled with micronozzle flow through tuning of the mass flow rate at the microchannel model inlet boundary. This idea of re-iterating the microchannel simulation with the value of mass flow rate obtained from micronozzle simulation was thus disregarded as first the microchannel model certainty could not be studied, secondly, the re-iteration would not be able to produce the expected results due to model sensitivity to slight changes in boundary parameters, and lastly, the simulation time associated with the microchannel two-phase CFD flow modeling was too long around more than 1 week in general with the supercomputer DelftBlue where all the microchannel simulations were run.

Thus at this point, the VLM microchannel CFD model results on flow pattern visualization and heat transfer performance prediction could not be compared with actual VLM experimental results, so their accuracy is not known. Micronozzle CFD model on its own has been proven to provide an accurate estimation of the thruster performance. However, if the coupled numerical model is more accurate or not could not be performed in this study. As such, the research results here are concluded with the above research questions answered, and the next steps to improve the numerical model or new research ideas are provided in section 5.2.

5.2. Recommendations
Some recommendations for further research are as follows:

- **Real microchannel geometry**: A simplified 2D rectangular microchannel geometry was used in this study to characterize the heat transfer performance of the VLM microchannel. At the beginning of the research, a 3D serpentine microchannel simulation with single phase flow was considered, but since the phase change needed to be incorporated into the model it was disregarded and a simplified 2D geometry was adopted instead. A full 3D microchannel simulation with a two-phase flow would be very computationally extensive, but the flow characteristics like flow mixing due to secondary flow and dean vortices unique to the serpentine curvature used in the VLM microchannel would reveal additional effects on the heat transfer capability of the VLM microchannel.

- **Multiple parallel microchannels**: Similarly, instead of five parallel microchannels used in the VLM, a single microchannel flow was simulated. Multiple parallel microchannels flow boiling research can be found in the heat sink literature. Similar research for VLM microchannels can be adapted to study flow boiling instabilities linked with the multiple microchannels.

- **Sensitivity analysis of relaxation parameters**: As explained above, the evaporation condensation relaxation parameters in the multiphase VOF model of VLM microchannel flow boiling greatly affected the resulting heat transfer performance. As such, a sensitivity analysis of that parameter could be conducted to increase the model's reliability.

- **Different heat transfer model**: Only a single multiphase CFD model was explored in this study. However, other heat transfer models in Fluent as well could model the microchannel two-phase flow before disregarding the CFD model as a whole. For instance, the Eulerian-based wall boiling Rensselaer Polytechnic Institute (RPI) Model could be explored to model the microchannel flow.

- **Real gas model for micronozzle**: In this study, the micronozzle flow was simulated based on ideal gas assumptions valid in the low-pressure and high-temperature regions, which does prove accurate enough. As water vapor is rapidly expanded through the divergent section of the micronozzle, the temperature could drop below the saturation temperature of water and condensation can affect the performance of thrusters. A real gas model valid throughout the micronozzle operation could be implemented in this case predicting more accurate performance of the VLM.

- **DSMC model for rarefaction effects**: Several existing research utilizes the particle-based approach of the Direct Simulation Monte Carlo (DSMC) method to characterize the rarefied flow in micronozzles. In this study, the partial slip condition with velocity and temperature jump applied to the walls of the micronozzle accounted for some rarefaction effects. However, in lower operating pressure ranges than were used in this study, the model's accuracy could not be confirmed. Flow at the divergent section could transition to a rarefied regime. In such conditions DSMC method although very extensive with a large number of simulated particles can be important to accurately predict the performances of micronozzles.

- **Micronozzle convergence angle**: The new generation VLM micronozzle simulated in this study has a higher convergence angle than is conventionally found in the literature. During the simulation, it was found that there is flow reversal at the convergent section near the inlet as flow could not overcome the sharp bending of the geometry right after the entrance. Using a higher pressure at the inlet boundary or increasing the micronozzle throat area did not solve the problem. Thus in the simulation flow was not allowed to exit through the nozzle for the solver stability however, the flow reversal in reality will cause instability in micronozzle operation and will affect its performance. So using a lower convergence angle for the micronozzle where flow gradually turns towards the throat is recommended.

- **Coupling problem**: Coupling the individual CFD models of microchannel and micronozzle could not be achieved in this study. However, an alternative approach would be to model both microchannel and micronozzle into a single two-phase computational domain. To reduce complexities regarding two-phase flow, the model could be 2D and the upstream of the micronozzle could be simplified into multiple straight microchannels spanning the whole width. The multiple microchannels can make the problem complex (associated with pressure fluctuations that could occur at different microchannels), but it can reveal important flow characteristics and the simulation times can be estimated to be approximately the combined simulation times of this study, using the supercomputer.

References

[1] W.M. Abed et al. "Numerical and experimental investigation of heat transfer and fluid flow characteristics in a micro-scale serpentine channel". In: *International Journal of Heat and Mass Transfer* 88 (Sept. 2015), pp. 790–802. ISSN: 0017-9310. DOI: 10.1016/J.IJHEATMASSTRANSFER.2015.04.062.

[2] T. Alam et al. "Favourably regulating two-phase flow regime of flow boiling HFE-7100 in microchannels using silicon nanowires". In: *Scientific Reports* | 11 (123), p. 11131. DOI: 10.1038/s41598-021-89466-z. URL: https://doi.org/10.1038/s41598-021-89466-z.

[3] A.A. Alexeenko et al. "Numerical Modeling of Axisymmetric and Three-Dimensional Flows in Microelectromechanical Systems Nozzles". In: *https://doi.org/10.2514/2.1726* 40 (5 May 2012), pp. 897–904. ISSN: 00011452. DOI: 10.2514/2.1726. URL: https://arc.aiaa.org/doi/10.2514/2.1726.

[4] A.A. Alexeenko et al. "Performance Analysis of Microthrusters Based on Coupled Thermal-Fluid Modeling and Simulation". In: *https://doi.org/10.2514/1.5354* 21 (1 May 2012), pp. 95–101. ISSN: 15333876. DOI: 10.2514/1.5354. URL: https://arc.aiaa.org/doi/10.2514/1.5354.

[5] R. Ali, B. Palm, and M. H. Maqbool. "Flow Boiling Heat Transfer of Refrigerants R134a and R245fa in a Horizontal Micro-Channel". In: *Experimental Heat Transfer* 25 (3 June 2012), pp. 181–196. ISSN: 08916152. DOI: 10.1080/08916152.2011.609962. URL: https://www.tandfonline.com/doi/abs/10.1080/08916152.2011.609962.

[6] J.D. Anderson. *Computational Fluid Dynamics: The Basics with Applications*. McGraw-Hill International Editions: Mechanical Engineering. McGraw-Hill, 1995. ISBN: 9780071132107. URL: https://books.google.nl/books?id=phG_QgAACAAJ.

[7] *ANSYS Fluent Theory Guide, Release 14.0*. 2011.

[8] *Ansys Fluent User's Guide, Release 2021 R2, Part III: Solution Mode, Physical Properties*. 2021.

[9] Z. Anwar, B. Palm, and R. Khodabandeh. "Flow boiling heat transfer and dryout characteristics of R152a in a vertical mini-channel". In: *Experimental Thermal and Fluid Science* 53 (Feb. 2014), pp. 207–217. ISSN: 0894-1777. DOI: 10.1016/J.EXPTHERMFLUSCI.2013.12.009.

[10] E.B. Arkilic, K.S. Breuer, and M.A. Schmidt. "Mass flow and tangential momentum accommodation in silicon micromachined channels". In: *Journal of Fluid Mechanics* 437 (June 2001), pp. 29–43. ISSN: 1469-7645. DOI: 10.1017/S0022112001004128. URL: https://www.cambridge.org/core/journals/journal-of-fluid-mechanics/article/mass-flow-and-tangential-momentum-accommodation-in-silicon-micromachined-channels/39FC18424253468F0324D1DE196AB5E3.

[11] K. H. Bang and W. H. Choo. "Flow Boiling in Minichannels of Copper, Brass, and Aluminum Round Tubes". In: *Proceedings of the Second International Conference on Microchannels and Minichannels (ICMM2004)* (Dec. 2008), pp. 559–564. DOI: 10.1115/ICMM2004-2381. URL: https://dx.doi.org/10.1115/ICMM2004-2381.

[12] Z. Y. Bao, D. F. Fletcher, and B. S. Haynes. "Flow boiling heat transfer of Freon R11 and HCFC123 in narrow passages". In: *International Journal of Heat and Mass Transfer* 43 (18 Sept. 2000), pp. 3347–3358. ISSN: 0017-9310. DOI: 10.1016/S0017-9310(99)00379-8.

[13] R.L. Bayt. "Analysis, Fabrication and Testing of a MEMS-based Micropropulsion System". PhD thesis. Massachusetts Institute of Technology, 1999.

[14] F.M. Bianchi. "Numerical analysis of microchannel flow in vaporizing resistojet thrusters". MA thesis. Delft University of Technology, 2023. URL: http://repository.tudelft.nl.

[15] M. Bidabadi, M. A. Heidari, and A. Rahbari. "A novel analytical model of a MEMS vaporizing liquid micro thruster: Multi-phase flow and heat transfer". In: *2010 The 2nd International Conference on Computer and Automation Engineering, ICCAE 2010* 5 (2010), pp. 321–325. DOI: `10.1109/ICCAE.2010.5451436`.

[16] S. Bigham and S. Moghaddam. "Microscale study of mechanisms of heat transfer during flow boiling in a microchannel". In: *International Journal of Heat and Mass Transfer* 88 (Sept. 2015), pp. 111–121. ISSN: 0017-9310. DOI: `10.1016/J.IJHEATMASSTRANSFER.2015.04.034`.

[17] J.U Brackbill, D.B Kothe, and C. Zemach. "A continuum method for modeling surface tension". In: *Journal of Computational Physics* 100.2 (1992), pp. 335–354. ISSN: 0021-9991. DOI: `https://doi.org/10.1016/0021-9991(92)90240-Y`. URL: `https://www.sciencedirect.com/science/article/pii/002199919290240Y`.

[18] C. Cappelletti, S. Battistini., and B.K. Malphrus. *Cubesat handbook : from mission design to operations*. London : Academic Press, 2021.

[19] G.P. Celata et al. "Flow pattern analysis of flow boiling inside a 0.48 mm microtube". In: *International Journal of Thermal Sciences* 58 (Aug. 2012), pp. 1–8. ISSN: 1290-0729. DOI: `10.1016/J.IJTHERMALSCI.2012.03.014`.

[20] J. W. Cen and J. L. Xu. "Performance evaluation and flow visualization of a MEMS based vaporizing liquid micro-thruster". In: *Acta Astronautica* 67.3-4 (Aug. 2010), pp. 468–482. ISSN: 00945765. DOI: `10.1016/j.actaastro.2010.04.009`.

[21] *CFD Online*. 2024. URL: `https://www.cfd-online.com/Forums/fluent/238871-where-rgp-table-file-created.html` (visited on 12/05/2024).

[22] K. H. Cheah and K. S. Low. "Fabrication and performance evaluation of a high temperature co-fired ceramic vaporizing liquid microthruster". In: *Journal of Micromechanics and Microengineering* 25.1 (Jan. 2015). ISSN: 13616439. DOI: `10.1088/0960-1317/25/1/015013`.

[23] K.H. Cheah. *Space Micropropulsion for Nanosatellites: Progress, Challenges and Future*. Elsevier, Jan. 2022, pp. 1–315. ISBN: 9780128190371. DOI: `10.1016/C2018-0-05037-9`.

[24] C. C. Chen et al. "Simulation and experiment research on vaporizing liquid micro-thruster". In: *Sensors and Actuators, A: Physical* 157.1 (Jan. 2010), pp. 140–149. ISSN: 09244247. DOI: `10.1016/j.sna.2009.10.025`.

[25] John C. Chen. "Correlation for boiling heat transfer to saturated fluids in convective flow". In: *Industrial and Engineering Chemistry Process Design and Development* 5 (3 July 1966), pp. 322–329. ISSN: 01964305. DOI: `10.1021/I260019A023/ASSET/I260019A023.FP.PNG_V03`. URL: `https://pubs.acs.org/doi/abs/10.1021/i260019a023`.

[26] L. Cheng and G. Xia. "Fundamental issues, mechanisms and models of flow boiling heat transfer in microscale channels". In: *International Journal of Heat and Mass Transfer* 108 (May 2017), pp. 97–127. ISSN: 0017-9310. DOI: `10.1016/J.IJHEATMASSTRANSFER.2016.12.003`.

[27] P. Cheng and H. Y. Wu. "Mesoscale and Microscale Phase-Change Heat Transfer". In: *Advances in Heat Transfer* 39 (C Jan. 2006), pp. 461–563. ISSN: 0065-2717. DOI: `10.1016/S0065-2717(06)39005-3`.

[28] E.M. Chiapero, M. Fernandino, and C.A. Dorao. "Experimental results on boiling heat transfer coefficient, frictional pressure drop and flow patterns for R134a at a saturation temperature of 34 °C". In: *International Journal of Refrigeration* 40 (Apr. 2014), pp. 317–327. ISSN: 0140-7007. DOI: `10.1016/J.IJREFRIG.2013.11.026`.

[29] J.G. Collier and J.R. Thome. *Convective Boiling and Condensation*. Oxford University Press, 1994.

[30] J. R. Cooper. "Representation of the ideal-gas thermodynamic properties of water". In: *International Journal of Thermophysics* 3 (1 Mar. 1982), pp. 35–43. ISSN: 0195928X. DOI: `10.1007/BF00503957/METRICS`. URL: `https://link.springer.com/article/10.1007/BF00503957`.

[31] S. Dandavino et al. "Microfabricated electrospray emitter arrays with integrated extractor and accelerator electrodes for the propulsion of small spacecraft". In: *Journal of Micromechanics and Microengineering* 24.7 (June 2014), p. 075011. ISSN: 0960-1317. DOI: `10.1088/0960-1317/24/7/075011`. URL: `https://iopscience.iop.org/article/10.1088/0960-1317/24/7/075011%20https://iopscience.iop.org/article/10.1088/0960-1317/24/7/075011/meta`.

[32] M. G. De Giorgi and D. Fontanarosa. "A novel quasi-one-dimensional model for performance estimation of a Vaporizing Liquid Microthruster". In: *Aerospace Science and Technology* 84 (Jan. 2019), pp. 1020–1034. ISSN: 12709638. DOI: `10.1016/j.ast.2018.11.039`.

[33] X. Fang et al. "Saturated flow boiling heat transfer: review and assessment of prediction methods". In: *Heat and Mass Transfer/Waerme- und Stoffuebertragung* 55 (1 Jan. 2019), pp. 197–222. ISSN: 14321181. DOI: `10.1007/S00231-018-2432-1/TABLES/13`. URL: `https://link.springer.com/article/10.1007/s00231-018-2432-1`.

[34] A. Ferrari, M. Magnini, and J. R. Thome. "Numerical analysis of slug flow boiling in square microchannels". In: *International Journal of Heat and Mass Transfer* 123 (2018), pp. 928–944. ISSN: 0017-9310. DOI: `https://doi.org/10.1016/j.ijheatmasstransfer.2018.03.012`. URL: `https://www.sciencedirect.com/science/article/pii/S0017931018303016`.

[35] M. Gad-El-Hak. "The Fluid Mechanics of Microdevices—The Freeman Scholar Lecture". In: *Journal of Fluids Engineering* 121 (1 Mar. 1999), pp. 5–33. ISSN: 0098-2202. DOI: `10.1115/1.2822013`. URL: `https://dx.doi.org/10.1115/1.2822013`.

[36] C.S. Ganani. "Micronozzle Performance A Numerical and Experimental Study". MA thesis. Delft University of Technology, 2019. URL: `http://repository.tudelft.nl`.

[37] R. Ghodssi and P. Lin. *MEMS Materials and Processes Handbook*. Vol. 1. Springer Science & Business Media, 2011.

[38] M.G. De Giorgi and D. Fontanarosa. "Numerical data concerning the performance estimation of a Vaporizing Liquid Microthruster". In: *Data in Brief* 22 (Feb. 2019), pp. 307–311. ISSN: 2352-3409. DOI: `10.1016/J.DIB.2018.12.013`.

[39] A. Greco and G.P. Vanoli. "Flow-boiling of R22, R134a, R507, R404A and R410A inside a smooth horizontal tube". In: *International Journal of Refrigeration* 28 (6 Sept. 2005), pp. 872–880. ISSN: 0140-7007. DOI: `10.1016/J.IJREFRIG.2005.01.008`.

[40] C.A.J. Hanselaar. "Evaporative Two-Phase Micro-Flow Modelling". MA thesis. Delft University of Technology, 2016. URL: `http://repository.tudelft.nl`.

[41] T. Harirchian and S.V. Garimella. "A comprehensive flow regime map for microchannel flow boiling with quantitative transition criteria". In: *International Journal of Heat and Mass Transfer* 53 (13-14 June 2010), pp. 2694–2702. ISSN: 0017-9310. DOI: `10.1016/J.IJHEATMASSTRANSFER.2010.02.039`.

[42] T. Harirchian and S.V. Garimella. "Effects of channel dimension, heat flux, and mass flux on flow boiling regimes in microchannels". In: *International Journal of Multiphase Flow* 35 (4 Apr. 2009), pp. 349–362. ISSN: 0301-9322. DOI: `10.1016/J.IJMULTIPHASEFLOW.2009.01.003`.

[43] J.Kim and J.S. Lee. "Numerical study on the effects of inertia and wettability on subcooled flow boiling in microchannels". In: *Applied Thermal Engineering* 152 (Apr. 2019), pp. 175–183. ISSN: 1359-4311. DOI: `10.1016/J.APPLTHERMALENG.2019.02.064`.

[44] A. M. Jacobi and J. R. Thome. "Heat Transfer Model for Evaporation of Elongated Bubble Flows in Microchannels". In: *Journal of Heat Transfer* 124 (6 Dec. 2002), pp. 1131–1136. ISSN: 0022-1481. DOI: `10.1115/1.1517274`. URL: `https://dx.doi.org/10.1115/1.1517274`.

[45] S. G. Kandlikar. "Heat Transfer Mechanisms During Flow Boiling in Microchannels". In: *Journal of Heat Transfer* 126 (1 Feb. 2004), pp. 8–16. ISSN: 0022-1481. DOI: `10.1115/1.1643090`. URL: `https://dx.doi.org/10.1115/1.1643090`.

[46] S. G. Kandlikar. "Scale effects on flow boiling heat transfer in microchannels: A fundamental perspective". In: *International Journal of Thermal Sciences* 49 (7 July 2010), pp. 1073–1085. ISSN: 1290-0729. DOI: `10.1016/J.IJTHERMALSCI.2009.12.016`.

[47] S. G. Kandlikar. "Similarities and Differences Between Flow Boiling in Microchannels and Pool Boiling". In: *Heat Transfer Engineering* 31 (3 Mar. 2010), pp. 159–167. ISSN: 01457632. DOI: 10.1080/01457630903304335. URL: https://www.tandfonline.com/doi/abs/10.1080/01457630903304335.

[48] S.G. Kandlikar and W.J. Grande. "Evolution of Microchannel Flow Passages-Thermohydraulic Performance and Fabrication Technology". In: *Heat Transfer Engineering* 24 (1 2003), pp. 3–17. ISSN: 1521-0537. DOI: 10.1080/01457630304040. URL: https://www.tandfonline.com/action/journalInformation?journalCode=uhte20.

[49] T. G. Karayiannis and M. M. Mahmoud. "Flow boiling in microchannels: Fundamentals and applications". In: *Applied Thermal Engineering* 115 (Mar. 2017), pp. 1372–1397. ISSN: 1359-4311. DOI: 10.1016/J.APPLTHERMALENG.2016.08.063.

[50] K. Karthikeyan et al. "Low temperature co-fired ceramic vaporizing liquid microthruster for microspacecraft applications". In: *Applied Energy* 97 (2012), pp. 577–583. ISSN: 03062619. DOI: 10.1016/j.apenergy.2011.11.078.

[51] P.A. Kew and K. Cornwell. "Correlations for the prediction of boiling heat transfer in small-diameter channels". In: *Applied Thermal Engineering* 17 (8-10 Aug. 1997), pp. 705–715. ISSN: 1359-4311. DOI: 10.1016/S1359-4311(96)00071-3.

[52] N. H. Kim, Y. S. Sim, and C. K. Min. "Convective Boiling of R-22 in a Flat Extruded Aluminum Multi-Port Tube". In: *Proceedings of the Second International Conference on Microchannels and Minichannels (ICMM2004)* (Dec. 2008), pp. 507–513. DOI: 10.1115/ICMM2004-2375. URL: https://dx.doi.org/10.1115/ICMM2004-2375.

[53] S.M. Kim and I. Mudawar. "Universal approach to predicting saturated flow boiling heat transfer in mini/micro-channels – Part I. Dryout incipience quality". In: *International Journal of Heat and Mass Transfer* 64 (Sept. 2013), pp. 1226–1238. ISSN: 0017-9310. DOI: 10.1016/J.IJHEATMASSTRANSFER.2013.04.016.

[54] P. Kundu, T. K. Bhattacharyya, and S. Das. "Design, fabrication and performance evaluation of a vaporizing liquid microthruster". In: *Journal of Micromechanics and Microengineering* 22.2 (Feb. 2012). ISSN: 09601317. DOI: 10.1088/0960-1317/22/2/025016.

[55] A. Kurmanbay. "Design, Fabrication and Characterization of MEMS based micro heater for Vaporizing Liquid Microthruster". MA thesis. Delft University of Technology, 2019. URL: http://repository.tudelft.nl.

[56] U. Kvell et al. "Nanosatellite orbit control using MEMS cold gas thrusters". In: *Proceedings of the Estonian Academy of Sciences* 63 (2014), pp. 279–285. DOI: 10.3176/proc.2014.2S.09. URL: www.eap.ee/proceedings.

[57] P. W. Kwan, X. Huang, and X. Zhang. "Design and testing of a microelectromechanical-system-based high heat flux vaporizing liquid microthruster". In: *Acta Astronautica* 170 (May 2020), pp. 719–734. ISSN: 0094-5765. DOI: 10.1016/J.ACTAASTRO.2020.01.017.

[58] G. M. Lazarek and S. H. Black. "Evaporative heat transfer, pressure drop and critical heat flux in a small vertical tube with R-113". In: *International Journal of Heat and Mass Transfer* 25 (7 July 1982), pp. 945–960. ISSN: 0017-9310. DOI: 10.1016/0017-9310(82)90070-9.

[59] J. Lee and I. Mudawar. "Critical heat flux for subcooled flow boiling in micro-channel heat sinks". In: *International Journal of Heat and Mass Transfer* 52 (13-14 June 2009), pp. 3341–3352. ISSN: 0017-9310. DOI: 10.1016/J.IJHEATMASSTRANSFER.2008.12.019.

[60] J. Lee and I. Mudawar. "Fluid flow and heat transfer characteristics of low temperature two-phase micro-channel heat sinks – Part 2. Subcooled boiling pressure drop and heat transfer". In: *International Journal of Heat and Mass Transfer* 51 (17-18 Aug. 2008), pp. 4327–4341. ISSN: 0017-9310. DOI: 10.1016/J.IJHEATMASSTRANSFER.2008.02.013.

[61] J. Lee and I. Mudawar. "Two-phase flow in high-heat-flux micro-channel heat sink for refrigeration cooling applications: Part II—heat transfer characteristics". In: *International Journal of Heat and Mass Transfer* 48 (5 Feb. 2005), pp. 941–955. ISSN: 0017-9310. DOI: 10.1016/J.IJHEATMASSTRANSFER.2004.09.019.

[62] W.H. Lee. "A pressure iteration scheme for two-phase flow modeling". In: *Multiphase transport fundamentals, reactor safety, applications* 1 (1980), pp. 407–431.

[63] E.W. Lemmon et al. *Thermophysical Properties of Fluid Systems*. 2024. URL: `https://webbook.nist.gov/` (visited on 11/02/2024).

[64] X. Li et al. "Influences of geometry configurations on the performance of micro-nozzles". In: *Acta Astronautica* 215 (Feb. 2024), pp. 618–630. ISSN: 0094-5765. DOI: `10.1016/J.ACTAASTRO.2023.12.045`.

[65] R.J.d.S. Lima, J.M. Quibén, and J.R. Thome. "Flow boiling in horizontal smooth tubes: New heat transfer results for R-134a at three saturation temperatures". In: *Applied Thermal Engineering* 29 (7 May 2009), pp. 1289–1298. ISSN: 1359-4311. DOI: `10.1016/J.APPLTHERMALENG.2008.06.021`.

[66] B. Liu et al. "Recent advances in MEMS-based microthrusters". In: *Micromachines* 10.12 (Dec. 2019). ISSN: 2072666X. DOI: `10.3390/MI10120818`.

[67] C. Liu. *Foundations of MEMS*. Pearson Education Limited, 2012.

[68] H. Liu et al. "An assessment and analysis of phase change models for the simulation of vapor bubble condensation". In: *International Journal of Heat and Mass Transfer* 157 (Aug. 2020), p. 119924. ISSN: 0017-9310. DOI: `10.1016/J.IJHEATMASSTRANSFER.2020.119924`.

[69] M. Liu et al. "Study on micronozzle flow and propulsion performance using DSMC and continuum methods". In: *Acta Mechanica Sinica/Lixue Xuebao* 22 (5 Oct. 2006), pp. 409–416. ISSN: 05677718. DOI: `10.1007/S10409-006-0020-Y/METRICS`. URL: `https://link.springer.com/article/10.1007/s10409-006-0020-y`.

[70] W.F. Louisos and D.L. Hitt. "Viscous Effects on Performance of Three-Dimensional Supersonic Micronozzles". In: *https://doi.org/10.2514/1.53026* 49 (1 Aug. 2012), pp. 51–58. ISSN: 15336794. DOI: `10.2514/1.53026`. URL: `https://arc.aiaa.org/doi/10.2514/1.53026`.

[71] R.A. Makhan. "Performance of the MEMS Vaporizing Liquid Microthruster using cold nitrogen gas as propellant An experimental study". MA thesis. Delft University of Technology, 2018. URL: `http://repository.tudelft.nl`.

[72] T.V. Mathew. "Design of a MEMS micro-resistojet". MA thesis. Delft University of Technology, 2011. URL: `https://repository.tudelft.nl`.

[73] D. K. Maurya, S. Das, and S. K. Lahiri. "An analytical model of a silicon MEMS vaporizing liquid microthruster and some experimental studies". In: *Sensors and Actuators, A: Physical* 122.1 SPEC. ISS. (July 2005), pp. 159–166. ISSN: 09244247. DOI: `10.1016/j.sna.2005.04.020`.

[74] D. K. Maurya, S. Das, and S. K. Lahiri. "Silicon MEMS vaporizing liquid microthruster with internal microheater". In: *Journal of Micromechanics and Microengineering* 15.5 (May 2005), pp. 966–970. ISSN: 09601317. DOI: `10.1088/0960-1317/15/5/010`.

[75] J.C. Maxwell. "VII. On stresses in rarified gases arising from inequalities of temperature". In: *Philosophical Transactions of the Royal Society of London* 170 (1879), pp. 231–256. DOI: `10.1098/rstl.1879.0067`.

[76] B.J. McBride, S. Gordon, and M. A. Reno. *Coefficients for Calculating Thermodynamic and Transport Properties of Individual Species*. 2024. URL: `https://ntrs.nasa.gov/api/citations/19940013151/downloads/19940013151.pdf` (visited on 11/04/2024).

[77] M. Mihailovic et al. "MEMS silicon-based resistojet micro-thruster for attitude control of nano-satellites". In: *2011 16th International Solid-State Sensors, Actuators and Microsystems Conference, TRANSDUCERS'11*. 2011, pp. 262–265. ISBN: 9781457701573. DOI: `10.1109/TRANSDUCERS.2011.5969432`.

[78] S. Mortada et al. "Boiling heat transfer and pressure drop of R-134a and R-1234yf in minichannels for low mass fluxes". In: *International Journal of Refrigeration* 35 (4 June 2012), pp. 962–973. ISSN: 0140-7007. DOI: `10.1016/J.IJREFRIG.2012.03.004`.

[79] J. Mueller. "Thruster options for microspacecraft: A review and evaluation of existing hardware and emerging technologies". In: *33rd Joint Propulsion Conference and Exhibit* (1997). DOI: `10.2514/6.1997-3058`.

[80] V. Pallichadath et al. "In-orbit micro-propulsion demonstrator for PICO-satellite applications". In: *Acta Astronautica* 165 (Dec. 2019), pp. 414–423. ISSN: 00945765. DOI: `10.1016/J.ACTAASTRO.2019.09.004`.

[81] V. Pallichadath et al. "In-orbit micro-propulsion demonstrator for PICO-satellite applications". In: *Acta Astronautica* 165 (Dec. 2019), pp. 414–423. ISSN: 0094-5765. DOI: `10.1016/J.ACTAASTRO.2019.09.004`.

[82] P.K. Panigrahi and M. Asfer. "Boundary Slip of Liquids". In: *Encyclopedia of Microfluidics and Nanofluidics*. Boston, MA: Springer US, 2008, pp. 140–147. ISBN: 978-0-387-48998-8. DOI: `10.1007/978-0-387-48998-8_124`. URL: `https://doi.org/10.1007/978-0-387-48998-8_124`.

[83] A. Pappadimitriou. "Performance Evaluation of a Vaporizing Liquid Microthruster using nitrogen and water as propellants". MA thesis. Delft University of Technology, 2018. URL: `http://repository.tudelft.nl`.

[84] J. M. Pearl, W. F. Louisos, and D. L. Hitt. "Three-dimensional numerical study of linear plug micronozzles". In: *53rd AIAA Aerospace Sciences Meeting* (2015). DOI: `10.2514/6.2015-1621`. URL: `https://arc.aiaa.org/doi/10.2514/6.2015-1621`.

[85] J.M. Pearl, W.F. Louisos, and D.L. Hitt. "Thrust calculation for low-reynolds-number micronozzles". In: *Journal of Spacecraft and Rockets* 54 (1 Dec. 2017), pp. 287–298. ISSN: 15336794. DOI: `10.2514/1.A33535/ASSET/IMAGES/LARGE/FIGURE11.JPEG`. URL: `https://arc.aiaa.org/doi/10.2514/1.A33535`.

[86] R.M.A. Poyck. "Design, manufacturing and characterisation of a water fed CubeSat micro-resistojet Dondersteen". MA thesis. Delft University of Technology, 2014. URL: `http://repository.tudelft.nl`.

[87] W. Qu and I. Mudawar. "Flow boiling heat transfer in two-phase micro-channel heat sinks—I. Experimental investigation and assessment of correlation methods". In: *International Journal of Heat and Mass Transfer* 46 (15 July 2003), pp. 2755–2771. ISSN: 0017-9310. DOI: `10.1016/S0017-9310(03)00041-3`.

[88] G. Ribatski, L. Wojtan, and J.R. Thome. "An analysis of experimental data and prediction methods for two-phase frictional pressure drop and flow boiling heat transfer in micro-scale channels". In: *Experimental Thermal and Fluid Science* 31 (1 Oct. 2006), pp. 1–19. ISSN: 0894-1777. DOI: `10.1016/J.EXPTHERMFLUSCI.2006.01.006`.

[89] D.E. Rothe. "Electron-beam studies of viscous flow in supersonic nozzles". In: *https://doi.org/10.2514/3.6279* 9 (5 May 1971), pp. 804–811. ISSN: 00011452. DOI: `10.2514/3.6279`. URL: `https://arc.aiaa.org/doi/10.2514/3.6279`.

[90] J. Scott. *Shock Diamonds and Mach Disks*. 2024. URL: `https://aerospaceweb.org/question/propulsion/q0224.shtml` (visited on 11/08/2024).

[91] A. Sharma and M. K. Khan. "Heat transfer and flow characteristics of varying curvature wavy microchannels". In: *International Journal of Thermal Sciences* 185 (Mar. 2023), p. 108096. ISSN: 1290-0729. DOI: `10.1016/J.IJTHERMALSCI.2022.108096`.

[92] M.A.C. Silva. "MEMS Micropropulsion Design, Modeling and Control of Vaporizing Liquid Microthrusters". PhD thesis. Delft University of Technology, 2018. URL: `https://doi.org/10.4233/uuid:57f725e1-b3f3-455c-83ce-9156b2123c88`.

[93] M.A.C. Silva et al. "A review of MEMS micropropulsion technologies for CubeSats and PocketQubes". In: *Acta Astronautica* 143 (Feb. 2018), pp. 234–243. ISSN: 00945765. DOI: `10.1016/J.ACTAASTRO.2017.11.049`.

[94] M.A.C. Silva et al. "Vaporizing Liquid Microthrusters with integrated heaters and temperature measurement". In: *Sensors and Actuators A: Physical* 265 (Oct. 2017), pp. 261–274. ISSN: 0924-4247. DOI: `10.1016/J.SNA.2017.07.032`.

[95] S. I. Singh. "Design, Fabrication and Characterization of MEMS Micro-resistojet Thrusters". MA thesis. Delft University of Technology, 2023. URL: `https://resolver.tudelft.nl/uuid:103b1edc-c3d4-4a44-9309-f9748fe9eace`.

[96] W. Sutherland. "LII. The viscosity of gases and molecular force". In: *The London, Edinburgh, and Dublin Philosophical Magazine and Journal of Science* 36 (223 Dec. 1893), pp. 507–531. ISSN: 1941-5982. DOI: `10.1080/14786449308620508`.

[97] J. R. Thome and A.Cioncolini. "Flow Boiling in Microchannels". In: *Advances in Heat Transfer* 49 (Jan. 2017), pp. 157–224. ISSN: 0065-2717. DOI: `10.1016/BS.AIHT.2017.06.001`.

[98] J.R. Thome. "Boiling in microchannels: a review of experiment and theory". In: *International Journal of Heat and Fluid Flow* 25 (2 Apr. 2004), pp. 128–139. ISSN: 0142-727X. DOI: `10.1016/J.IJHEATFLUIDFLOW.2003.11.005`.

[99] J.R. Thome. *Wolverine engineering data book III.* (web book updated yearly), 2006. URL: `https://infoscience.epfl.ch/handle/20.500.14299/214953`.

[100] C.B. Tibiriçá and G. Ribatski. "Flow patterns and bubble departure fundamental characteristics during flow boiling in microscale channels". In: *Experimental Thermal and Fluid Science* 59 (Nov. 2014), pp. 152–165. ISSN: 0894-1777. DOI: `10.1016/J.EXPTHERMFLUSCI.2014.02.017`.

[101] C.B. Tibiriçá et al. "A complete set of simple and optimized correlations for microchannel flow boiling and two-phase flow applications". In: *Applied Thermal Engineering* 126 (Nov. 2017), pp. 774–795. ISSN: 1359-4311. DOI: `10.1016/J.APPLTHERMALENG.2017.07.161`.

[102] L. S. Tong and Y. S. Tang. "Boiling Heat Transfer And Two-Phase Flow". In: *Boiling Heat Transfer and Two-Phase Flow* (May 2018). DOI: `10.1201/9781315138510`. URL: `https://www.taylorfrancis.com/books/mono/10.1201/9781315138510/boiling-heat-transfer-two-phase-flow-tong`.

[103] F. La Torre. "Gas flow in miniaturized nozzles for micro-thrusters". PhD thesis. Delft University of Technology, 2011. URL: `https://resolver.tudelft.nl/uuid:176902dc-7234-414c-af5b-87ef11ec6dc1`.

[104] T.X. Van Wees. "Characterization and Testing of a MEMS-Vaporizing Liquid Microthruster for Small Satellite Propulsion". MA thesis. Delft University of Technology, 2017. URL: `http://repository.tudelft.nl`.

[105] H.K. Versteeg and W. Malalasekera. *An Introduction to Computational Fluid Dynamics: The Finite Volume Method.* Pearson Education Limited, 2007. ISBN: 9780131274983. URL: `https://books.google.nl/books?id=RvBZ-UMpGzIC`.

[106] J.N. Weinmiller. "Multiphase flow in micro-thrusters Using lattice Boltzmann modeling". MA thesis. Delft University of Technology, 2021. URL: `http://repository.tudelft.nl`.

[107] L.T. Williams and M.F. Osborn. "Performance impacts of geometry and operating conditions on a low Reynolds number micro-nozzle flow". In: *IEPC* 120 (2017), pp. 1–12.

[108] H.W. Woolley. *Water and Steam: Their properties and current industrial applications, J. Straub and K. Scheffler (editors), Pergamon Press, 1980*.

[109] M.H. Wu and P.S. Lin. "Design, fabrication and characterization of a low-temperature co-fired ceramic gaseous bi-propellant microthruster". In: *Journal of Micromechanics and Microengineering* 20.8 (Aug. 2010). ISSN: 09601317. DOI: `10.1088/0960-1317/20/8/085026`.

[110] C. Xie. "Characteristics of micronozzle gas flows". In: *Physics of Fluids* 19 (3 Mar. 2007). ISSN: 10706631. DOI: `10.1063/1.2709707/255883`. URL: `/aip/pof/article/19/3/037102/255883/Characteristics-of-micronozzle-gas-flows`.

[111] Y. Xu et al. "An experimental study of flow boiling heat transfer of R134a and evaluation of existing correlations". In: *International Journal of Heat and Mass Transfer* 92 (Jan. 2016), pp. 1143–1157. ISSN: 0017-9310. DOI: `10.1016/J.IJHEATMASSTRANSFER.2015.09.044`.

[112] H. Yamaguchi et al. "Experimental measurements of thermal and tangential momentum accommodation coefficients on solid surfaces: Water vapor in comparison with noble gases". In: *International Journal of Heat and Mass Transfer* 183 (Feb. 2022), p. 122195. ISSN: 0017-9310. DOI: `10.1016/J.IJHEATMASSTRANSFER.2021.122195`.

[113] G. Yang et al. "Review on bubble dynamic of subcooled flow boiling-part b: Behavior and models". In: *International Journal of Thermal Sciences* 184 (Feb. 2023), p. 108026. ISSN: 1290-0729. DOI: `10.1016/J.IJTHERMALSCI.2022.108026`.

[114] X. Y. Ye et al. "Study of a vaporizing water micro-thruster". In: *Sensors and Actuators A: Physical* 89.1-2 (Mar. 2001), pp. 159–165. ISSN: 0924-4247. DOI: `10.1016/S0924-4247(00)00540-9`.

[115] I. Yeo and S. Lee. "2D computational investigation into transport phenomena of subcooled and saturated flow boiling in large length to diameter ratio micro-channel heat sinks". In: *International Journal of Heat and Mass Transfer* 183 (Feb. 2022), p. 122128. ISSN: 0017-9310. DOI: `10.1016/J.IJHEATMASSTRANSFER.2021.122128`.

[116] L. Yin and L. Jia. "Confined bubble growth and heat transfer characteristics during flow boiling in microchannel". In: *International Journal of Heat and Mass Transfer* 98 (July 2016), pp. 114–123. ISSN: 0017-9310. DOI: `10.1016/J.IJHEATMASSTRANSFER.2016.02.063`.

[117] L. Yin et al. "Subcooled flow boiling of water in a large aspect ratio microchannel". In: *International Journal of Heat and Mass Transfer* 112 (Sept. 2017), pp. 1081–1089. ISSN: 0017-9310. DOI: `10.1016/J.IJHEATMASSTRANSFER.2017.05.028`.

[118] B.T.C. Zandbergen. *Course AE4S01 Thermal Rocket Propulsion (version 2.08)*. Tech. rep. 2020.

[119] K. L. Zhang et al. "A MEMS-based solid propellant microthruster with Au/Ti igniter". In: *Sensors and Actuators A: Physical* 122.1 (July 2005), pp. 113–123. ISSN: 0924-4247. DOI: `10.1016/J.SNA.2005.04.021`.

[120] A. Zilié, D. L. Hitt, and A. A. Alexeenko. "Numerical simulations of supersonic flow in a linear aerospike micronozzle". In: *Collection of Technical Papers - 37th AIAA Fluid Dynamics Conference* 1 (2007), pp. 482–495. DOI: `10.2514/6.2007-3984`.

A
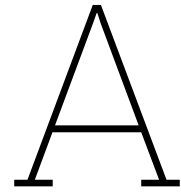
Real Gas Property (RGP) Table

The following script is used to generate the RGP table for water and water vapor used in the fluent multiphase simulation in this research. [21]

```python
import pyExt.RefProp as arp
fluidsPath = arp.getFluidsPath()
mat = arp.RefPropLib()

fluidList = ['fluids/water.fld'] # Change the REFPROP fluid here
mat.setup(fluidsPath, fluidList)

interpError = 1e-3 # Change accuracy/file size here, units for T,P are [K] and [Pa]
Tmin = 300
Tmax = 700
Pmin = 100.0
Pmax = 2000000.0
fluid_name = 'water' #This is the Fluid Name, which will be followed by L or V for the Phase
# Component names for Liq, Vap and Mix are NameL, NameV, and NameL

# Generate both the liquid and vapor components in the RGP file in one go

fluid = arp.RGPSettings(fluid_name, Tmin, Tmax, Pmin, Pmax, interpError, arp.ADAPT_AUTO_TP)
print(dir(fluid))

arp.generateRGPfile(r"C:\Users\sr_sh\Desktop\Thesis\waterprop.rgp", fluid) # Provide Output
    path and filename here

#"C:\Program Files\ANSYS Inc\v241\SystemCoupling\bin\systemcoupling" -R "C:\Users\sr_sh\
    Desktop\Thesis\Rgp_gen.py"
```